



The Structure and Dynamics of the Subparsec Jet in M87 Based on 50 VLBA Observations over 17 Years at 43 GHz

R. Craig Walker^{1,7} , Philip E. Hardee², Frederick B. Davies³ , Chun Ly^{4,5} , and William Junor⁶

¹National Radio Astronomy Observatory, Socorro, NM 87801, USA; cwalker@nrao.edu

²Department of Physics & Astronomy, The University of Alabama, Tuscaloosa, AL 35487, USA

³Department of Physics, University of California, Santa Barbara, CA 93106-9530, USA

⁴Steward Observatory, 933 N. Cherry Ave., Tucson, AZ 85721, USA

⁵MMT Observatory, 933 N. Cherry Ave., Tucson, AZ 85721, USA

⁶ISR-2, MS-B244, Los Alamos National Laboratory, P.O. Box 1663, Los Alamos, NM 87545, USA

Received 2017 November 15; revised 2018 January 30; accepted 2018 February 13; published 2018 March 15

Abstract

The central radio source in M87 provides the best opportunity to study jet formation because it has a large angular size for the gravitational radius of the black hole and has a bright jet that is well resolved by very long baseline interferometry observations. We present intensive monitoring observations from 2007 and 2008, plus roughly annual observations that span 17 years, all made with the the Very Long Baseline Array at 43 GHz with a resolution of about 30 by $60R_S$. Our high dynamic range images clearly show the wide opening angle structure and the counterjet. The jet and counterjet are nearly symmetric in the inner 1.5 mas (0.12 pc in projection), with both being edge brightened. Both show deviations from parabolic shape in the form of an initial rapid expansion and subsequent contraction followed by further rapid expansion and, beyond the visible counterjet, subsequent collimation. Proper motions and counterjet/jet intensity ratios both indicate acceleration from apparent speeds of $\lesssim 0.5c$ to $\gtrsim 2c$ in the inner ~ 2 mas and suggest a helical flow. The jet displays a sideways shift with an approximately 8–10 yr quasi-periodicity. The shift propagates outward nonballistically and significantly more slowly than the flow speed revealed by the fastest-moving components. Polarization data show a systematic structure with magnetic field vectors that suggest a toroidal field close to the core.

Key words: galaxies: active – galaxies: individual (M87) – galaxies: jets – hydrodynamics – radio continuum: galaxies – relativistic processes

Supporting material: animations

1. Introduction

M87 (Virgo A, NGC 4486, 3C 274) is a giant elliptical galaxy near the center of the Virgo Cluster that contains a very massive black hole and a prominent jet. The scale, in gravitational units per unit angle, is the best for any jet with observed structure, making M87 a prime target for studies of the jet launch region. At a distance to M87 of 16.7 Mpc (Mei et al. 2007), 1 mas ≈ 0.081 pc and 1 mas yr⁻¹ $\approx 0.264c$. At this assumed distance, the black hole in the center of M87 has a mass, determined from stellar dynamics, of $(6.1 \pm 0.4) \times 10^9 M_\odot$ (Gebhardt 2011, adjusted for a different assumed distance). This gives a scale of 1 mas $\approx 140R_S$, where the Schwarzschild radius $R_S \equiv 2GM/c^2 \approx 1.8 \times 10^{15}$ cm.⁸ With this scale, Very Long Baseline Array (VLBA; Napier et al. 1993) observations at 43 GHz (7 mm), with a resolution of 0.2–0.4 mas, probe structures with sizes on the order of $100R_S$.

The well-known, kiloparsec-scale jet in this galaxy is a prominent source of radio, optical, near-ultraviolet (NUV), and X-ray emission. There are remarkable similarities between the radio, optical, and NUV emission on projected scales of

0.1–1 kpc. The bright knots, the filamentary emission between the knots, and the bends and twists in the jet can easily be identified in the optical and NUV, as well as the radio (Perlman et al. 2001). While X-ray images from *Chandra* (Marshall et al. 2002; Wilson & Yang 2002) are not of comparable resolution to the radio or optical, the same bright knots and overall jet structure can easily be seen in the X-rays.

The M87 jet has long been known to have a wide opening angle base on scales well below 1 mas (Junor et al. 1999). On average the jet expands parabolically out to about the first bright knot (known as HST-1) at $\sim 0''.9$ (projected distance ~ 70 pc) from the core (Asada & Nakamura 2012; Hada et al. 2013), but with evidence for faster expansion at the smallest scales (see Hada et al. 2013, 2016). Older very long baseline interferometry (VLBI) observations at 1.6 GHz indicate an FWHM apparent opening angle of $\Theta^{\text{app}} \approx 6^\circ.9$ out to ~ 50 mas (projected distance ~ 4 pc) from the radio core (Reid et al. 1989). Beyond HST-1 the jet expands conically (Asada & Nakamura 2012), and Very Large Array (VLA) observations at 15 GHz indicate an FWHM apparent opening angle of $\Theta^{\text{app}} \approx 6^\circ.5$ from HST-1 to knot A located at $\sim 12''$ (projected distance ~ 930 pc) from the radio core (Owen et al. 1989). The radio core in M87 is thought to be nearly coincident with the position of the black hole, unlike the situation in many blazars (e.g., Marscher et al. 2008). Multifrequency VLBA astrometric observations indicate an

⁷ The National Radio Astronomy Observatory (NRAO) is a facility of the National Science Foundation (NSF), operated under cooperative agreement by Associated Universities, Inc. (AUI).

⁸ The M87 black hole mass is still controversial, with results from gas dynamics giving masses of about half that given above (Walsh et al. 2013). If the smaller mass proves to be correct, all distances given in this paper in R_S will need to be revised upward accordingly.

offset of only 41 μas at 43 GHz (Hada et al. 2011), equivalent to about $6R_s$.

Proper motions of jet components in the radio and optical range from subluminal to superluminal. A component located at ~ 18 mas (projected distance ~ 1.4 pc) shows an angular motion of 1.1 ± 0.3 mas yr $^{-1}$ that corresponds to a subluminal motion of $\beta^{\text{app}} \equiv v^{\text{app}}/c \approx 0.3$ (Reid et al. 1989). Kovalev et al. (2007) find motions of less than a few percent of the speed of light at 15 GHz for several components within 25 mas of the core with the VLBA. That result is based partly on the MOJAVE program (Lister & Homan 2005), a recent reanalysis of which gives hints of acceleration and mild superluminal motion (Britzen et al. 2017). At higher frequencies, both subluminal and mildly superluminal (up to $\beta^{\text{app}} \approx 2.5$) speeds, with evidence for acceleration, have been seen based on the 43 GHz VLBA data to be presented in this paper (Mertens et al. 2016, hereafter MLWH) and based on KaVA (KVN and VERA Array [Korean VLBI Network and VLBI Exploration of Radio Astronomy]) data at 22 GHz (Hada et al. 2017). Slow motions were seen by Hada et al. (2016) with four epochs, two at 86 GHz and two at 43 GHz. With one exception, those components were at core distances of about 1 mas or less. The fastest observed proper motion, found in the optical band at HST-1, is superluminal with $\beta^{\text{app}} = 6.1 \pm 0.6$ (Biretta et al. 1999). The fastest observed radio proper motions, also at HST-1, are superluminal with $\beta^{\text{app}} = 4.3 \pm 0.7$ (Cheung et al. 2007) and 4.17 ± 0.07 and 4.08 ± 0.08 (both Giroletti et al. 2012). Giroletti et al. (2012) also find less reliable evidence for a component moving at $\beta^{\text{app}} = 6.4 \pm 0.8$, similar to the optical result. Asada et al. (2014) find evidence from their 1.6 GHz global VLBI data plus other data from the literature for acceleration from subluminal to superluminal speeds between about 160 mas and HST-1. In general, at and beyond HST-1 the radio proper motions are less than optical proper motions in the same region, and proper motions suggest jet deceleration (see Hardee & Eilek 2011).

An important parameter for interpretation of the data is the jet angle to the line of sight. There is no one, simple way to determine that angle, so the reasoning leading to the choice of the angle used in this paper is explained here at some length. The fastest observed proper motions and modeling can be used to constrain the viewing angle. The highest observed optical superluminal speed requires a jet viewing angle of $\theta < 18^\circ_{-1.6}^{+2.0}$. Recent model-dependent values for the viewing angle are $\theta = 14^\circ$, used by Nakamura & Meier (2014) to provide a self-consistent shock model for optical relativistic motions and particle acceleration at HST-1, and a value of $\theta = 15^\circ$, found by Wang & Zhou (2009) using synchrotron spectrum model fitting to the kiloparsec jet. MLWH found that a viewing angle of $\theta = 19^\circ \pm 4^\circ$ (see Table 6 in MLWH) provided a fit to the observed acceleration and collimation of the jet assuming a Poynting-flux-dominated approximation for the jet dynamics.

Less model-dependent values for the viewing angle can be found in MLWH. A value of $\theta = 17^\circ_2 \pm 3^\circ_3$ (see Equation (4) in MLWH) is obtained by MLWH between 0.5 and 1 mas from the core using apparent component speeds in the jet, $\beta_j^{\text{app}} = 0.21 \pm 0.04$, and the counterjet, $\beta_{\text{cj}}^{\text{app}} = 0.14 \pm 0.02$, along with an intensity ratio, $I_j/I_{\text{cj}} = 9.5 \pm 1.5$. An additional analysis in MLWH, based on the assumption that the significantly different speeds in northern and southern limbs of the jet are the result of jet rotation, leads to a viewing angle

value of $\theta = 19^\circ_2 \pm 3^\circ_7$ (see Equation (9) in MLWH). Thus, MLWH concluded that a viewing angle of $\theta \approx 18^\circ$ represented a reasonable average based on these two techniques and Poynting-flux-dominated jet dynamics. We note here that the jet rotation and Poynting flux model viewing angle estimate lies above the maximum value allowed by the optically observed $\beta_j^{\text{app}} = 6.1$ motion at HST-1, and the average viewing angle estimate lies uncomfortably close to the maximum viewing angle. Thus, we adopt the smaller viewing angle from MLWH of $\theta \approx 17^\circ$ in order to relate angular scales to intrinsic scales, and we point out that all the recent model-dependent viewing angles lie within 3° of this choice.

At a viewing angle of $\theta = 17^\circ$, intrinsic lengths are ~ 3.42 times longer than apparent (projected) lengths, and the intrinsic jet opening angle between HST-1 (intrinsic distance ~ 240 pc) and knot A (intrinsic distance ~ 3180 pc) is $\Theta \sim 2^\circ$. At that viewing angle, the observed optical and radio superluminal motions of $\beta^{\text{app}} = 6.1$ and $\beta^{\text{app}} = 4.3$ imply intrinsic Lorentz factors of $\gamma = 10.9$ ($\beta = 0.9958$) and $\gamma = 4.6$ ($\beta = 0.9763$), respectively.

The jet is observed to be edge brightened from about 50 to 200 mas and also beyond $1''$. At angular distances out to ~ 80 mas, the edge-brightened radio jet exhibits quasi-periodic deviation of the brightness centroid (Reid et al. 1989) that likely indicates brightness alternation from one side to the other. Beyond HST-1 the jet is similarly edge brightened at 15 GHz, and side-to-side alternation in the radio brightness profile is apparent from HST-1 through knot D located at $\sim 3''_5$ (intrinsic distance ~ 906 pc) from the 15 GHz radio core (Owen et al. 1989). The jet also appears to contain twisted filaments from HST-1 to knot A (Lobanov et al. 2003) that are related to side-to-side variation in the brightness profile (Hardee & Eilek 2011).

The jet structure seen in the optical and NUV is quite similar to that seen at 15 GHz, but there are important differences in detail. The optical/NUV emission is more concentrated in the knots and toward the jet axis, and the outer edges of the jet are less well defined than in the radio (e.g., Sparks et al. 1996; Madrid et al. 2007). The major bright radio or optical knots can also be identified in the lower-resolution X-ray images (e.g., Perlman & Wilson 2005), but they can differ in position or structure from their radio or optical counterparts. At 15 GHz the projected magnetic field lies more or less along the edge of the jet flow (Owen et al. 1989), which may be indicative of a shear layer (Laing 1981). The optical/NUV knots also differ somewhat in polarization from the radio knots in that they tend to indicate magnetic field perpendicular to the jet flow and suggest the presence of shocks (Perlman et al. 1999). In general, the broader radio profile, the more centrally concentrated optical/NUV structure, differences in the polarization structure, and the slower observed motions in the radio suggest velocity shear across the jet, with the limb brightening observed in the radio being associated with the shear layer.

In this paper, we present results from monitoring observations of M87 at 43 GHz using the VLBA. Images from 23 epochs in 2007 and early 2008 are used to study the structure and dynamics of the inner jet. An image showing the average structure was made by stacking the 23 images and is used for the structure analysis. In that image, the limb-brightened jet is observed to 20 mas beyond the core. A faint structure, which extends slightly more than 1 mas beyond the core in the opposite direction, is speculated to be a counterjet

(Kovalev et al. 2007; Ly et al. 2007). We use transverse intensity slices to obtain the maximum intensity as a function of distance from the core and the width as a function of distance from the core. The individual images, and movies made with them, are used to study the rapid and complex changes near the core in an effort to extract velocities and possible acceleration. The 2008 observations showed a significant increase in flux density of the VLBA core that coincided with a flare seen at TeV energies as reported in Acciari et al. (2009). An early version of the 23-epoch average image, along with images from four individual epochs, was presented in that initial flare report. The flare led to an effort to catch additional cases of correlated radio and TeV flares, a result of which is that we have an ongoing series of roughly annual 43 GHz VLBA observations of M87. We report results, based on those observations to 2016, along with legacy observations going back to 1999, of a study of changes to the jet envelope on timescales of years. Preliminary presentations of some of our data, including an initial movie, have appeared in Walker et al. (2008, 2016), while an extensive analysis of the apparent velocity field in 2007 is given in MLWH.

The paper is organized as follows. In Section 2 we describe the observations. In Section 3 we present the observational results with subsections on the average structure (Section 3.1), on the rapid structural evolution (Section 3.2), on the polarized structure (Section 3.3), on the long-term evolution between 1999 and 2016 (Section 3.4), and on the counterjet structure based on an average image and on recent, high-sensitivity observations (Section 3.5). In Section 4 we examine some of the possible implications of our observations for jet structure and collimation properties that will provide a framework for future theoretical and numerical modeling of jet acceleration and collimation regions. Finally, we summarize and further discuss our results in Section 5.

For a listing of the symbols used in this paper, see Appendix A.

2. The Observations

2.1. Data Acquisition

The primary goals of the 43 GHz VLBA M87 project were to determine the apparent jet velocity and as much as possible about the dynamics of the jet close to the black hole. M87 had been observed before, but with some combination of inadequate resolution to see very close to the core and time sampling intervals that were too long unless the motions are very slow (e.g., Reid et al. 1989; Junor & Biretta 1995). For example, if the apparent motions are at the speed of light, a component would be moving at 4 mas yr^{-1} , which is about 20 beamwidths for the VLBA at 43 GHz. Some other sources have apparent speeds of more than 10 times that. If fast motions exist in M87 near the core as they do on larger scales, they probably had not been detected because they were seriously undersampled. So a pilot project was conducted in 2006 during which time intervals of between 3 days and 3 months were sampled. The results were somewhat ambiguous, but it was concluded that the changes that were seen could be followed with a 3-week sampling interval. Such observations were made throughout 2007. During that period, it became apparent that the sampling interval was too long—apparently related features moved two or more beamwidths between observations, and relating features was difficult. In early 2008, the observations

were continued at about 1-week intervals. Despite the use of dynamic scheduling, the short interval forced the use of less optimal observing conditions, so the data quality in 2008 was not as high as in 2007. Many sessions had missing antennas, which is not tolerated well when imaging a complex source with the sparse UV coverage of the VLBA. The primary data set for this paper is the first 11 epochs from 2007 and 12 epochs from 2008. One additional epoch, 2007 November 2, is shown, but the remaining five 2007 epochs have technical problems, so they are not used in this paper.

The correlation between a TeV flare and a radio flare noted in Section 1 led to an ongoing effort to catch other such flares in the hopes of further constraining the TeV emission location and mechanism. The TeV instruments could only observe at night, which constrains the coordinated observations of M87 to happen during the early part of each year. Observations were made with the VLBA once or twice each year to monitor the ambient condition of the radio jet. If a high-energy flare was seen, additional observations were triggered. There were triggers in 2010 and 2016, but no clear correlated radio flare was found in our data. With our data plus an additional observation of their own that had high flux density and was almost coincident with the TeV flare, Hada et al. (2012) reported a weak radio flare associated with the 2010 TeV event. In 2012, there was a period of enhanced TeV emission that failed to reach the trigger level for our project, but for which observations on the VERA and the European VLBI Network detected a significant radio flare (Hada et al. 2014). A by-product of our 2010 trigger response is that we have a six-image stack for 2010. In 2016, most of the follow-up observations were too short to make good images, so only three full-track observations are available, and one of those had poor observing conditions.

All of the observations reported here were made on the 10-station VLBA. Only the first two archival observations in 1999 and 2000 used additional antennas as noted in Appendix B. The first table in that Appendix gives the dates, image noise, and peak and total flux densities from the individual observations that contributed to this paper (not for all of the observations that were made). The long-term analysis also used four average observations, listed in the second table of Appendix B, one from each year with six or more individual observations.

The observations from 2004 and earlier are from the VLBA archive. They provide roughly annual information on M87 at 43 GHz back to 1999. Several of those observations involved co-authors on this paper, and several involved the use of M87 as a phase reference source for astrometric studies or for observations of nearby weak Virgo Cluster sources. Literature references for the projects involved can be found in Table 3. Most of those observations involved less, sometimes significantly less, time on source and less bandwidth than the post-2006 observations, so the image quality is generally not up to the same standard.

Starting with the pilot project in 2006, the observations involved a full track with data spanning most of the time that M87 was visible from at least a few stations of the VLBA. The total time on M87 at 43 GHz varied from about 5 to about 7 hr. The sources OJ 287, 3C 279, and occasionally 3C 84 or J1635+3808 were observed to use as polarization calibrators, fringe finders, and bandpass calibrators. Beginning in 2007, short phase-referencing scans on M84 were observed in an attempt to

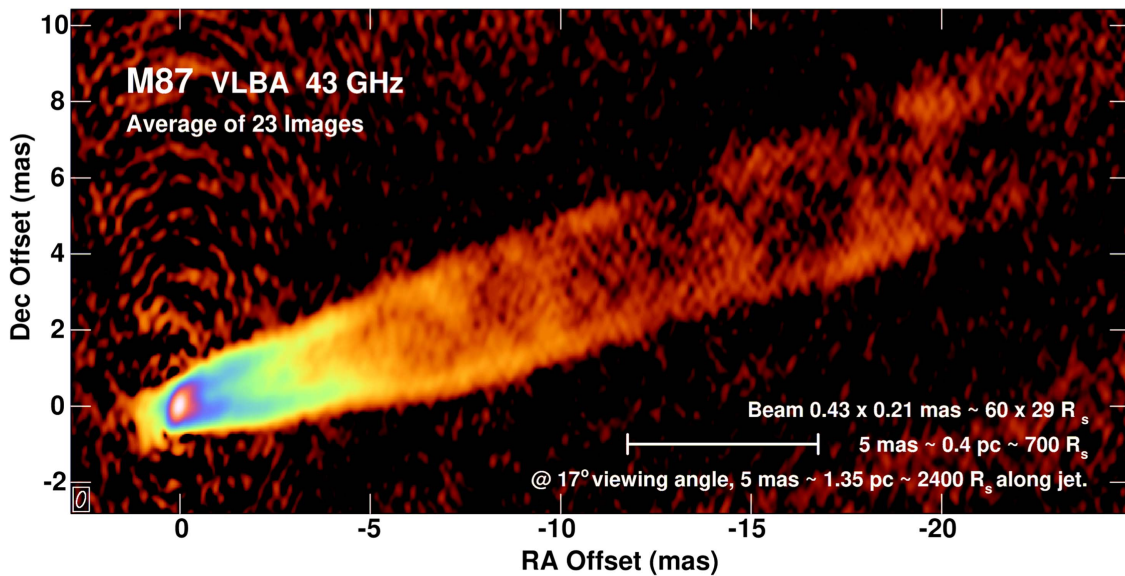


Figure 1. 23-epoch average radio image of the jet and counterjet in M87 based on data from 2007 and 2008. Angular to linear scales (in pc and in Schwarzschild radii R_s) are indicated for distances in the sky plane and for distances along the axis of the jet assuming that it is oriented at 17° to the line of sight. The beam with resolution 0.43×0.21 mas elongated in position angle -16° is shown at the lower left. The off-source noise level is $62 \mu\text{Jy beam}^{-1}$, and the image peak is 0.83 Jy.

measure the relative proper motions of M84 and M87 and to constrain any core wander. Such data are also available from 2001 October 12 and 2004 April 4 (Ly et al. 2007). To improve the quality of that astrometry, two to four roughly half-hour bursts of scans around the sky were added to calibrate the atmosphere starting with 2008 March 12. Beginning in 2009, roughly 20% of the M87 on-source time used 24 GHz to allow study of the spectral index and, possibly, Faraday rotation. The results from most of the polarization data, from the 24 GHz imaging, and from the M87/M84 astrometry will be reported elsewhere.

Various changes have occurred to the VLBA hardware over the years spanned by this project. The most important is that the recording bandwidth has been increased both by increasing availability of recording media and, eventually, by a significant hardware upgrade. The bandwidths used are shown in Table 3. Between the pilot project, recorded at 128 Mbps (16 MHz per polarization), and the most recent observations, recorded at 2048 Mbps (256 MHz per polarization), the bandwidth improvements alone gave a sensitivity increase of a factor of four. The data were correlated at the Pete V. Domenici Science Operations Center in Socorro, New Mexico, on the original hardware correlator up through 2009. A new Distributed FX (DiFX) software correlator that provides significantly enhanced capabilities (Deller et al. 2011) began operation in time to be used for our 2010 and later epochs. A description of the status of the VLBA hardware at any given time, at least since 2009, can be found in the Observational Status Summaries such as Van Moorsel (2014) and others that can be found at the same site.

2.2. Data Reduction

The data were reduced with the Astronomical Image Processing System (AIPS; Greisen 1995) following the usual procedures for VLBI data reduction, including correction for instrumental offsets using the autocorrelations, bandpass calibration based on strong calibrator observations, and

correction for atmospheric opacity based on the system temperature data. The a priori amplitude calibration depended on the gains provided by VLBA operations, which are based on results from regular single-dish pointing observations of Jupiter, Saturn, and Venus averaged over many months. Additional calibrations were done to enhance the M87/M84 astrometry and are included here for completeness. The Earth Orientation Parameters were updated to values more accurate than those available at the time of correlation. For many of the epochs, corrections were made for the ionospheric delays based on global ionospheric maps produced by the Jet Propulsion Laboratory, which are available at NASA’s Crustal Dynamics Data Information System (CDDIS). Atmospheric delay corrections were made using AIPS task DELZN based either on delays measured on sources around the sky in the aforementioned two to four bursts of about a half-hour duration or, for observations on or before 2008 March 6, on the residual fringe rates of the project sources and calibrators. These additional calibrations do not affect the images of M87.

The images of M87 were made using data that are both amplitude and phase self-calibrated. The flux scale for each epoch was set by normalizing the self-calibration gain adjustments to the a priori gains for observations above 30° elevation on only those antennas with good weather and instrumental conditions for that epoch. The flux densities are believed to be accurate to within about 10%, although the errors on the first few observations (especially 1999) may be higher. The phase self-calibration does not preserve source position, so, for analysis of the dynamics, the images were aligned on the image peaks. During the radio flare of 2008, the astrometric observations of the M87/M84 relative positions suggest that there is a small core shift as new components appear (F. Davies, et al. 2018, in preparation). For the 2008 event, the brightest we have seen by far, the effect was under $100 \mu\text{as}$, while at other times it is less than a few tens of μas , so the effect is small enough to ignore for purposes of this paper. For the imaging of this complex and fairly extended source, we found it important to use the robustness parameter

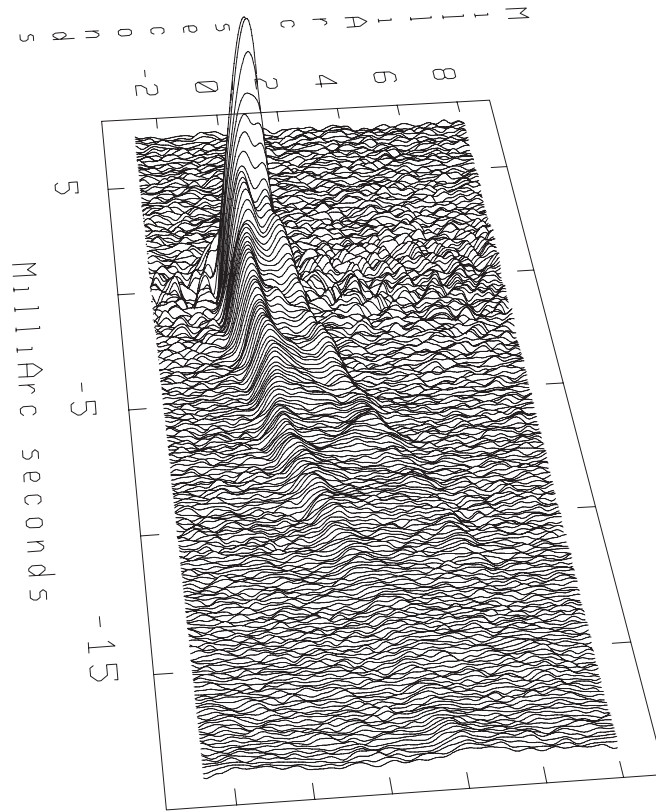


Figure 2. 3D slice profile rendering of the stacked 43 GHz VLBA image of M87 shown in Figure 1. The amplitude scale is logarithmic to allow low-level jet features to show without saturating the core region. The long axis (near vertical) is the R.A. offset. The short axis is the decl. offset in mas. The image is rotated by 75° to provide a good perspective on the edge-brightened jet structure.

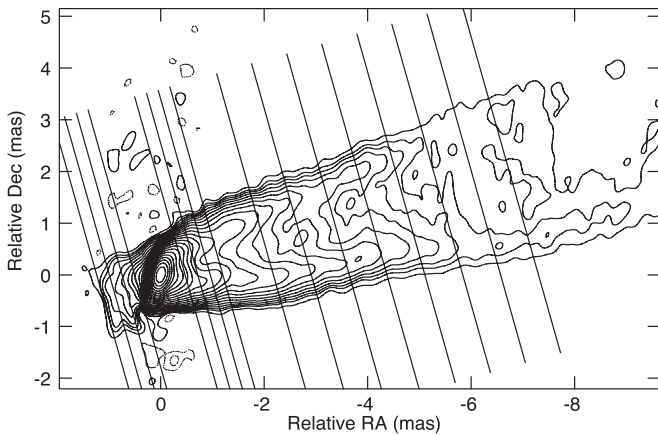


Figure 3. Locations of the sample intensity slices across the jet and counterjet shown in Figures 4 and 5 are shown overlaid on a contour map version of the image in Figure 1. The contour levels, in mJy beam^{-1} , are $-0.3, 0.3, 0.6, 0.85, 1.2,$ and 1.7 , increasing from there by factors of $\sqrt{2}$. The convolving beam for the CLEAN image is 0.43×0.21 mas elongated in position angle -16° .

(Briggs 1995) to gain some of the advantages of both natural and uniform weighting together, and to be able to significantly vary the dirty beam, which seems to help convergence during the self-calibration and imaging iterations. We also found that significantly better images could be obtained using the multiresolution capability of the imaging task IMAGR (Greisen et al. 2009). To aid comparison between epochs, nearly all images in this paper have had the point CLEAN components restored with a common beam of 0.43×0.21 mas, elongated

in position angle -16° . That resolution amounts to about $60R_S \times 30R_S$ with the adopted distance and black hole mass.

The observations were scheduled and correlated in a manner consistent with obtaining images of the polarized structure of M87. The primary calibrators for this purpose were OJ 287 and 3C 279. These sources were used to determine the instrumental polarization using the standard procedures in AIPS meant for application to resolved calibrators of unknown structure. For the electric vector position angle (EVPA) calibration, we have utilized results from the Boston University Blazar Project (Jorstad & Marscher 2016, and references therein), which includes the two calibrators. That project has many more sources, which aids the calibration significantly. We do not have simultaneous epochs, but past experience suggests that the absolute position angles will be the same when the images have the same total intensity structure, the same polarized intensity structure, and the same run of polarization angles along the source. When an epoch of the Blazar Project can be found with such a match for the total intensity and polarization structure for a calibrator, the EVPA calibration can be set to give the same polarization position angles for that calibrator. This method was used to calibrate the EVPA for both epochs for which we present polarization images later. Confidence in the method was gained from the fact that the two calibrators gave independent but consistent calibrations for each epoch and the polarization angles for M87 were consistent between the epochs. To our knowledge, this method of EVPA calibration has not been used before but should be useful for other projects.

For this project, obtaining a reliable polarization calibration proved to be possible but very time-consuming. It has only

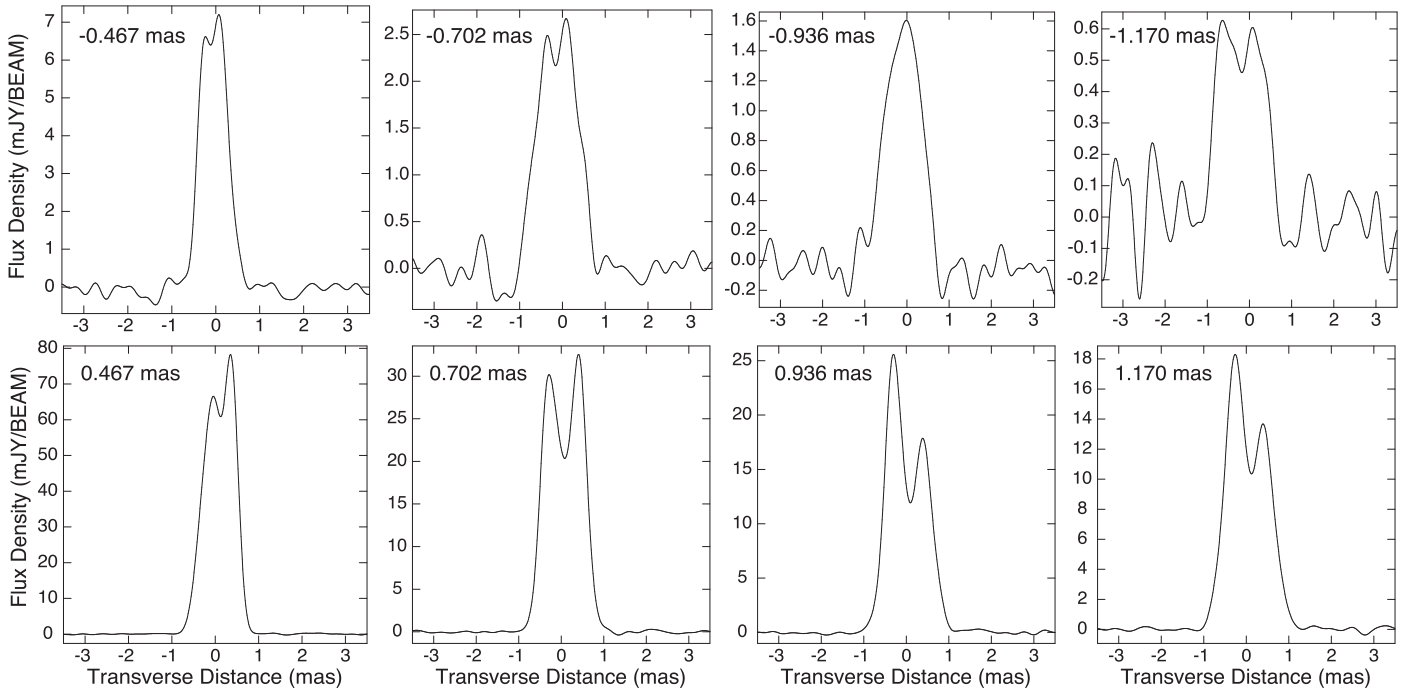


Figure 4. Sample intensity slices at distances of 0.467, 0.702, 0.936, and 1.170 mas with respect to the radio core in the counterjet (top row) and jet (bottom row) directions. The slice locations are shown in Figure 3. The northern edge of the jet and counterjet is at positive values on the transverse (mas) scale.

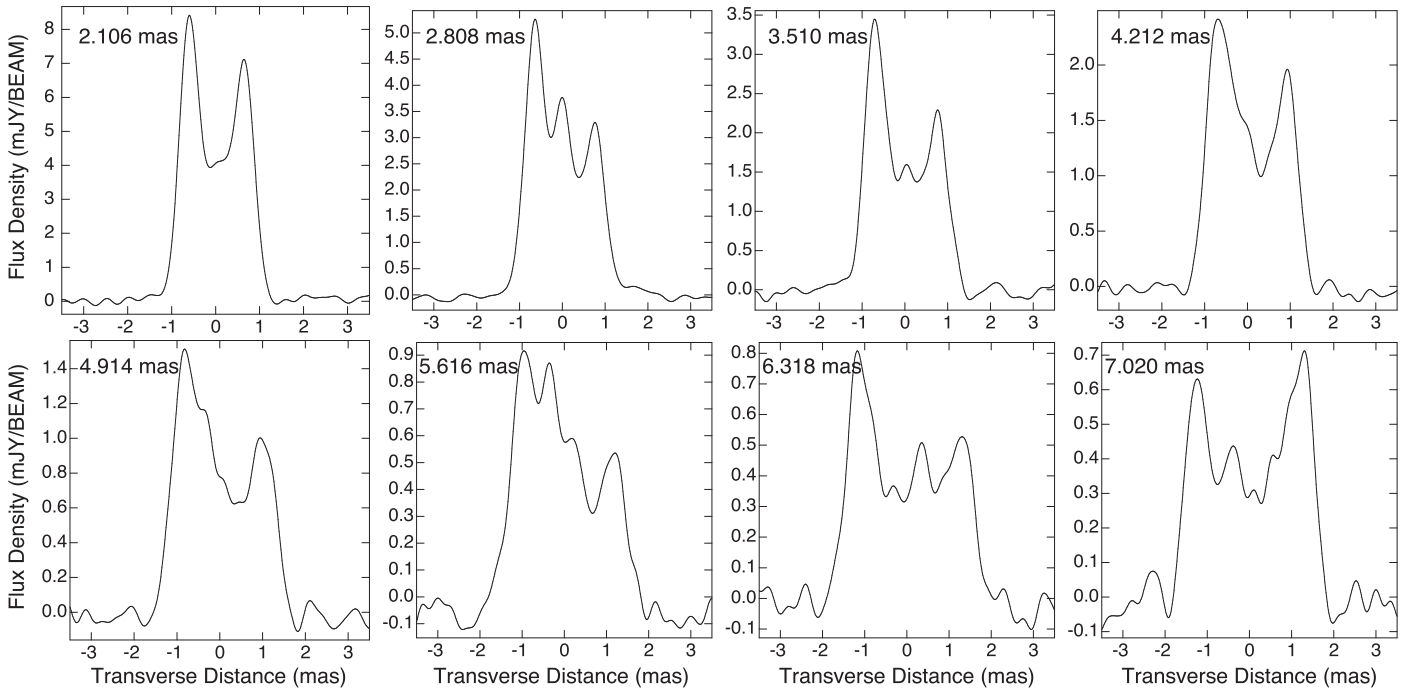


Figure 5. Sample intensity slices across the jet at positions 2.106, 2.808, 3.510, and 4.212 mas (top row) and at positions 4.914, 5.616, 6.318, and 7.020 mas (bottom row) with respect to the core as shown in Figure 3.

been completed to our satisfaction for two epochs, the results from which will be shown in Section 3.3. Those two epochs give similar results, so they likely reveal the nature of the polarization structure within about 0.5 mas of the core. To avoid significant additional delay in the publication of the total intensity results, we have chosen to defer a full polarization analysis. Once the rest of the polarization results

are available, we should be able to study time dependencies and to detect the polarization farther down the jet. In addition, the 24 GHz data should allow study of Faraday rotation along the jet. Detection of polarization farther along the jet depends on higher sensitivity, which can be obtained by stacking the 2007/2008 data and/or by using the recent, higher-sensitivity observations. Those recent observations are subject to

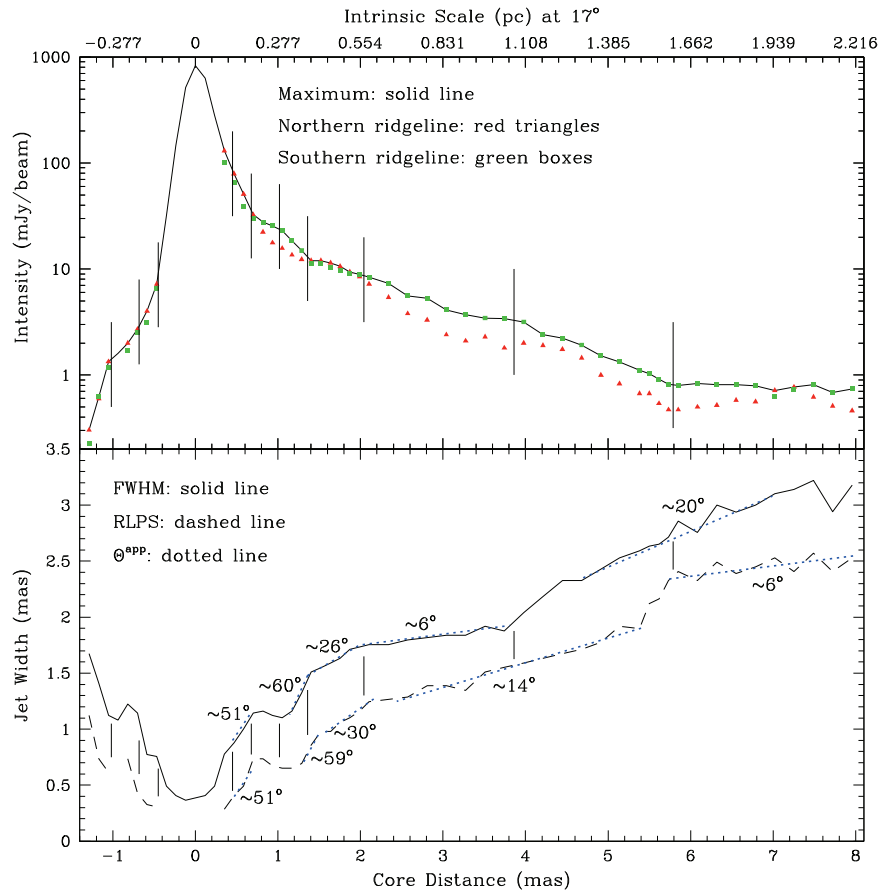


Figure 6. Top panel: maximum intensity (solid line) and maximum intensity associated with the northern (red triangles) and southern (green squares) ridgelines are plotted along with vertical lines indicating the first location not dominated by the unresolved core and subsequently the locations of change in the intensity decline along the jet. Vertical lines along the counterjet side are placed at the same core distance as the first three lines along the jet. Bottom panel: FWHM and the RLPS in mas, along with vertical lines transferred from the top panel. Simple linear fits to the apparent jet full opening angle, Θ^{app} , for both FWHM and RLPS are indicated by the dotted lines. Angular scale is indicated along the bottom axis, and intrinsic scale for the jet at 17° to the line of sight is indicated along the top axis.

frequency-dependent instrumental effects within our observing bands, which, because of software limitations (since fixed), hindered our initial calibration attempts.

3. Observational Results

The results of our M87 VLBA observational program are presented in this section. There are five subsections. Each subsection begins by presenting images that address a different aspect of the information available from the observations. Then the images are analyzed to extract more quantitative information that should help us understand the nature of the inner jet. Further discussion of what is learned from the data is deferred to Section 4.

Section 3.1 presents an average intensity image based on the 2007 and 2008 data, showing the persistent structure. An analysis based on slices is used to extract some of the detailed features of the jet shape, which can shed light on the jet propagation near the core.

Section 3.2 shows the individual images from the 2007 and 2008 observations. These are the main movie observations, and the movies are available in the online version of the paper. An effort is made to measure component motions using traditional, component-tracking methods. This is not as sophisticated as what was done in MLWH, but it provides added confidence in

the detection of superluminal motion and of acceleration very near the core.

Section 3.3 presents the polarization results from the two epochs from 2007 for which we already have a successful polarization calibration. There is a systematic structure to the polarization near the core, which suggests a toroidal field geometry.

Section 3.4 gathers the early observations, from before 2007, plus the results from ongoing efforts to catch more cases of activity related to TeV flares since 2009, to provide roughly annual images between 1999 and 2016. A movie based on these results is available in the online version of the paper. The jet is shown to move transversely over a period of several years. An analysis of that transverse motion, including derivation of a propagation speed of the pattern that is that sideways motion, is presented.

Section 3.5 uses the inner few mas of an average of nearly all our data over the full 17 yr, along with images from two of the recent, high-sensitivity observations, processed specifically for high resolution, to delineate the structure of the counterjet.

3.1. Average Intensity

A total of 23 images were used to make the movies showing the dynamics of the inner M87 jet that are presented in Section 3.2. Those images have been averaged to improve the

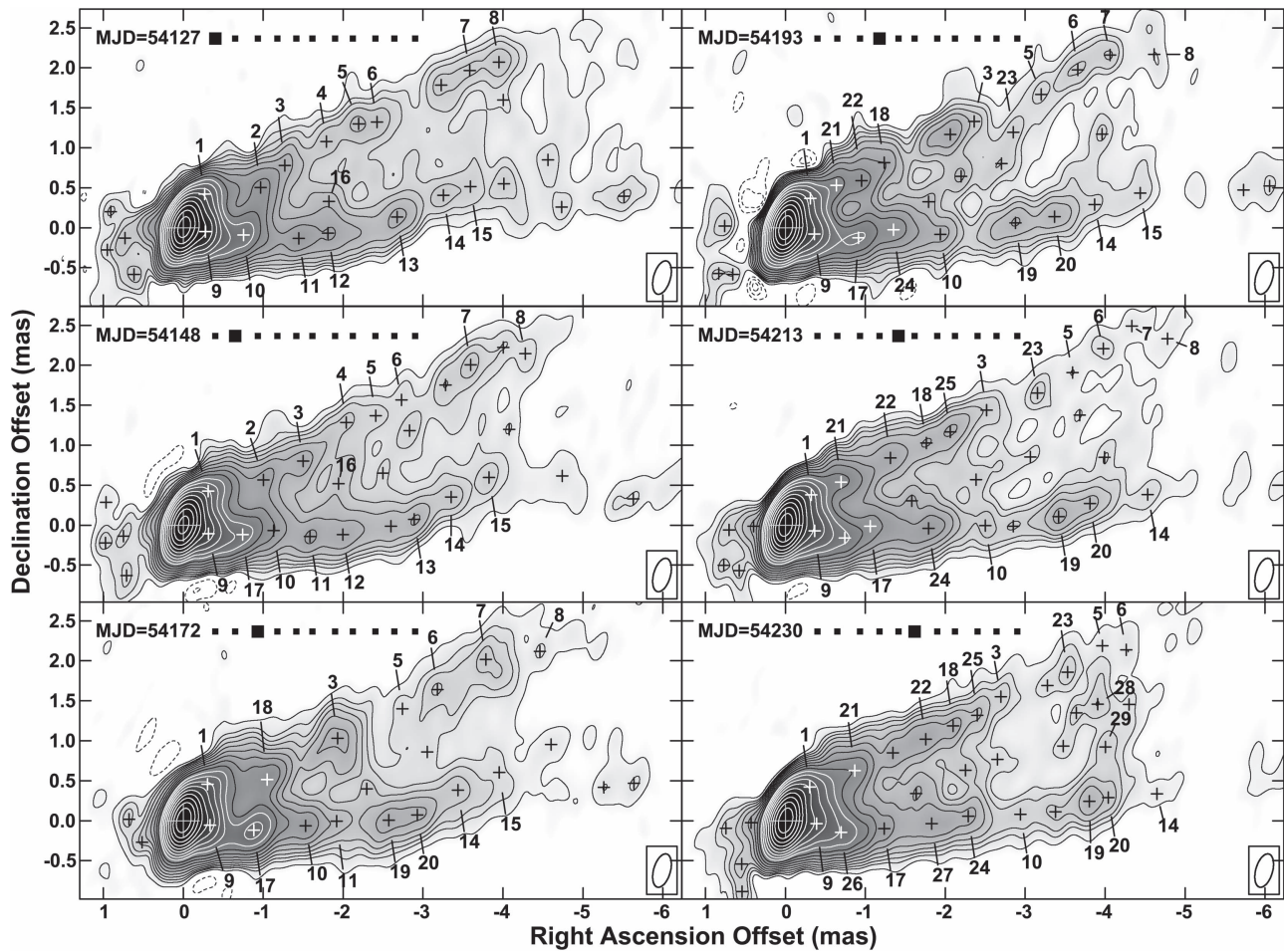


Figure 7. Contour/gray-scale plots of observations 1–6 of those that were made of M87 with the VLBA at 43 GHz during 2007 at about 3-week intervals. The convolving beam size used was 0.43×0.21 mas elongated along position angle -16° . The contour levels (mJy beam^{-1}) are $-1.4, -1.2, -1, 1, 1.2, 1.4, 1.7, 2, 2.4, 2.8, 3.4, 4, 4.8, 5.7, 6.7, 8, 9.5, 11.3, 13.4, 16, 19, 23, 27, 32, 38, 45, 91, 181, 362,$ and 724 . The image off-source noise level is between about 0.17 and $0.25 \text{ mJy beam}^{-1}$. Components, identified by eye, are marked with plus signs. Numbers are for components that appear to be related between epochs based on proximity and other cues in the structure.

sensitivity and to show the persistent structure of the subparsec M87 jet as seen at 43 GHz over a period of 1.2 yr in 2007 and 2008. The detailed structure that varies from epoch to epoch is smeared out by the averaging process. The average image is shown in Figure 1. At a viewing angle of $\theta = 17^\circ$, 1 mas in the sky plane corresponds to an intrinsic (i.e., deprojected) distance along the jet of 0.27 pc or about $480R_g$. Structure on the counterjet side, previously speculated to indicate a counterjet (Kovalev et al. 2007; Ly et al. 2007), extends a little more than 1 mas to the other side of the radio core. There are three positions located at $\sim 1, \sim 3.5,$ and ~ 13 mas from the radio core where the jet appears to recollimate and then subsequently expand. The image, along with those of Figures 2 and 3, suggests an oblique filament crossing the jet associated with a brighter feature near the jet center at ~ 2.5 mas from the radio core and possibly some fainter filaments crossing the jet at larger distances from the radio core. Overall the northern edge of the jet appears straighter than the southern edge. An average of all the epochs to be presented in Section 3.4 is not used for the analysis here because of smearing of the otherwise sharp edges caused by the transverse motions reported in that section. A 3D slice profile rendering of the 23-epoch total intensity image shown in Figure 2 shows more quantitatively the edge brightening seen in Figure 1. The southern edge is typically

brighter than the northern edge by a few tens of percent, but there is a wide scatter in the ratio, with the north being brighter in a few locations.

In order to examine in detail the transverse structure and compare counterjet to jet sides of the core, slices of the intensity image separated by 0.117 mas were made from -1.287 to 7.956 mas along the counterjet and jet axis, i.e., separated by about half a beamwidth. Figure 3 shows an intensity contour plot of the inner 10 mas of the image shown in Figure 1, with lines superimposed that mark the locations of the sample intensity slices shown in Figures 4 and 5. These sample slices are a subset of all of those calculated and used in the analysis. Here the slice axis is located at an angle of $15^\circ.76$ with respect to the R.A. axis. Figure 4 shows sample transverse intensity slices at 0.234 mas intervals in the inner ± 1.2 mas centered on the 43 GHz core. Similar transverse edge-brightened structure is evident on both jet and counterjet sides of the core, albeit on the counterjet side inside -1.2 mas there is one position where the maximum intensity is interior to the bright ridgelines (at -0.819 mas; not shown in Figure 4) and one position where the intensity is centrally peaked (at -0.936 mas; shown in Figure 4). On the jet side all slices inside 1.2 mas are edge brightened. The northern edge is brighter nearer the core along both jet and counterjet in the two

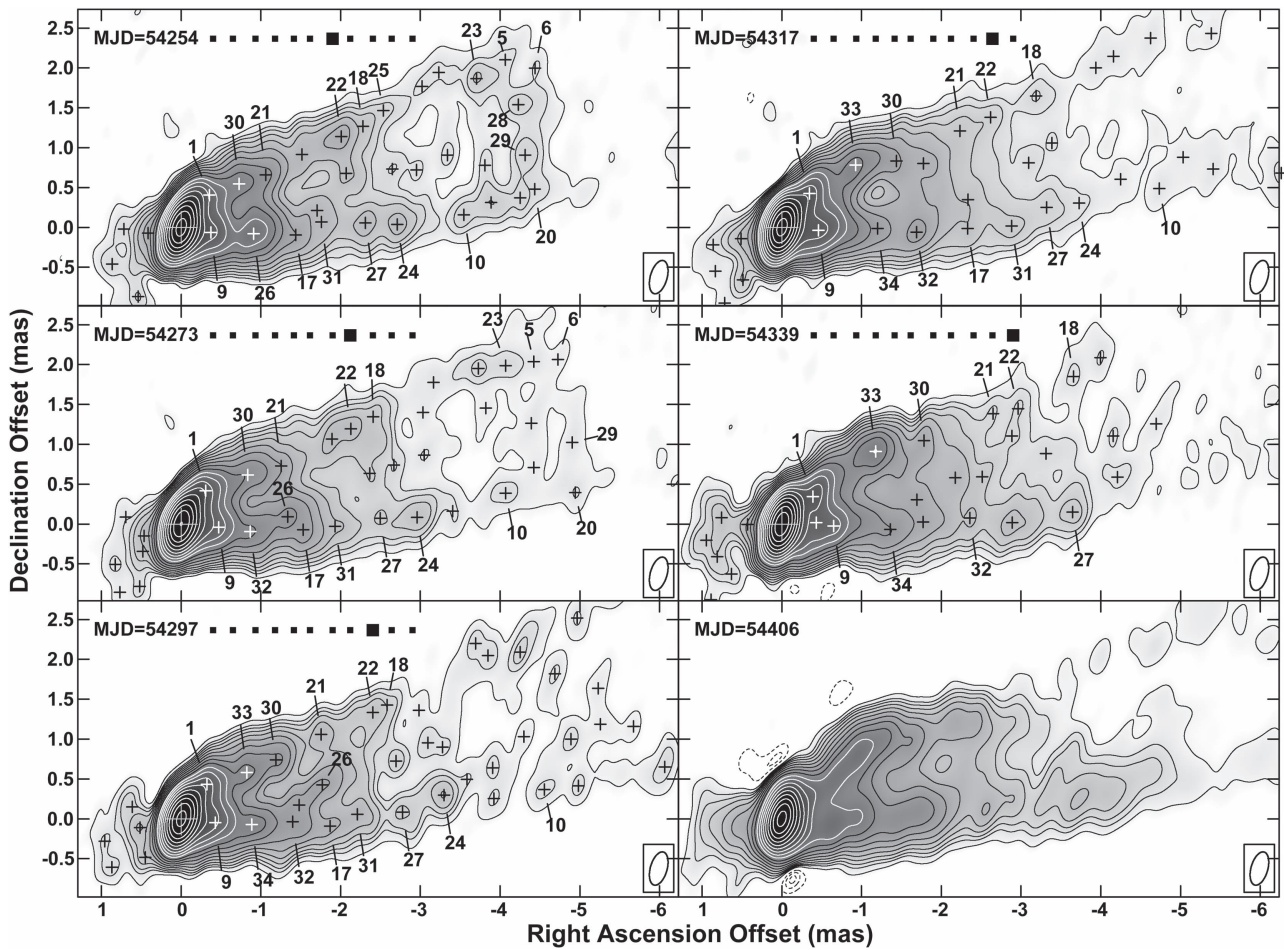


Figure 8. Contour/grayscale plots of observations 7–11 of those that were made of M87 with the VLBA at 43 GHz during 2007 at about 3-week intervals. The 11 images were used to make the movie shown in online animation Figure 9. The final image (bottom right panel) is from late in 2007. It is included for completeness, but other data sets near it in time have problems and are not yet fully reduced, so this image from late in 2007 was not used in the movie, the stack, and most of the analysis. The convolving beam size, contour levels, and marked components for all of the images shown here are the same as in Figure 7.

innermost slices. Along the jet the southern edge becomes brighter in the two slices farthest from the core, and there is weak indication of similar behavior along the counterjet in the slice farthest from the core. In the 23-epoch intensity image we cannot follow the counterjet farther from the core.

Figure 5 shows sample transverse intensity slices along the jet from ~ 2.11 to ~ 7.02 mas in 0.702 mas (approximately three beamwidth) intervals. The slices show the edge brightening apparent in the 23-epoch image (Figures 1) and 3D slice profiles (Figure 2). Additionally, these slices show that the transverse intensity profile is more complicated than double edge peaked, in particular between ~ 2.3 and ~ 3.5 mas (2.808 mas; shown in Figure 5) and also between ~ 4.5 and ~ 7.0 mas (bottom row in Figure 5). The structures responsible for these more complicated intensity profiles might be associated with filaments crossing the jet diagonally. Diagonal filaments are suggested by faintly visible structure in Figure 1 and are somewhat easier to identify in the 3D slice profiles of Figure 2 and in the contour plot underlying Figure 3.

The intensities associated with the bright northern and southern jet edge ridgelines along with the maximum intensity at each transverse slice position are shown in the top panel of Figure 6. Along the jet, the maximum intensity is always associated with one of the bright ridgelines. In the innermost ± 0.3 mas the intensity profile is dominated by the unresolved

core, although even at ± 0.2 mas the intensity on the jet side significantly exceeds that on the counterjet side. Vertical lines in the intensity plot are placed across the jet at the first location where the unresolved radio core does not significantly affect the intensity (~ 0.4 mas) and at larger distances where the intensity decline with distance changes slope significantly. Three vertical lines across the counterjet side are placed at the same radio core distance as the first three lines along the jet. Along the jet and counterjet sides of the core the second vertical line at $\sim \pm 0.7$ mas is associated with a significant reduction in the intensity decline, and the third vertical line at ~ 1 mas is associated with a significant increase in the intensity decline.

The bottom panel in Figure 6 shows that change in the slope of the intensity decline can be identified with change in the expansion rate along the jet and the counterjet side. The bottom panel shows the FWHM width, the ridgeline peak separation (RLPS) between the intensity peaks associated with the edge-brightened ridgelines, and simple linear fits to the apparent jet full opening angle, Θ^{app} , along the jet where the apparent full opening angle is defined as

$$\Theta^{\text{app}} \equiv \arctan(\Delta W / \Delta z),$$

where ΔW and Δz are the change in jet width and in core distance in mas, respectively. The symmetry in the opening

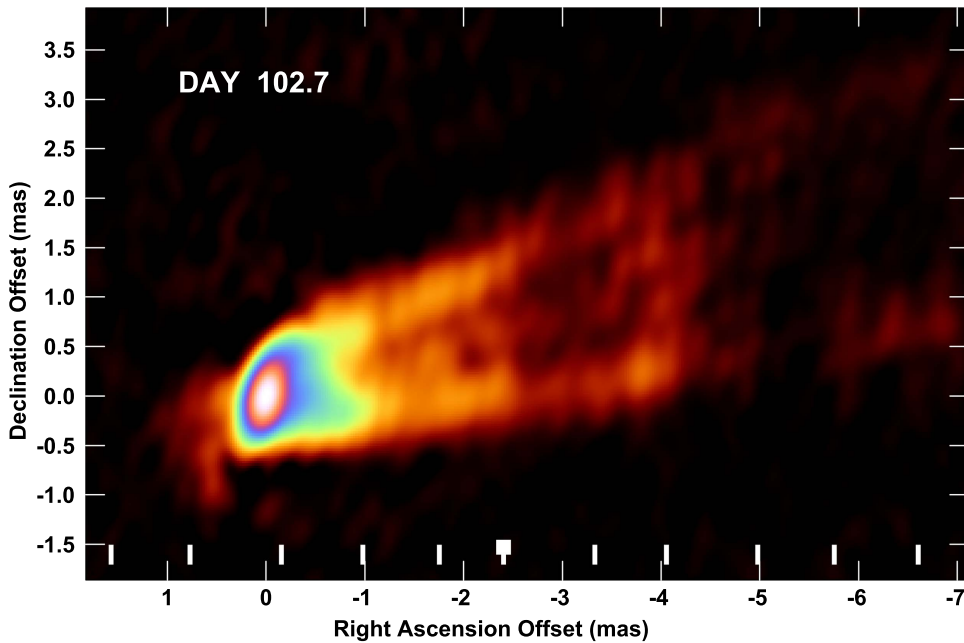


Figure 9. For the offline versions of this paper, this figure is a colorized version of one frame from the 2007 movie. Online, the figure is the movie, showing the first 11 images in sequence, with pauses proportional in time to the interval between epochs (typically 3 weeks). The underlying images are the same as those in Figures 7 and 8. The series of ticks along the bottom indicates elapsed time, and the moving box indicates which epoch is being displayed. The movie shows the actual observed epochs because confusing artifacts appear when interpolating undersampled data. The movie provides a clear visual impression of outward motion, but also of a rapidly evolving pattern that makes it hard to follow individual features over long periods.

(An animation of this figure is available.)

angle between the jet and counterjet sides, along with the similar edge brightening, confirms the identification of the faint structure as the counterjet. In both jet and counterjet we see an initial rapid opening, $\Theta^{\text{app}} \approx 51^\circ$, followed by a region in which the width decreases slightly, $\Theta^{\text{app}} \lesssim 0^\circ$. Subsequently both jet and counterjet increase in width rapidly with $\Theta^{\text{app}} \approx 59^\circ\text{--}60^\circ$, and the counterjet becomes too faint to follow farther. The obvious symmetry on either side of the radio core in the jet and counterjet structure at our 0.117 mas slice separation means that the radio core is located no more than half the slice interval, i.e., one-quarter the beamwidth, and <0.06 mas from the central engine. Thus, the radio core is located at $<8.5R_S$ from the central engine, consistent with the results of Hada et al. (2011).

Following the second rapid increase in width, the jet opening angle decreases first to $\Theta^{\text{app}} \approx 26^\circ\text{--}30^\circ$ and subsequently to $\Theta^{\text{app}} \approx 6^\circ\text{--}14^\circ$. Up to about 3.9 mas from the radio core both FWHM and RLPS widths change their slopes at about the same radio core distance, and to within the uncertainties Θ^{app} is about the same for FWHM- and RLPS-determined widths. This spatially synchronized behavior is broken beginning at ~ 3.9 mas, where the FWHM width increases rapidly out to ~ 4.4 mas without a similar increase in the RLPS width. The RLPS width shows a similar rapid increase beginning at ~ 5.5 mas and extending to ~ 5.8 mas. It is unclear whether these differences between the two width measurements are significant or just reflect uncertainty in the measurement methods, especially given the weakness of the northern ridge relative to the center, to the large brightness difference between the sides, and changes occurring along the southern envelope in this region. Beyond 5.8 mas the RLPS width indicates $\Theta^{\text{app}} \approx 6^\circ$, similar to the parsec- and kiloparsec-scale jet

opening angle. The implications of these structures will be discussed in Section 4.1.

3.2. Rapid Structure Evolution

In this section, we present individual epoch images and movies made from them that allow detailed studies of the structural evolution of the M87 jet near the core. The structure is complex and rapidly evolving and is not easily described as a series of moving features. The most convincing way to see that there is significant outward motion is to view the movies that give a strong visual impression of such motion. Despite the difficulties, we perform a traditional component motion analysis for the 2007 and 2008 data and show the results here. For a full velocity analysis of our 2007 data using more sophisticated techniques that can identify multiple, overlapping velocity fields, see MLWH.

3.2.1. Intensity Images

Figures 7 and 8 show the total intensity contour plots from the 11 epochs at about 3-week intervals between 2007 January 27 (MJD 54,127) and 2007 August 26 (MJD 54,339). The line of squares next to the dates gives a visual representation for the time of each epoch, especially if the images are viewed as a movie. The filled square representing the particular epoch shown in each panel is enlarged. Over this period the standard deviation (SD) of the 43 GHz flux from the core (inner 1.2 mas) was $\sim 5\%$, not significantly above the noise and uncertainties. There are significant changes to the intensity along the edges and down the center line of the jet. Significant change is also seen in the intensity of the counterjet. Some of the variation is the result of instrumental effects, but other variation is the result of true intensity changes that may be related to motions

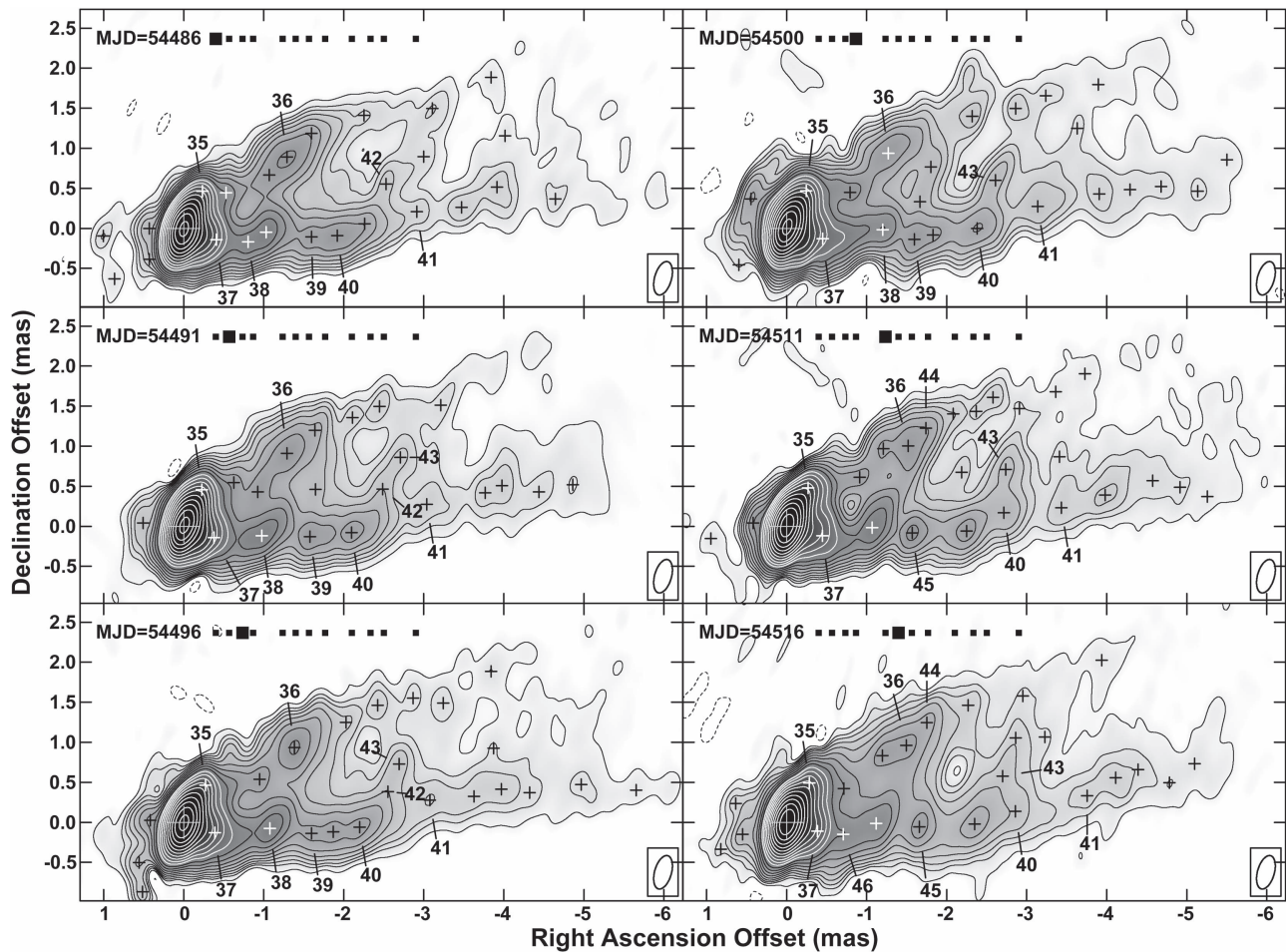


Figure 10. Contour plots of the total intensity of M87 at 43 GHz for the first six epochs at about 1-week intervals observed in 2008. This set starts on 2008 January 21 and ends on 2008 February 20. The beam dimensions, contour levels, and meaning of the marks are the same as for Figure 7.

along the jet. True structural changes are large enough that it is difficult to connect features from epoch to epoch when sampled at 3-week intervals.

A movie of the color image versions of the 2007 images is shown in online animation Figure 9. Offline, that figure is a sample frame from the movie. Interpolation is not used for the movie because the typical motion in 2007 between epochs is about 2.5 times the beamwidth and interpolation leads to distracting artifacts in the structure or the noise depending on how the interpolating is done. Viewing the movie is the best way to see the jet motions.

Observations continued between MJD 54,363 and 54,464 at 3-week intervals, but most have issues that complicate processing. Those issues have been partially overcome for the observation on 2007 October 26 (MJD 54,406), which is shown as the last panel in Figure 8. This epoch is sufficiently isolated in time from the other epochs that it is not used in the time series analysis or the 23-image stack. It is included in the 49-image stack in Section 3.5 on the counterjet. Technically this image is of interest because the observations were made at four frequencies (39.4, 41.3, 43.1, and 44.8 GHz) in an attempt to improve the UV coverage. The benefit of four frequencies was not fully realized because the two stations giving the longest baselines were degraded—one was out for maintenance, while the other had poor weather.

In Figures 7 and 8, plus signs indicate the visually determined positions of local maxima in the total intensity. An attempt to relate these features from epoch to epoch was made by blinking rapidly back and forth between the epochs. The attempt is hampered, as noted above, by the large motions between epochs. But a variety of visual cues, including the peak location and also aspects such as major dips in the ridgeline, made it possible to identify a significant number of components. Each feature that appeared related in three or more successive epochs was given a number. The motions of these components are analyzed in Section 3.2.2.

Figures 10 and 11 show total intensity contour plots of M87 for 12 epochs at intervals of about 1 week from 2008 January 21 to 2008 April 5. These plots are similar to the images shown in Figures 7 and 8 for the 2007 data, although the observing interval is significantly shorter. Feature identification was done in the same manner as for the 2007 data, and the results are included in our motion analysis. In principle, with the shorter interval, it should have been easier to relate features between epochs. But, as noted in Section 2, many of the images were of lower quality than those in 2007, so feature identification was as or more difficult. A movie of the color image versions of the 2008 images is shown in online animation Figure 12. Offline, that figure is a sample frame from the movie. Due to the lower quality of many of the images, the impression of motion is not

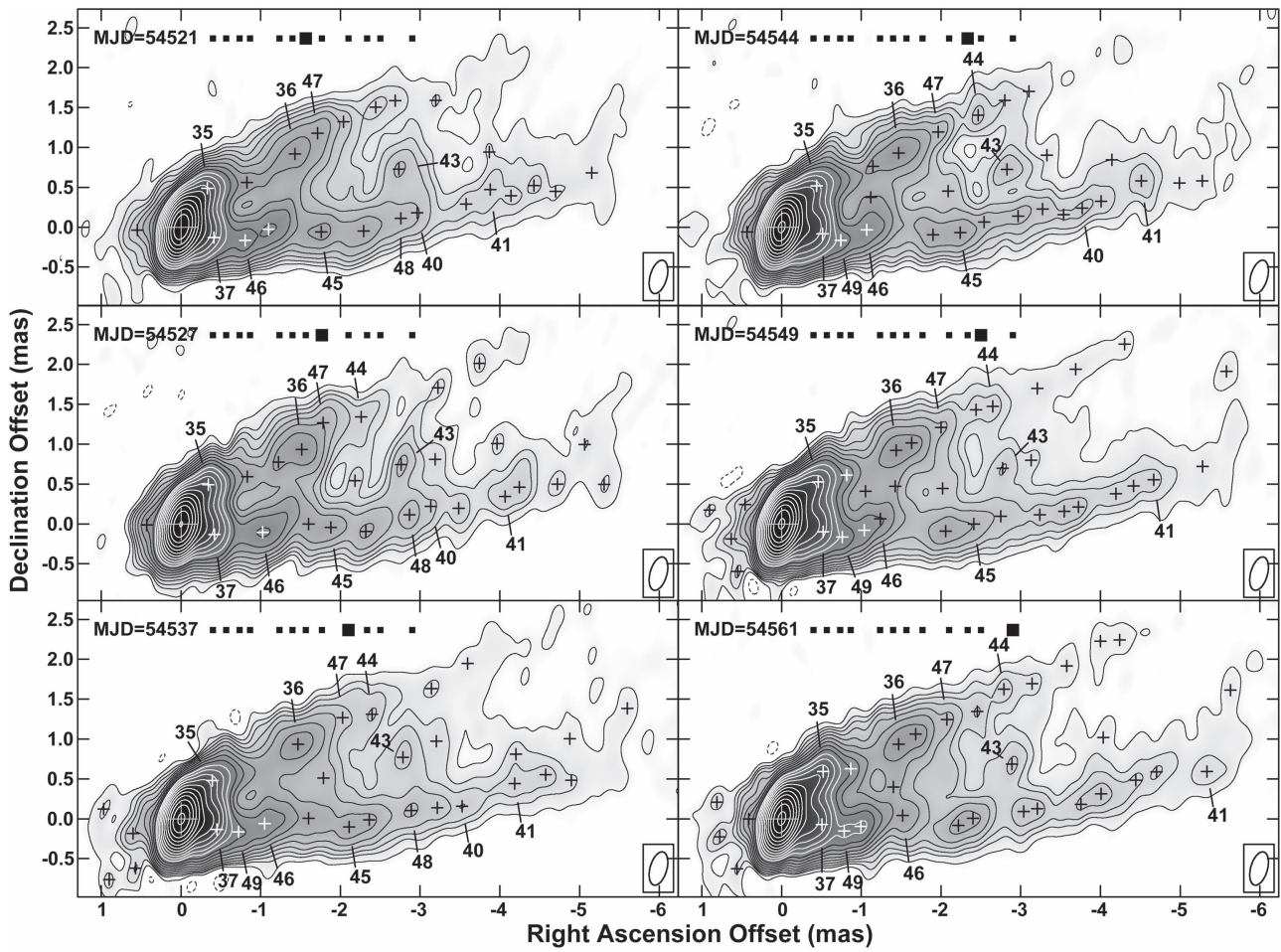


Figure 11. Contour plots of the total intensity of M87 at 43 GHz for the last six epochs at about 1-week intervals observed in 2008. This set starts on 2008 February 25 and ends on 2008 April 5. The beam dimensions, contour levels, and meaning of the marks are the same as for Figure 7.

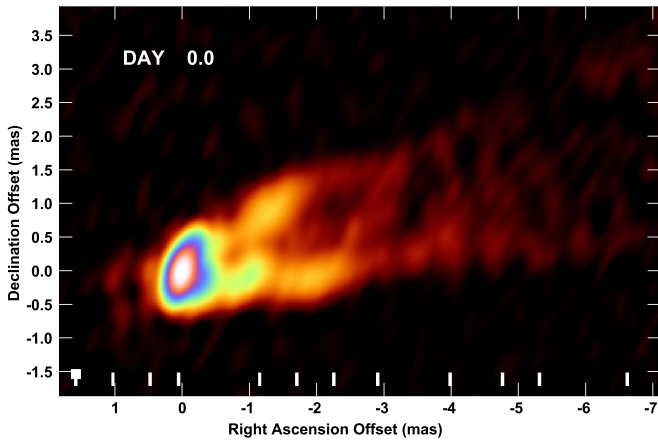


Figure 12. For the offline versions of this paper, this figure is a colorized version of one frame from the movie made from the 2008 data. Online, this figure is a movie showing the 12 images in sequence, with pauses proportional in time to the interval between epochs (typically 1 week). The underlying images are the same as those in Figures 10 and 11. The series of ticks along the bottom indicates elapsed time, and the moving box indicates which epoch is being displayed. The data quality was not as good as in 2007 because tight observing date constraints precluded waiting for better weather. Three epochs were so degraded that the images were not included, as evidenced by gaps in the time sequence. Despite these degradations, the movie still gives a clear visual impression of outward motion.

(An animation of this figure is available.)

as strong as with Figure 9, but the impression of motion is still present.

Serendipitously, TeV flaring occurred during the first 2 weeks of 2008 February, and it is around this time that a significant long-term increase in the core intensity at 43 GHz began. By 2008 April the core intensity had increased by 60% relative to the pre-TeV flaring average. Over the same time period the jet edges first brighten near to the core, with brightening extending outward over time. The increased brightening along the jet edges inside 1 mas can be seen by comparing the panel for January 21 in Figure 10, from before the TeV flaring, to the panel for April 5 in Figure 11. It is even more clear in the difference images shown in Figure 3 of Acciari et al. (2009).

3.2.2. Component Motion Analysis

Figures 7–8 and 10–11 show a jet structure that is complex and rapidly evolving. The details of the structure, especially in the regions farther from the core, are somewhat uncertain because of the high dynamic range required to image the jet in the presence of the bright core, the complexity of the overall structure being imaged with limited UV coverage, and the unfortunate loss of one or more antennas in some epochs, especially during 2008. The fact that many of the marked features in the figures are not numbered is an indication that the

M87 Components Along Northern Edge

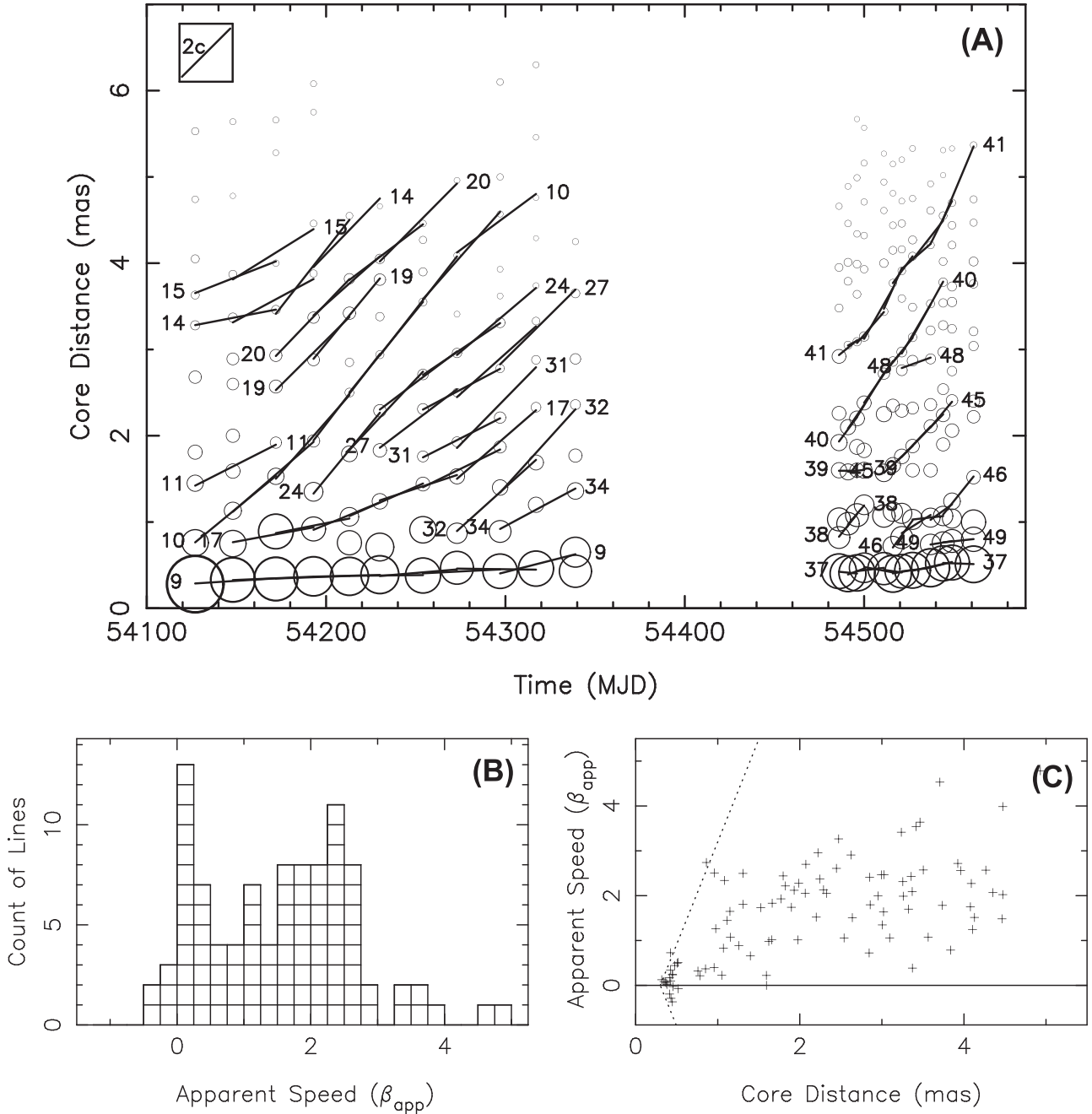


Figure 13. (a) Positions of components that lie along the southern edge of the M87 jet as indicated in Figures 7, 8, 10, and 11 as a function of time (for reference, 2007 January 1 is MJD 54,101) are marked by circles whose area is proportional to the component peak flux density. Where three components have the same number in successive epochs, a fit was done for speed and position. Each such fit is represented by a line segment in the figure. (b) Histogram of the number of line segments in panel (a) as a function of apparent speed $\beta^{app} = v^{app}/c$. There are concentrations of speeds near zero, mostly from positions near the core, and concentrations at $\gtrsim 2c$, although intermediate and some faster speeds are also seen. (c) Plot of apparent speed with core distance (midpoint of line segment). The dotted line is the right boundary of the exclusion region resulting from the requirement that the first of the three points in a line segment be resolved from the core. The boundary shown is for the 3-week cadence of the 2007 observations. As is apparent from looking at panel (a), higher velocities are at larger core distances. For distances less than about 2 mas, an acceleration region, as identified by MLWH, is seen.

structure is not easily described by long-lived discrete “components.” However, we can present a component motion analysis based on the marked and numbered features.

Figures 13 and 14 show the results from such an analysis of the features seen in Figures 7 through 11. The two figures show results for the southern and northern edges of the jet, respectively. There were insufficient features for a similar

analysis along the jet center line or in the counterjet. In each figure, panel (a) shows a time series of the positions of all the marked features. When three features have the same number in successive epochs, the feature is assumed to correspond to the same moving component. The feature is then connected by a line segment where the line segment is the result of a linear fit to the position and apparent speed of the component. The other

M87 Components Along Northern Edge

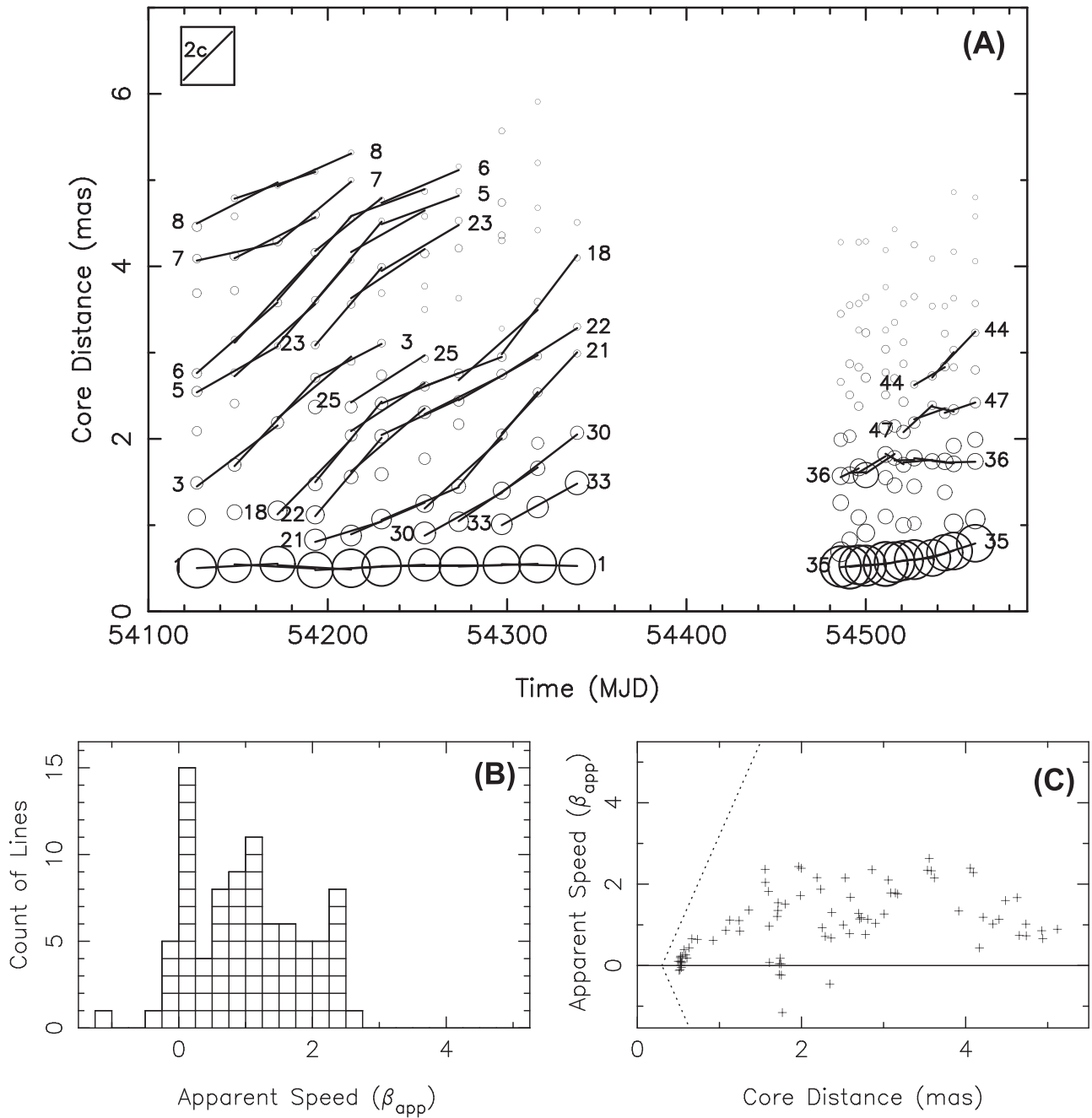


Figure 14. Similar to Figure 13, but using data from components along the northern edge of the jet. See the caption of Figure 13 for details. The speeds seen in both edges are discussed in the text, along with comparison with results from MLWH. Compared to the southern edge, the northern edge shows more of a preponderance of intermediate speeds with a broad peak near $1c$. As along the southern edge, an acceleration region is seen at distances less than about 2 mas.

two panels are based on those line segment results. Panel (b) shows a histogram of fitted speeds for the line segments. Panel (c) shows the speed plotted as a function of core distance where the position of the midpoint of a line segment is used for the core distance. There is an exclusion region for fast components near the core because the first feature closest to the core must be resolved from the core. The dotted line indicates the boundary of the exclusion region assuming that the first point must be 0.4 mas from the core and that the observing cadence is once per 3 weeks, which is appropriate for 2007. For 2008 with

an observing cadence of once per week, the boundary of the exclusion region is steeper.

The data show a wide scatter in apparent speeds. The speeds range from slightly negative to near $5c$. Near the core, the speeds are slower with faster speeds at larger core distances. The histograms show concentrations near zero and near $2.3c$ for both edges, with an additional concentration near $1.0c$ along the northern edge. The feature closest to the core is moving very slowly if at all, but that feature is generally just the inner part of the jet that is not well resolved from the core. Toward

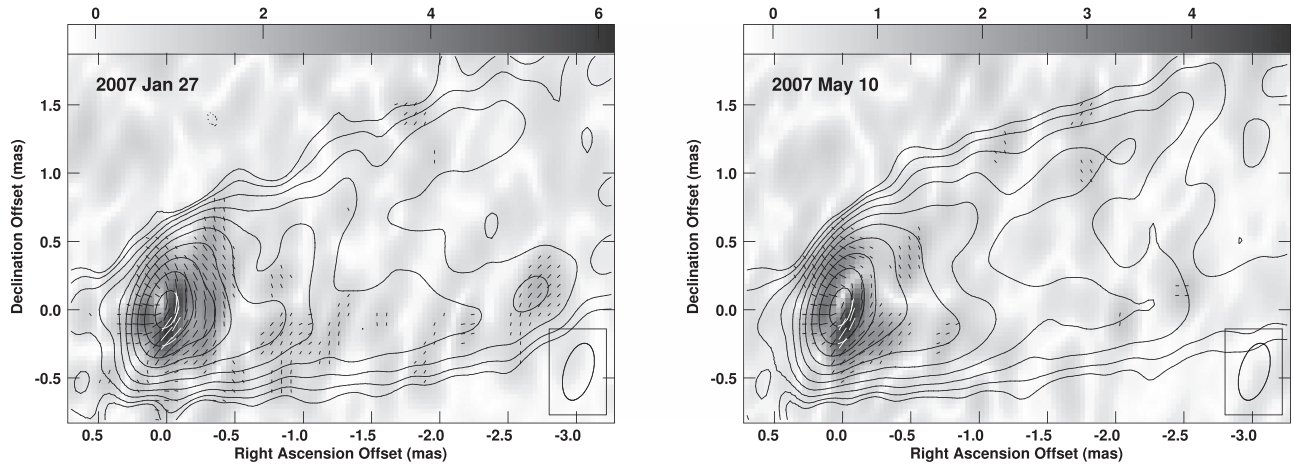


Figure 15. Magnetic field vectors overlaid on total intensity contours and a polarized intensity grayscale image for the 43 GHz VLBA observations made on 2007 January 27 (MJD 54,127) and 2007 May 10 (MJD 54,230). The contour levels are 1, 2, 4, 8, 16, 32, 64, 128, 256, and 512 mJy beam⁻¹. The convolving beam, with a resolution of 0.43×0.21 mas, elongated along position angle -16° , is shown at the lower right. The peak total flux densities are 666 and 660 mJy beam⁻¹, respectively, while the peak polarized flux densities, at slightly different positions from the peak total flux densities, are 6.15 and 4.91 mJy beam⁻¹, respectively. The percent polarizations at the positions of the peak polarized intensity are 1.5% and 1.1% at the two epochs and rise to about 4% at about 0.4 mas along the jet ridges. The cutoff levels for plotting of the polarization vectors are 0.5 mJy beam⁻¹ for the total intensity (2.5 and 3.1 times the rms noise for the two epochs) and 1.0 mJy beam⁻¹ for polarized intensity (4.3 and 5.0 times the rms noise of the Q and U images for the two epochs). Both epochs show a consistent polarization structure near the core. On the jet side, the magnetic vectors wrap around the core. There is a minimum in the polarized intensity near the peak of the total intensity where the polarization direction jumps by about 90° .

the end of the data set, in 2008, the innermost northern feature (#35) does move away more decisively. That feature appears to be related to the radio flare in the core region that occurred around the time of the TeV flares seen between MJD 54,497 and 54,509 and is shown in difference images in Acciari et al. (2009). Here this feature is seen to have accelerated to $\beta^{\text{app}} \approx 0.64$ at ~ 0.8 mas from the core. For features farther from the core, there is a general trend for speeds to increase out to ~ 2 mas, reaching speeds $\beta^{\text{app}} \approx 2$ albeit with large scatter. Simply averaging all the points more than 1.8 mas from the core for both years gives results for the north and south ridges of $1.43c$ and $2.19c$ with SDs of $0.67c$ and $0.90c$, respectively. These averages correspond to 5.44 and 8.30 mas yr⁻¹. But averages may be too simplistic if, for example, additional acceleration is involved.

Our results can be compared to those presented for the 2007 data by MLWH. That study used the Wavelet-based Image Segmentation and Evaluation (WISE) velocity field analysis combined with a stacked cross-correlation analysis (Mertens & Lobanov 2015) to analyze the velocity field in a manner that was able to pick out overlapping fast and slow motions. Velocities from the WISE analysis, as shown in Figure 3 of MLWH, show a wide scatter with predominantly slow speeds near the core and speeds over a wide range up to nearly $3c$ beyond about 2 mas. Visual inspection does not show clear evidence for multiple components. The velocity plots shown in our Figures 13 and 14 look similar in character. It was the stacked cross-correlation analysis in MLWH that helped delineate the velocity structure of the jet. The analysis found that, at core distances between 0.5 and 1 mas, the motions are in the range of $\beta^{\text{app}} = 0.2\text{--}0.5$ with the higher speeds in the north. Between 1 and 4 mas, there are two velocity components. The slower component has $\beta^{\text{app}} = 0.17$ (north) and 0.49 (south). The faster component has $\beta^{\text{app}} = 2.41$ (north) and 2.20 (south). Speeds were also determined along the center of the jet with values found between those of the northern and southern edges.

The stacked cross-correlation analysis found a clear division at about $\beta^{\text{app}} = 1.5$ between the fast and slow components. For comparison, using only 2007 data (the only data used by MLWH), our visually determined components at core distances greater than 1.8 mas have an average $\beta_{\text{N}}^{\text{app}} = 1.47$ with SD of 0.60 for the northern edge and $\beta_{\text{S}}^{\text{app}} = 1.79$ with SD of 0.56 for the southern edge. Similar averages for the WISE data in Figure 3 of MLWH for all points beyond 1.8 mas are $\beta_{\text{N}}^{\text{app}} = 0.91$ and $\beta_{\text{S}}^{\text{app}} = 1.26$. The WISE analysis clearly picks out more slow components than our visual analysis. Restricting the average to components that have individual speeds above $\beta^{\text{app}} = 1.5$ to try to focus on the fast component seen by MLWH, the averages for our data are $\beta_{\text{N}}^{\text{app}} = 2.04$ and $\beta_{\text{S}}^{\text{app}} = 2.06$, while they are $\beta_{\text{N}}^{\text{app}} = 2.05$ and $\beta_{\text{S}}^{\text{app}} = 2.10$ for the data from Figure 3 of MLWH. Thus, the data sets give essentially the same result for the faster components. In fact, they are remarkably close given the limitations of the data and of our visual analysis method. For further discussion of the velocity results, the reader is referred to Section 4.2 and to MLWH.

3.3. Polarization Images

Images of the polarized emission of a radio jet can provide much information about the magnetic fields in the jet. For that reason, all of our observations included the necessary cross-hand correlations and calibration observations to allow imaging of the polarization. Difficulties were encountered with the calibration, and a full polarization analysis has been deferred. But two epochs, 2007 January 27 and 2007 May 10, were successfully calibrated and imaged. The polarization structure within 3 mas of the core is shown in Figure 15 for those two epochs. Magnetic field vectors are shown under the assumption that they are rotated 90° from the measured electric field vectors and that there is no significant relativistic aberration or rotation measure. These assumptions will need to be checked because rotation measures high enough to matter (greater than about 5000 rad m⁻²) have been observed at other positions and frequencies in M87 (Zavala & Taylor 2002; Kuo et al. 2014). It may be possible to extract rotation measures

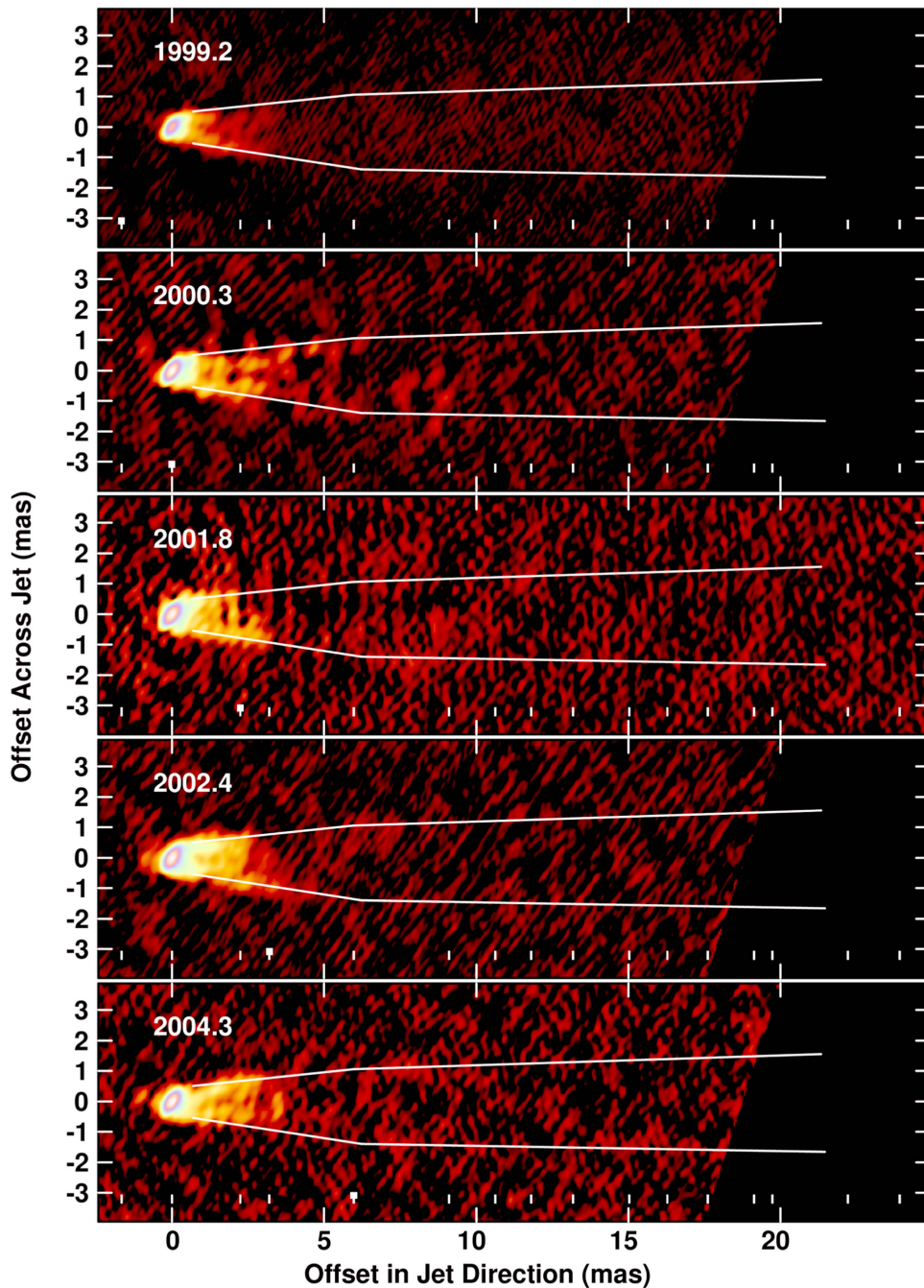


Figure 16. First five previously published epochs between 1999 and 2004 (Junor et al. 1999; Ly et al. 2007) of the roughly annual observations of M87 made between 1999 and 2016. All images have been rotated by -18° . The white lines indicating the jet edges on the 2007 image are there to aid visual detection of changes at different epochs. The images in Figures 16–18 are available as a movie in online animated Figure 19.

from our data, but that analysis has not yet been completed. The magnetic field vectors are superimposed on total intensity contours and a grayscale image indicating the polarized intensity. The polarization percentage varies from near zero close to the core, where the field direction flips, to about 4% about 0.4 mas from the core along the southern edge of the jet and along the northern edge of the jet in the first epoch. Farther along the jet, and closer to the core along the northern edge in the second epoch, the polarized emission is too weak for reliable detection in these two data sets. The peak polarized flux densities (noted in the figure caption) are seen about 0.15 mas southwest of the core. At those locations, the polarization percentages are 1.5% and 1.1% at the first and second

epochs, respectively. On the counterjet (east) side of the core, within the wings of the beam, the polarization is 1% to 2%.

The magnetic field orientation shows a consistent pattern at the two epochs. This might be expected, as there were no large changes to the intensity structure during this period. On the jet side of the core the magnetic field vectors are approximately perpendicular to the local jet axis. Rotation of the vectors between north and south edges reflects the wide jet opening angle. On the counterjet side of the core, the magnetic field vectors are approximately parallel to the counterjet axis, and again rotation between north and south edges reflects the wide opening angle. While the $\sim 90^\circ$ polarization angle change near

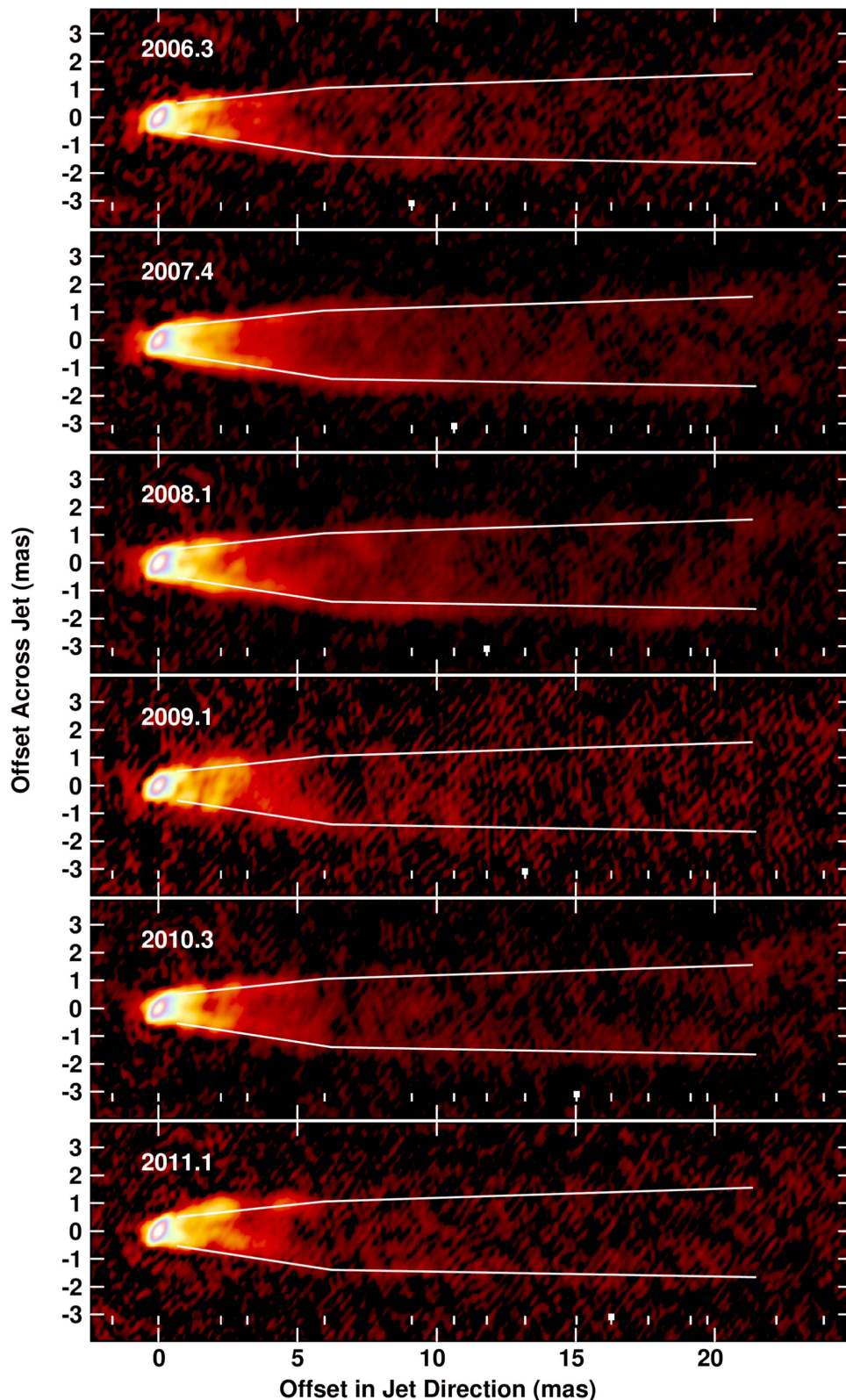


Figure 17. Middle six epochs of the roughly annual observations of M87 made between 1999 and 2016. The 2006.3, 2007.4, 2008.1, and 2010.3 images are actually stacks (noise-weighted means) of 6, 11, 12, and 6 images, respectively, taken within a few months of the indicated mean time. As in Figure 16, the white lines indicate the jet edges on the 2007 intensity image. Recall that the stacks will smear out variable structure and emphasize persistent structures. The images in Figures 16–18 are available as a movie in online animated Figure 19.

the core may reflect the magnetic field structure, it is also possible to get such an effect in VLBI sources as a result of the transition from optically thick to optically thin emission. A related opacity effect is expected to displace the radio core from

the actual black hole location. Such a shift for 43 GHz in M87 was measured by Hada et al. (2011) to be $41 \pm 12 \mu\text{as}$. Given that the polarized emission on the counterjet side of the core is within the wings of the convolving beam, it is possible that it

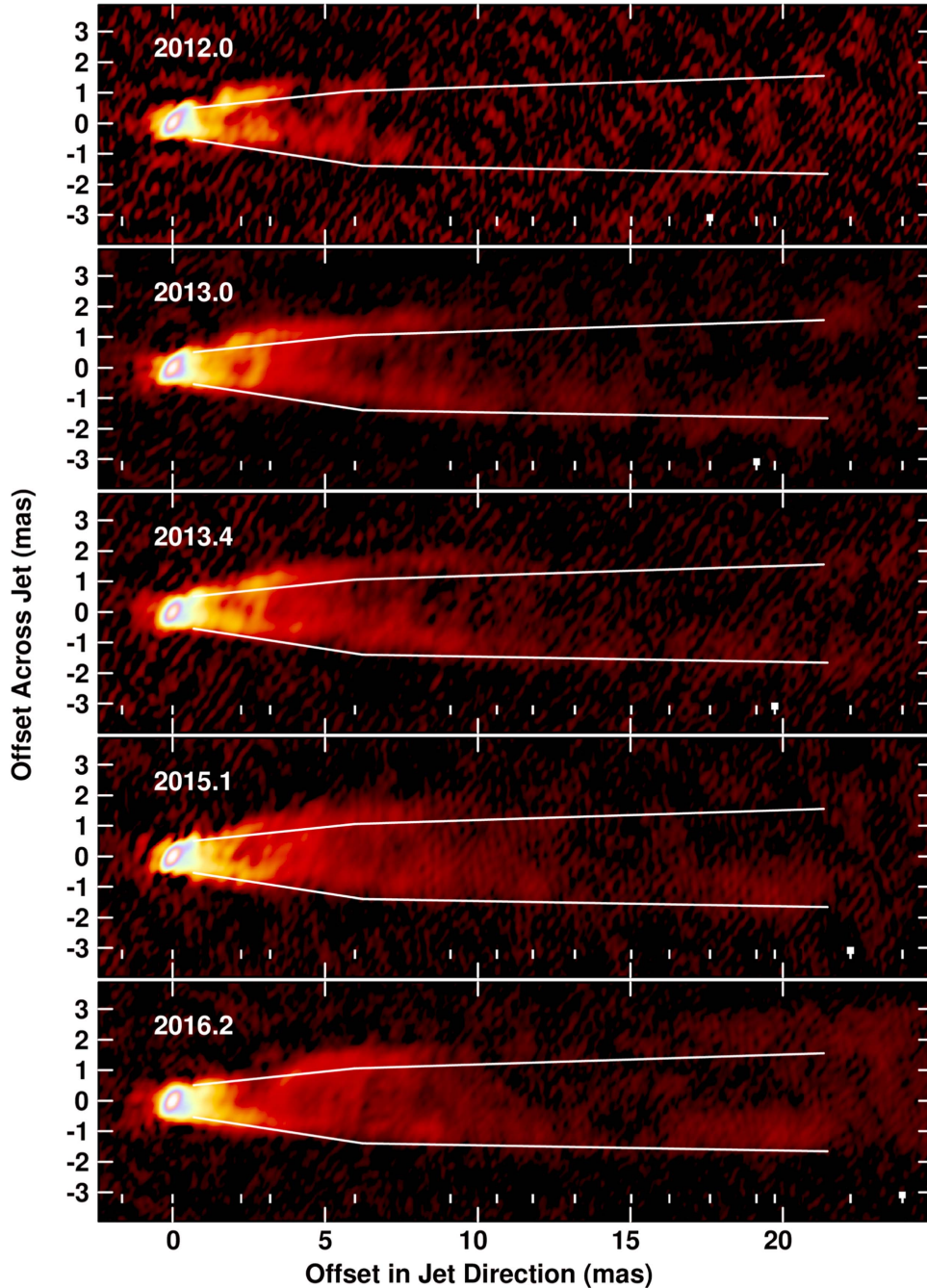


Figure 18. Final five epochs of the roughly annual observations of M87 made between 1999 and 2016. This group consists of single-epoch images (not stacks). The final four are based on observations made after the VLBA bandwidth upgrade. With typically eight times the bandwidth or nearly three times the sensitivity of the older observations, the individual epochs have noise levels comparable to the stacks in Figure 17. As single-epoch images, transient details are not smeared. Again, the white lines indicate the jet edges on the 2007 intensity image. The images in Figures 16–18 are available as a movie in online animated Figure 19.

originates in the portion of the jet between the black hole and the radio core, i.e., not from the counterjet. As noted above, the polarized intensity drops rapidly away from the core, but the percentage polarization rises over the short distance for which it is measured reliably. There is some suggestion that the magnetic field vectors are more flow aligned along the northern and southern edges of the jet at ~ 2.5 mas from the core, although this result needs to be confirmed with lower noise polarization data.

Magnetic field vectors that are wrapped around the core, reflecting the initial large jet opening angle, suggest a toroidal jet magnetic field geometry. However, modeling is needed to take into account the relatively small viewing angle to the line of sight, along

with possible optical depth, Faraday rotation, and relativistic aberration effects. The polarization data from our observations that have not yet been reduced should provide much higher sensitivity, allowing detection of polarization farther from the core. The data taken since 2009 will provide 24 GHz data to allow measurement of Faraday rotation. These improvements should eventually provide more information on the magnetic field structure.

3.4. Long-term Evolution

This project began as an effort to measure possible superluminal motions near the core of M87 by sampling significantly

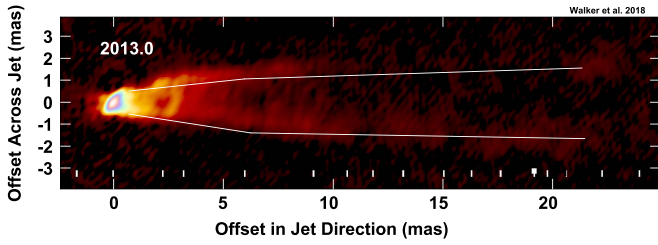


Figure 19. In the online version of this paper, this figure is a movie made from the roughly annual images shown in Figures 16–18. It gives a visual sense of the changes that occurred in the source between 1999 and 2016, including the side-to-side displacements. Those shifts are described in detail in Section 3.4.2 in terms of a linear shift and a sine wave, both functions of time, both of which propagate down the jet at a pattern speed. A fit to the offsets of the jet center from a nominal center line gives the parameters of these patterns and their pattern speed, which is fast, but not as fast as the faster-component motions. A pattern speed is also derived using a correlation analysis giving a similar result. For the offline versions of this paper, the image from 2013.0 is shown.

(An animation of this figure is available.)

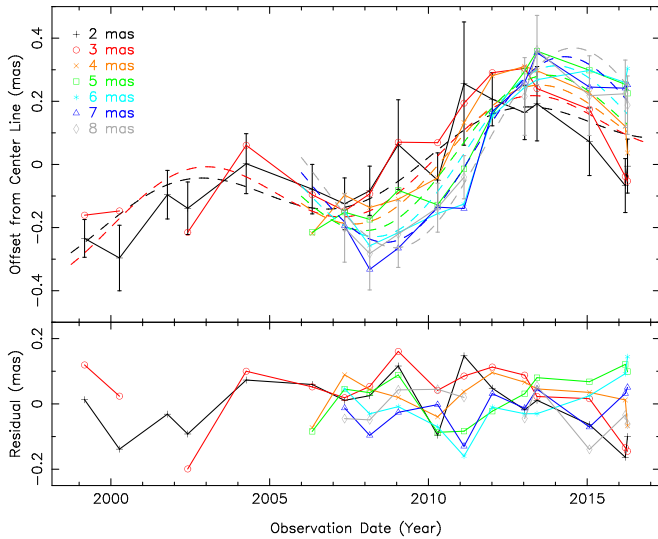


Figure 20. Measured offsets of the M87 jet center from a line extending from the core along position angle of -72° . The data used are the images shown in Figures 16–18 with one extra observation (2016 April 10 in Table 3) included at the end. Offset measurements are based on finding the outermost half and quarter power points on each side, relative to the peak on that side. “Error” bars are based on the separation of the two points on each side and do not vary much, so only those for the points at 2 and 8 mas are shown. Dashed lines are the results, for different core distances as indicated by color, of a least-squares fit for a model, described in the text, whose main components are a linear relation and a sine function, both with time, both propagating down the jet. The “errors” were used as the weights in the fit. The apparent propagation speed, with its formal error from the fit, is $\beta_{pp}^{app} = 0.89 \pm 0.18$. The bottom panel shows the residual data that are the measured data points with the fitted model subtracted.

faster than had been done in previous projects. But slower, longer-term sampling has the potential to provide information on aspects of the jet behavior other than component speeds. For example, relatively slow changes in the jet envelope or direction could be observed, providing information about jet propagation and the external medium. As described in Section 2, we have, somewhat fortuitously, roughly annual observations covering 17 yr. Prior to our pilot project, a few archival observations done for other reasons are available. Between 2009 and 2016, annual observations were made as part of an effort to observe radio counterparts

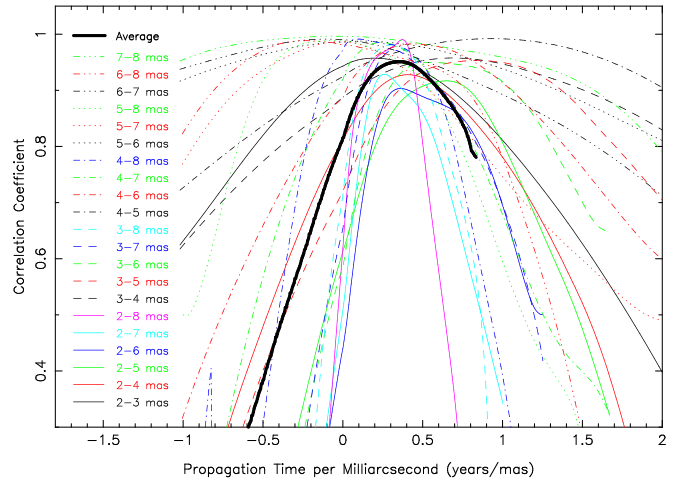


Figure 21. Correlation functions used to determine the propagation speed of the side-to-side variations in the M87 jet center position. These provide an alternate determination to that from the least-squares fit shown in Figure 20. The data used are the subset of those shown in Figure 20 that were taken between 2006 and 2016. Data for each core distance, measured at 1 mas intervals in core distance, were correlated with that of each other distance as a function of time lag. The time axis is scaled by dividing by the separation in core distance of the pair so that the axis becomes the propagation time per mas (years mas^{-1}). The correlation function for each pair of core distances is identified by a unique combination of color and line type as shown in the legend. For most pairs, the line type indicates the initial core distance of each pair, while the color indicates the separation in core distance of the pair. The 7–8 mas pair does not conform to the pattern because the plotting software used provided too few line types. The average over all the correlation curves is shown by the bold black line. The weighted average of the peaks of the individual curves is $0.327 \pm 0.038 \text{ yr mas}^{-1}$, while the peak of the average curve is at $0.350 \text{ yr mas}^{-1}$.

to TeV flares. In this section, we first present the images from these roughly annual observations and subsequently determine displacement motions from these images. A clear finding is that the jet moves transversely on timescales of several years.

3.4.1. Intensity Images

The total intensity evolution of the subparsec-scale radio jet in M87, spanning a 17 yr period from 1999 to 2016, is shown in Figures 16–18. Approximately annual observations at 43 GHz involving the VLBA are shown. The images in Figures 16–18 were used to make the movie shown in the online animation of Figure 19.

Where multiple observations were made in less than a year, average images are shown. Image quality improves significantly with time as the VLBA hardware improved and as more average images became available. See Table 3 for details of the observations, including the bit rate and the off-source image noise.

The images in Figure 16 are early observations and have limited sensitivity. In some of the very early observations, the actual observing time was short because M87 was a phase calibrator, not the primary target of the archival observations shown here. Average images are available from the pilot project in 2006, from the main monitoring observations in 2007 and 2008, and from the trigger response in 2010.

Significant transverse displacement of the jet, especially between about 2 and 8 mas from the core, is seen in Figures 16–18, particularly in the epochs after 2011.1 relative to earlier epochs. Lines have been drawn on the figures that

follow the bright jet edges in the 2007.4 average image. These lines help make the northern shift of the jet clear, especially in the later epochs. The transverse displacements are discussed more extensively below.

Figures 16–18 also show that the relative brightness of southern and northern edges experiences significant changes over the 17 yr period in the innermost few mas. There are epochs when the northern side is brighter and epochs when the southern side is brighter. Which is brighter can be different as a function of position along the jet. It does appear that, when there is a transverse shift, the side toward which the shift happens brightens in the innermost 2–3 mas. The best case is for the large shift to the north that started in 2011.1. For that epoch, the northern side is brighter by a factor of 2–3 near 2 mas. The northern side remains brighter as the shift propagates along the jet, but as the jet starts to return toward its original position, the southern side becomes brighter.

3.4.2. Displacement Motion

The results of an effort to measure the propagation speed of the jet offset are shown in Figures 20 and 21. The transverse offset of the measured center of the jet relative to a nominal jet center line, which extends at position angle -72° from the core, is shown in Figure 20 for core distances at 2–8 mas at 1 mas increments (the offset is actually in the y direction in the rotated images). The offsets show a general drift north superimposed on what appears as a quasi-sinusoidal variation. The patterns for each distance from the core show a lag, indicating a propagation speed that is addressed in this section. For core distances at and beyond 3 mas, the offsets were measured from images that had been blurred along the jet direction (convolved with a beam of 0.42×1.0 mas elongated along $PA = -72^\circ$) to reduce effects of fine-scale structure. At 2 mas, the full-resolution images were used. Slices perpendicular to the jet were made at the core distances noted.

The offsets of the jet center from the $PA = -72^\circ$ line were determined from the slices by the following algorithm. First, the peak intensity south of the $PA = -72^\circ$ line was determined. Then, the locations of the most southern interpolated points at one-quarter and one-half of the that peak intensity were found. The average of those two points was treated as the position of the southern side, and one-half of the difference was treated as an “error bar.” The process was repeated for the northern side using the most northern points at one-quarter and one-half of the peak value north of the $PA = -72^\circ$ line. The separate determinations of the north and south peaks prevent spurious results when one ridge is significantly brighter than the other—a frequent case. The center was taken to be the average position of the northern and southern side points, and the number used for weighting in the analysis was the quadratic sum of the “error bars.” In practice, these “error bars” did not vary much between points, and, to avoid clutter, only those for the 2 and 8 mas points are shown in Figure 20.

Two methods were used to determine a speed of propagation of the transverse displacement pattern. The first method is a least-squares fit for the parameters of a simple equation that roughly describes the data in Figure 20. The purely empirical equation is not based on any particular physical model and is

given by

$$\begin{aligned} t &= t_{\text{yr}} - 2000.0 \\ t_d &= t - z/v_p \\ R_c &= R_0 + a_1 z + a_2 t_d + a_3 z^{a_4} \sin(2\pi f t_d + \phi_0) \end{aligned} \quad (1)$$

where R_c is the offset from the nominal center line in mas, t_{yr} is the date in decimal years, t is the number of years since 2000.0 (to reduce the chances of numerical problems), and t_d is the time a feature seen at time t at core distance z was at the core assuming linear motion from the core at speed v_p . The form of t_d used to parameterize the equation is not meant to imply that linear pattern motion occurs or exists very close to the core. The fitted parameter results for v_p , R_0 , a_1 , a_2 , a_3 , a_4 , f , and ϕ_0 are given in Table 1. The offset, R_c , for each core distance given by Equation (1) is shown as dashed lines in Figure 20 with the colors matching the data colors. The bottom panel shows the residuals after subtracting the model from the data.

A linear change in offset with core distance at a fixed time can be created in at least two ways. First, an error in the choice of the position angle assumed for the jet center relative to the core would produce such an effect because the resulting linear offset would grow with core distance. Second, if the offset changes with time at a constant rate, and that change propagates down the jet at finite speed, the same linear change in offset with distance will be produced. Both effects are included as terms in Equation (1). This would not normally work for the fit because the terms are completely correlated. However, we assume that the pattern propagation speeds for the linear change in the jet center offset and for the sine wave are the same. This causes the pattern propagation speed to be controlled by the sine wave, leaving the error in the choice of jet position angle to absorb any additional linear change in offset with distance. This assumption decorrelates the terms. The fitted result that the linear change with distance (a_1) is very small suggests that the assumed position angle was properly chosen for the reference epoch (2000.0).

This first method gives a period result of 10.3 ± 0.3 yr within the errors. However, visual inspection of Figure 20, concentrating on the 2 and 3 mas data points, suggests a shorter period. These two distances are the only ones measured from images before 2006 and have an extra 7 yr time baseline. Indeed, a fit to just the 2 and 3 mas data gives a period result of 7.6 ± 0.3 yr. Nevertheless, adding the data from farther down the jet strongly discourages the shorter period. The differences seem to result from the 2006 and 2016 data—the extremes of the time range for the more distant data. As a check of the 2016 March 14 data, and an indication of the reliability of the rest of the data, a 2016 April 10 epoch (the result of a high-energy trigger and included at the end of Table 3), not shown in Figure 18, was included for the fit. The results using this 2016 April 10 epoch show good agreement with those ending with the 2016 March 14 epoch. A few more years of good data, covering more than a full period, should provide some clarification. In any event, this method gives an apparent pattern speed of 3.36 ± 0.68 mas yr $^{-1}$ for $\beta_p^{\text{app}} = 0.89 \pm 0.18$. At a viewing angle $\theta = 17^\circ$ the apparent pattern speed would imply an intrinsic pattern speed of $\beta_p \approx 0.78 \pm 0.04$.

In the second method used to measure the displacement pattern speed, for each core distance, the measured data points at the different epochs were linearly interpolated to a dense time series, and each pair of time series (different distances) was

Table 1
Fitted Parameters of the Jet Displacement Model

Parameter	Description	Fit Value	Std. Error	Units
R_0	Offset at $z_{\text{ob}} = 0$, $t_d = 0$	-0.196	0.024	mas
a_1	Slope with distance	0.005	0.004	mas offset per mas core distance
a_2	Linear change with time	0.022	0.002	mas yr ⁻¹
v_p	Angular pattern speed	3.36 ^a	0.68	mas yr ⁻¹
a_3	Sine wave amplitude at $z = 0$	0.061	0.017	mas
a_4	Index of sine wave amp dependence on z_{ob}	0.69	0.16	...
f	Sine wave frequency	0.097 ^b	0.003	cycles mas ⁻¹
ϕ_0	Phase at $t_d = 0$	31	15	deg

Notes.

^a For the assumed distance of M87, the angular pattern speed (v_p) converts to an apparent pattern speed of $\beta_p^{\text{app}} = 0.89 \pm 0.18$.

^b The period of the sine wave (inverse of the frequency) is 10.3 ± 0.3 yr.

cross-correlated. This was done by calculating the ‘‘Pearson’s r ’’ statistic for time lags between -5 and 5 yr. The normalization is done separately for each lag to try to minimize the impact of end effects since the maximum lags are a noticeable fraction of the overall range. The correlations should peak at a time lag related to the pattern propagation speed. This method of measuring the propagation speed does not assume any particular functional form for the offsets, so it is insensitive to the timescale of any oscillations. The correlation functions are plotted in Figure 21. The correlations are plotted against time lag divided by the core-distance separation of the two time series being correlated. This turns the time lag axis into units of propagation time per mas, which is an inverse speed. The actual speed is not a natural unit for plotting the correlation functions because there is an infinity and sign flip in speed at zero lag. The correlations were then averaged as a function of the inverse speed, with the result shown by the bold black line in Figure 21. The peak of the average curve is at $0.350 \text{ yr mas}^{-1}$, which is 2.86 mas yr^{-1} or $\beta_p^{\text{app}} = 0.75$. An average speed was also calculated by measuring the peaks of each correlation function, again scaled by the distance, and performing a weighted mean. For the weights, the widths to the 90% amplitude points were used. That gives reasonable relative weights and does not significantly affect the calculated standard error, which takes into account the scatter of the points. The result, determined in this manner, is $0.327 \pm 0.038 \text{ yr mas}^{-1}$, which is $3.1 \pm 0.4 \text{ mas yr}^{-1}$ or $\beta_p^{\text{app}} = 0.81 \pm 0.10$. At a viewing angle $\theta = 17^\circ$ the apparent pattern speed (weighted average) would imply an intrinsic pattern speed of $\beta_p = 0.76 \pm 0.025$.

The speed measured from the correlation analysis ($\beta_p^{\text{app}} = 0.81 \pm 0.10$) is slower than, but within the errors of, the speed measured with the least-squares fitting ($\beta_p^{\text{app}} = 0.89 \pm 0.18$). This match between the speeds from the two methods lends credence to the results. In either case, the speed is significantly less than the component speeds measured in the component motion analysis ($\beta_p^{\text{app}} > 2$ for the fast components). Thus, the transverse shift of the jet is not propagating down the jet ballistically. Another indication that the offset is not ballistic is that it does not grow linearly with distance. The amplitude deviation of the fitted sine wave from the nominal axis grows with distance by only a power-law index of $\sim 2/3$.

3.5. The Counterjet

Essentially all of the images presented in this paper show evidence for a counterjet. A counterjet can provide important clues to the nature of the jet. First, its mere existence shows that

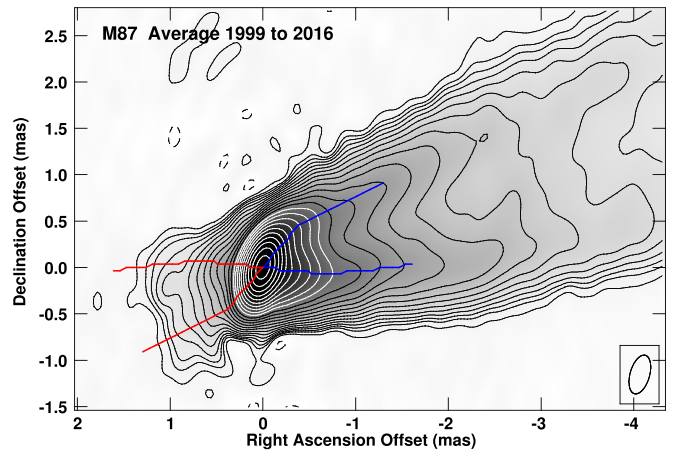


Figure 22. Noise-weighted average image made from the first 49 epochs of the 50 epochs listed in Table 3. The image shows the average counterjet structure at 43 GHz as far from the core as is allowed by our data. The convolving beam was the usual 0.43×0.21 mas, elongated along position angle -16° . The contour levels, in mJy beam^{-1} , are $-0.2, 0.2, 0.4, 5.6, 8, 11.3, 16$, increasing from there by factors of $\sqrt{2}$. The peak is $726 \text{ mJy beam}^{-1}$, and the off-source rms noise level is $47 \mu\text{Jy beam}^{-1}$. Blue lines (jet side) and red lines (counterjet side) show the locations where intensity measurements were made to give the sidedness data shown in Figure 25. The lines on the jet side follow the ridges, while those on the counterjet side are the jet-side lines reflected through the core.

the M87 jet is two-sided as it is launched, which is commonly assumed but rarely proven in superluminal sources. This provides evidence against flip-flop models (e.g., Rudnick & Edgar 1984) where the jet is one-sided at any given time. Second, the ratio of brightness of the jet and counterjet, if it is assumed to be the result of Doppler boosting, gives a measure of the jet speed. Third, similarities or differences in the structure of the jet and counterjet help distinguish features related to fundamental dynamical structures in the jet and surrounding medium from more ephemeral, time-dependent structures based on details of the stability of the jet generation mechanism.

While all of our images show the counterjet, those based on data that predate the recent upgrades to the VLBA did not reliably delineate the structure of the counterjet. The counterjet feature is weak and located in the region near the bright core where artifacts from residual calibration errors are most pronounced. Stacked images showed that it has a structure roughly symmetric with the main jet, and some of the recent, high-sensitivity observations show the structure more clearly. Here we first push the sensitivity at the normal resolution as far as possible with our data by stacking all of the images, with

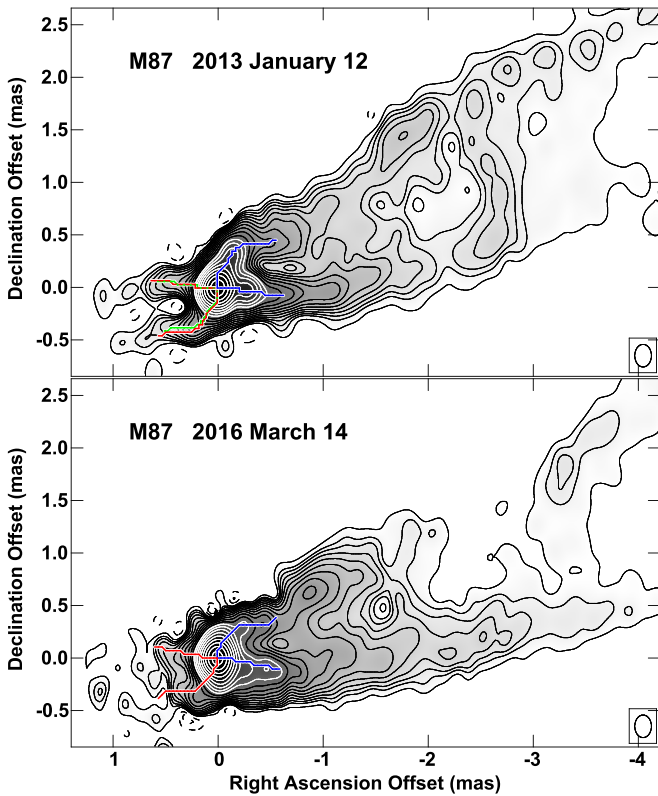


Figure 23. Mild super-resolution 2013 and 2016 images using the wide-bandwidth system on the VLBA. The convolving beam of 0.21×0.16 mas, elongated north–south, is shown in the lower right corner. It is $\sim 70\%$ the size of the fitted beam in the north–south direction and $\sim 100\%$ in the east–west direction. The contour levels, in mJy beam^{-1} , are $-2.8, -2, -1, 1, 2, 2.8$ and increase from there by factors of $\sqrt{2}$. Jagged blue (jet side) and red (counterjet side) lines connect pixel center points where intensity measurements were made for the sidedness data used in Figure 25. Green lines on the counterjet side in the 2013 image connect counterjet points plotted at 90% of the core distance of corresponding jet side points. Those green lines are dotted where they overlap the red lines. Note the symmetry between the jet and counterjet, especially in 2013. At very low levels there are residual calibration artifacts near the core, particularly in the 2016 image.

weighting based on the off-source noise. Subsequently, we explore the structure close to the core by adjusting imaging parameters to emphasize resolution in the creation of images from two of the best high-sensitivity epochs.

An image based on stacking 49 images from the epochs listed in Appendix B (excluding the last epoch) is shown in Figure 22. Only the inner few mas are shown to emphasize the counterjet because the side-to-side variations discussed in Section 3.4 blur the otherwise sharp-edged structure on larger scales. On these small scales, the side-to-side variation-induced blurring is relatively small compared to the resolution. This image allows measurement of the sidedness intensity ratio to ~ 1.7 mas from the core, provides cross-jet resolution, and shows the edge brightening similar to that seen on the jet side. The blue (jet side) and red (counterjet side) lines crossing the core in Figure 22 show the locations of the pixels whose intensities are used to measure the sidedness that will be discussed in Section 4.2.2. These pixels are chosen to follow the north and south ridges on the jet side. On the counterjet side, each pixel chosen is simply at the symmetrically opposite position from the corresponding pixel on the jet side. This builds in an assumption that the jet/counterjet structure is symmetric, which the image shows is close to, but not

precisely, true. Recall that, as with any stack spanning times longer than the timescales for changes in the source, the detailed changing structure is smoothed out, leaving the persistent structure.

Our recent higher-sensitivity, wide-bandwidth observations have provided an opportunity to delineate the structure of the counterjet at individual epochs in more detail than was previously possible. To examine the counterjet structure close to the core with two of the best data sets, 2013 January 12 and 2016 March 16, we have used imaging parameters that lead to higher resolution than our other images at the cost of degraded image quality on larger scales. This was accomplished by using a “robustness” (Briggs 1995) approximating uniform weighting. Uniform weighting emphasizes the long baselines even though they are a relatively small fraction of the data. Then the point-source CLEAN components were convolved with a beam smaller than that fitted to the dirty beam. This “super-resolution” increases the noise level and can be risky if overdone. Here the fitted beams were 0.31×0.16 mas elongated in $\text{PA} = -5^\circ.3$ in 2013 and 0.30×0.17 mas elongated in $\text{PA} = -6^\circ.2$ in 2016. The final convolving beam used was 0.21×0.16 mas in $\text{PA} = 0^\circ$. Thus, the super-resolution reduced the beam area by about 50%, mostly in the north–south direction. The peak flux densities are 0.62 and $0.48 \text{ Jy beam}^{-1}$ in 2013 and 2016, respectively.

The resulting fairly mild super-resolution images of the inner jet from the two data sets are shown in Figure 23. The images show a structure in which the counterjet is a reflection of the main jet, but at lower intensity. The bright edges of the main jet that exit the core at an apparent opening angle of about 70° have corresponding bright edges on the counterjet side. As with the stacked image, the blue lines (jet side) and red lines (counterjet side) show the locations where measurements of intensity along the jet were made for the sidedness data discussed in Section 4.2.2. The blue and red lines follow the jet ridgeline on the jet side and are reflected across the core for the counterjet side. They are jagged because measurements were made at pixel centers.

The northwest jet edge and the southeast counterjet edge, especially on 2013 January 12, show a distinct, sharp bend in both jet and counterjet at about 0.44 mas from the core. Such a feature is not common in our other images, so its appearance in both jet and counterjet suggests a common origin. If the bend were moving outward at a significant fraction of the speed of light, one would expect to see the bend closer to the core on the counterjet side because of differential light-travel time. That allows limits to be placed on the propagation speed of the bend. The green lines in the top panel of Figure 23 (2013 January 12 epoch) show a $\sim 10\%$ core-distance reduction compared to the red lines (which are symmetric with the blue lines on the jet side). This small reduction does appear to be a somewhat better match to the counterjet ridgeline. A 10% difference requires that the speed associated with bend motion be no more than about $0.05c$. This inner jet and counterjet region is where the slowest-moving components are seen (see Figures 13 and 14). On the other hand, there is a significant sidedness intensity ratio in this region (see Section 4.2.2), which suggests higher material speeds. Thus, we conclude that material is moving through the bend.

The results of the sidedness measurements and their implications are discussed in Section 4.2.2.

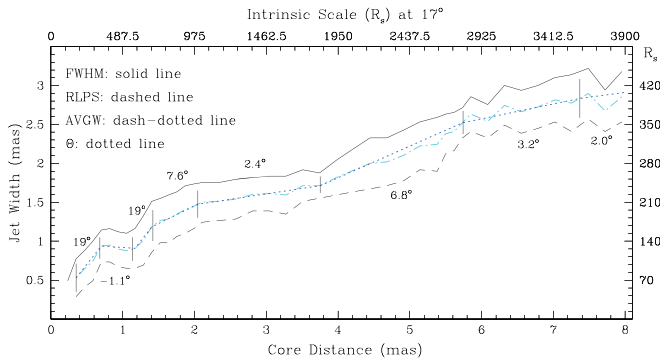


Figure 24. Average (AVGW) of FWHM- and RLPS-determined widths (cyan dot-dashed line), along with linear fits to the intrinsic opening angle, Θ (blue dotted line), between the vertical lines from the 23-epoch image. First and third vertical lines are shifted by -0.05 and $+0.1$ mas, respectively, relative to the locations indicated in Figure 6 in order to better accommodate the linear fitting. Numerical labels show the intrinsic full opening angle associated with the linear fits between the vertical lines. Beyond 7.4 mas the dotted line and label indicate the intrinsic opening angle of the kiloparsec-scale jet (see Section 1). The width along the right axis and the intrinsic core distance along the upper axis for the jet oriented at 17° to the line of sight are given in units of R_S .

4. Flow Dynamics and Emission

In this section, we explore what can be learned about the flow within the jet and about the structure of the jet based on the observational results of Section 3.

Section 4.1 examines the regions of expansion and recollimation of the jet envelope in the inner 7 mas of the jet, shown previously in Section 3.1 based on the 23-epoch average. Here we provide intrinsic opening angle values based on those data, on the 49-epoch average image data of Section 3.1, and on the images presented to study the counterjet in Section 3.5. This information can be used to provide an indication of the interaction between the jet and the external medium. It is distinct from Section 4.3, which is concerned with the internal flow structure of the jet.

Section 4.2 addresses the implications of the proper-motion measurements and of the ratio of the intensities of the jet and counterjet for jet flow speed and acceleration. Additionally, the different proper motions and intensities along the north and south sides of the jet and counterjet are used to explore poloidal versus helical flow models.

Section 4.3 addresses implications for the internal jet spine/sheath structure from the observed slice profiles and discusses potential differential Doppler boosting effects resulting from helical flow. These issues are distinct from Section 4.1, which addresses the jet envelope.

Section 4.4 explores the implications of propagation down the jet of the long-term changes in jet transverse position. Here we explore the constraints placed on the jet-external medium interface that would lead to the observed propagation assuming that nonballistic propagation can be described by the Kelvin-Helmholtz helical mode.

4.1. Expansion and Recollimation

Here the shape of the jet, especially regions of expansion and recollimation, is explored. That shape can provide constraints on the interaction of the jet and the external medium. In Figure 24 we redisplay the FWHM and RLPS widths from Figure 6, which are based on the 23-image stack of 2007 and 2008 data, and average the two to give a more reliable indicator

of the behavior of the jet width as a function of the intrinsic distance in units of R_S . As implied in the earlier discussion of Figure 6, there are sufficient uncertainties in the separate width measurements, especially in the region of greatest differences between about 5 and 6 mas, that we will not attempt to interpret those differences in terms of jet physics. Linear fits to the average width, indicated by the dotted line, are made between the vertical lines, which are shifted up to ~ 0.1 mas relative to the locations indicated in Figure 6 in order to better accommodate the linear fitting. The resulting intrinsic full opening angle associated with the linear fits is defined as $\Theta \equiv \arctan[\sin \theta (\Delta W / \Delta z)]$, where the viewing angle $\theta = 17^\circ$ and ΔW and Δz are the change in apparent width and apparent distance, respectively. Beyond 7.4 mas the dotted line in Figure 24 indicates the $\sim 2^\circ$ intrinsic opening angle of the jet beyond HST-1 from Owen et al. (1989). Our results suggest three collimation regimes: (1) an initial rapid expansion out to $\sim 340R_S$ (~ 0.7 mas) followed by jet contraction over a distance $\sim 195R_S$ (~ 0.4 mas), (2) a second equally rapid expansion beginning at $\sim 535R_S$ (~ 1.1 mas) with recollimation occurring over a distance $\sim 1265R_S$ (~ 2.6 mas), and (3) a third slower expansion beginning at $\sim 1805R_S$ (~ 3.7 mas) with recollimation still occurring at $\sim 3605R_S$ (~ 7.4 mas), where intrinsic distances in R_S assume a viewing angle of $\theta = 17^\circ$. On average our expansion is consistent with the parabolic structure out to about HST-1 found by Asada & Nakamura (2012). Our results confirm the initial rapid parabolic expansion found by Hada et al. (2013) inside $\sim 300R_S$. Our results also show that the structure consists of a subsequent contraction followed by additional expansions and recollimations beyond $\sim 535R_S$ that is more complicated than the slower single parabolic expansion beyond a few hundred R_S found in Hada et al. (2013).

The 49-epoch image (Figure 22), which shows the jet and counterjet and is based on 17 yr of data, also reveals different opening angle regimes for the jet. Motions blur the structure in the 49-epoch image, but the image still reveals a high initial opening angle near the core, followed by a narrower opening angle indicating slower expansion with distance. If we use the blue lines to determine the opening angle, we find $\Theta^{\text{app}} \approx 55^\circ$ inside 0.620 mas and $\Theta^{\text{app}} \approx 20^\circ$ beyond 0.620 mas and out to ~ 1.5 mas. The corresponding intrinsic opening angles are $\Theta \approx 23^\circ$ and $\Theta \approx 6^\circ$, respectively.

The mild super-resolution single-epoch 2013 and 2016 images (Figure 23) that show the inner jet and counterjet structures provide a more detailed view of the inner structure not blurred by motions. Now it is possible to see a rapid initial expansion, followed by a slower expansion in both jet and counterjet. In the 2013 image the blue lines indicate $\Theta^{\text{app}} \approx 58^\circ$ inside 0.5 mas and $\Theta^{\text{app}} \approx 10^\circ$ between ~ 0.5 and ~ 0.6 mas. In fact, the initial opening angle inside 0.5 mas must be even larger: we find an initial opening angle of $\Theta^{\text{app}} \approx 65^\circ$ if we connect the location of the sharp bend in the lines along the south counterjet and north jet to the core position. The corresponding intrinsic opening angles are $\Theta \geq 25^\circ$ inside 0.5 mas and $\Theta \approx 3^\circ$ between ~ 0.5 and ~ 0.6 mas. In the 2016 image the blue lines indicate $\Theta^{\text{app}} \approx 56^\circ$ inside 0.4 mas and $\Theta^{\text{app}} \approx 12^\circ$ between ~ 0.4 and ~ 0.6 mas. Again, if we connect the core position to the sharp bend in the south counterjet and north jet, we find an initial opening angle of $\Theta^{\text{app}} \approx 68^\circ$. The corresponding intrinsic opening angles are $\Theta \geq 23^\circ$ inside 0.4 mas and $\Theta \approx 3^\circ$ between ~ 0.4 and ~ 0.6 mas.

At even smaller scales than we resolve, Hada et al. (2016), using data at 86 GHz, find a region of jet expansion with apparent opening angle of $\Theta^{\text{app}} \approx 100^\circ$ inside 0.2 mas. They also find a subsequent contraction at a core distance of about ~ 0.25 mas. At a viewing angle of $\theta = 17^\circ$, the corresponding intrinsic opening angle is $\Theta \approx 38^\circ$ inside 0.2 mas.

The multiple expansion and collimation regions indicate a jet-launching region in which equilibrium parabolic expansion is achieved only after 5–7 mas, i.e., several thousand R_S . The nonequilibrium behavior found here and at smaller scales by Hada et al. (2016) should provide important information for the theoretical/numerical modeling of the jet-launching region. For example, we may be seeing the interaction between a black-hole-launched jet spine, velocity shearing sheath region, and disk wind cocooning medium (see also Hada et al. 2016), as well as the extent of the jet-launching and acceleration region. We note that the initial intrinsic opening angle near the jet base is such that a portion of the jet flow comes directly into the line of sight at a viewing angle of $\theta = 17^\circ$ to the jet axis. That some jet flow can be directly into the line of sight near to the jet base has consequences for models of the location and mechanism responsible for the TeV and associated radio flaring observed from M87.

4.2. Jet Flow

We now turn to the flow dynamics of the jet as revealed by the component motion measurements and by the observed sidedness ratios described in Section 3.2. The component motions represent the material flow speed if their origin is some feature of the underlying flow, such as a density enhancement, that moves with the jet material. They can also be slower than the underlying material if they are a pattern speed, such as might occur with instabilities, shocks, or interactions with external influences of some sort. The components are unlikely to be faster than the material speed. The sidedness ratio is most likely the result of Doppler boosting and is a direct consequence of the material flow speed. A sidedness ratio higher than implied by the true material speed would require some asymmetry in the physical parameters of the jet/counterjet system. A sidedness ratio lower than expected for the faster material motions also requires some complexity to the jet, such as the presence of some slower material that is contributing some of the emission. In the presence of Doppler boosting, which is assumed when there are superluminal apparent motions or high sidedness ratios, there can also be beaming-induced brightness differences between similar regions with different flow angles. In this section, the speeds implied by the component motions and sidedness are explored. Differences in speed and brightness between the sides of the jet are interpreted in terms of the possible flow patterns such as a helical flow. This discussion complements the extensive proper-motion study along the jet using the WISE analysis technique that can be found in MLWH.

4.2.1. Proper-motion Implications

Apparent jet motions obtained from the wavelet analysis given in Tables 2 and 3 of MLWH indicate averages of $\langle \beta_{\text{edge}}^{\text{app}} \rangle = 0.48 \pm 0.06$ (north) and 0.21 ± 0.04 (south) between 0.5 and 1 mas. Assuming pure poloidal flow along the jet edges, this would indicate intrinsic speeds of $\beta_{\text{edge}} = 0.64 \pm 0.03$ (north) and 0.43 ± 0.05 (south) at a viewing angle of $\theta = 17^\circ$.

Between 1 and 4 mas there are two velocity components. The slower component has $\langle \beta_{\text{edge}}^{\text{app}} \rangle = 0.17 \pm 0.16$ (north) and 0.49 ± 0.24 (south). The faster component has $\langle \beta_{\text{edge}}^{\text{app}} \rangle = 2.41 \pm 0.05$ (north) and 2.20 ± 0.15 (south). Following the same viewing angle and flow assumptions, the lower-velocity component would indicate $\beta_{\text{edg}} = 0.37^{+0.17}_{-0.34}$ (north) and $0.64^{+0.10}_{-0.17}$ (south), and the higher-velocity component would indicate $\beta_{\text{edge}} = 0.928 \pm 0.002$ ($\gamma \approx 2.68$) (north) and 0.918 ± 0.008 ($\gamma \approx 2.52$) (south).

It is hard to understand the velocity differences between opposite jet edges found assuming a purely poloidal flow. On the other hand, different values along opposite jet edges can naturally result from flow rotation about the jet axis. With rotation, the flow on each edge will be at different angles to the line of sight. Faster apparent motions will be seen along the edge, where the flow is at an angle to the line of sight that comes closer to the angle at which apparent motions are maximized.

The critical angle at which apparent motions are maximized, $\theta_{\text{crit}} \equiv \cos^{-1} \beta$, for $\beta \leq 0.928$ is $\theta_{\text{crit}} \geq 22^\circ$. This angle is greater than the poloidal flow angle to the line of sight along the jet edges, which is slightly larger than the jet axis angle to the line of sight (see Equation (4)). Thus, the higher apparent speeds along the northern jet edge between 0.5 and 1 mas and the higher apparent speeds along the northern jet edge of the faster component between 1 and 4 mas would indicate clockwise flow rotation about the jet axis. Here the “clockwise” terminology for the sense of rotation is for an observer looking toward M87 along the jet (not counterjet) axis and thus remains the same for a jet and counterjet that share a common source of rotation. Such rotation places the northern edge flow closer to the critical angle. The higher apparent speeds along the southern edge of the jet for the slower component between 1 and 4 mas would indicate counter-clockwise flow rotation for that component.

If the faster-component motion along the northern edge is interpreted as resulting from clockwise rotation, then the speed of the implied clockwise helical flow can be given approximately by

$$\frac{\beta_{\text{N}}^{\text{app}}}{|\sin(\theta_{\text{edge}} + \Delta\phi_{\text{h}})| + \beta_{\text{N}}^{\text{app}} \cos(\theta_{\text{edge}} + \Delta\phi_{\text{h}})} \approx \beta_{\text{h}} \approx \frac{\beta_{\text{S}}^{\text{app}}}{|\sin(\theta_{\text{edge}} - \Delta\phi_{\text{h}})| + \beta_{\text{S}}^{\text{app}} \cos(\theta_{\text{edge}} - \Delta\phi_{\text{h}})}, \quad (2)$$

where $\beta_{\text{N}}^{\text{app}}$ and $\beta_{\text{S}}^{\text{app}}$ are the apparent north (N) and south (S) edge motions, respectively, and $\Delta\phi_{\text{h}}$ provides an estimate of the difference in flow angle relative to pure poloidal flow along the jet edges at line-of-sight angle θ_{edge} . Here $\Delta\phi_{\text{h}} > 0$ indicates clockwise flow rotation, and we have made the simplifying assumption that the flow angle to the line of sight can be expressed as $\theta_{\text{edge}} \pm \Delta\phi_{\text{h}}$. A little manipulation allows us to solve for $\Delta\phi_{\text{h}}$, which is found from

$$\tan \Delta\phi_{\text{h}} = \frac{(\beta_{\text{N}}^{\text{app}} - \beta_{\text{S}}^{\text{app}}) \sin \theta_{\text{edge}}}{(\beta_{\text{S}}^{\text{app}} + \beta_{\text{N}}^{\text{app}}) \cos \theta_{\text{edge}} - 2\beta_{\text{S}}^{\text{app}} \beta_{\text{N}}^{\text{app}} \sin \theta_{\text{edge}}}. \quad (3)$$

In Equations (2) and (3), θ_{edge} is the viewing angle to the jet edges and is related to the viewing angle to the jet axis by

$$\cos \theta_{\text{edge}} = \frac{\cos \theta}{(\tan^2 \psi + 1)^{1/2}} \approx \left(1 - \frac{\psi^2}{2}\right) \cos \theta, \quad (4)$$

where $\theta = 17^\circ$ is the viewing angle to the jet axis and $\psi \equiv \Theta/2$ is the intrinsic half opening angle.

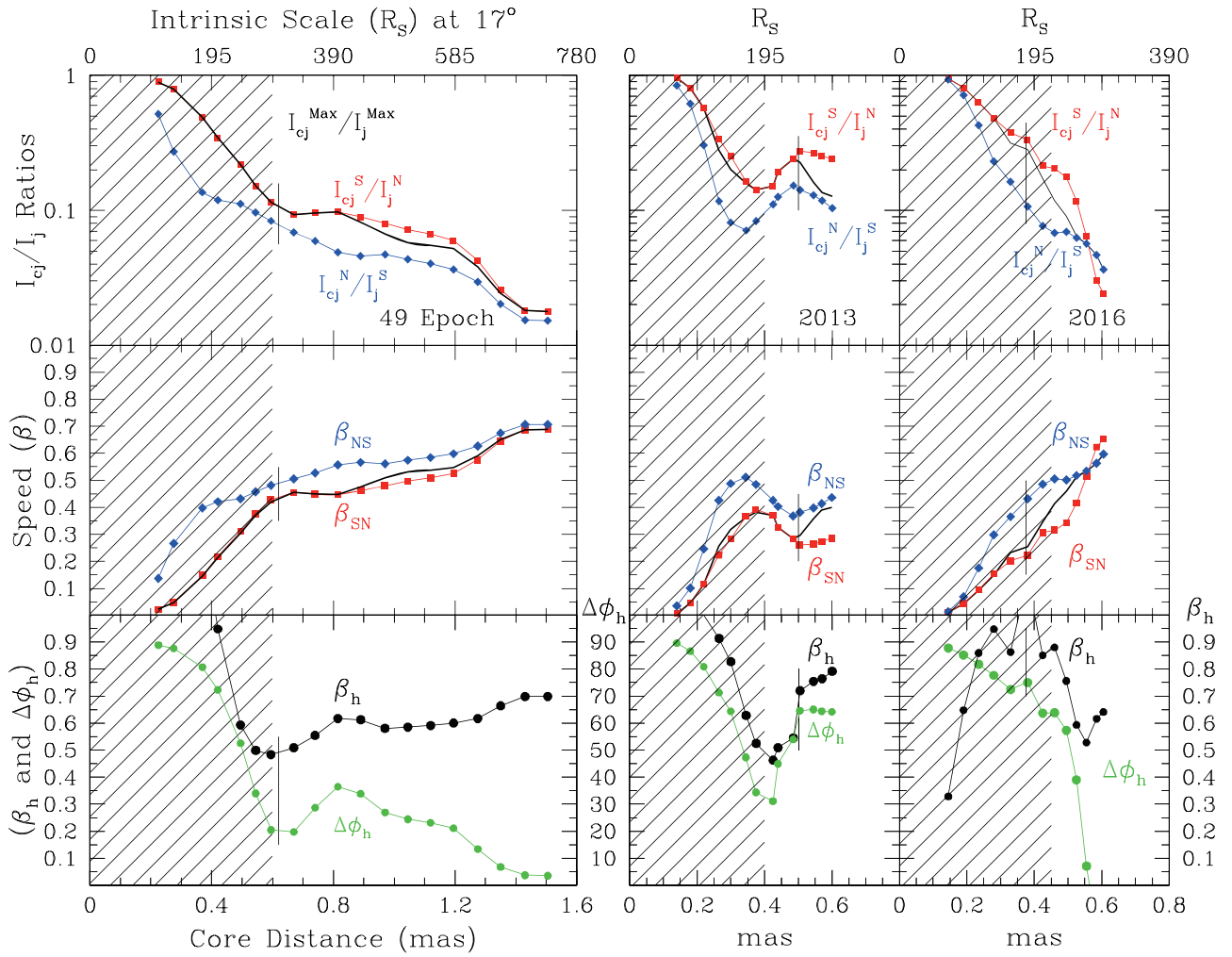


Figure 25. Top panels: counterjet/jet intensity ratios at image pixel positions along the blue and red lines in the M87 images of Figures 22 and 23. Each set is the ratio between intensities at positions on the counterjet (cj) side and the main jet (j) side that are symmetrically opposite the core. For comparison a black line indicates the intensity ratio choosing the maximum counterjet and jet edge intensities at each position. The positions were chosen to be along the northern (N) and southern (S) ridges on the jet side. The shaded region indicates where south counterjet and north jet ratios are dominated by the image resolution and core. The intrinsic scale in units of R_S along the jet is shown at the top. Middle panels: intrinsic jet speed implied by the ratios shown in the top panels at the viewing angle appropriate to the jet edges, θ_{edge} . An angle to the line of sight of the jet axis of $\theta = 17^\circ$ and a spectral index of $\alpha = 0.55$ are assumed. The vertical lines indicate the location where the jet opening angle changes significantly, seen mainly as a kink in the lines along the northern jet edge. Bottom panels: intrinsic flow speed, β_h , and flow angle, $\Delta\phi_h$, relative to pure poloidal motion along the jet edges.

Between 0.5 and 1 mas the intrinsic half opening angle ψ declines from about 9.5° to about -0.5° (see Figure 24). Here we use an average of $\psi \approx 4.5^\circ$, so the viewing angle to the jet edges is $\theta_{edge} \approx 17.6^\circ$. Now using the apparent edge motions reported above from MLWH so that $\beta_N^{app} = 0.48 \pm 0.06$ and $\beta_S^{app} = 0.21 \pm 0.04$, we find that

$$\Delta\phi_h = 7.8 \pm 1.8 \text{ and } \beta_h = 0.56 \pm 0.03$$

provides an indication of intrinsic clockwise helical flow less than 1 mas from the core. The likely range of values was determined by offsetting β_N^{app} and β_S^{app} , separately, by plus and minus 1σ and then taking the geometric sum of the positive changes and of the negative changes. The results were sufficiently symmetric to use an average absolute offset as the quoted error.

Between 1 and 4 mas, ψ declines from $\sim 9.5^\circ$ to $\sim 1.2^\circ$ (see Figure 24) but is at the smaller angle over two-thirds of this range. Here we use a distance-weighted average of $\psi \approx 3^\circ$ so that the viewing angle to the jet edges is $\theta_{edge} \approx 17.3^\circ$. Now using the faster apparent component motions from MLWH so

that $\beta_N^{app} = 2.41 \pm 0.05$ and $\beta_S^{app} = 2.20 \pm 0.15$, we find that

$$\Delta\phi_h = 2.9 \pm 2.0 \text{ and } \beta_h = 0.924 \pm 0.003$$

provides an indication of intrinsic clockwise helical flow a few mas from the core. Thus, in a flow rotation scenario we find evidence for a clockwise helical flow accelerating from $\beta_h \approx 0.56$ inside 1 mas to $\beta_h \approx 0.92$ at larger distances, with the flow becoming more poloidal at larger distances.

For the lower-velocity components from MLWH, if the edge motions, $\beta_N^{app} = 0.17 \pm 0.16$ and $\beta_S^{app} = 0.49 \pm 0.24$, are interpreted as resulting from counterclockwise rotation, then the flow angle and speed of the implied counterclockwise helical flow beyond 1 mas are $\Delta\phi_h = -9^\circ \pm 8^\circ$ and $\beta_h = 0.55 \pm 0.12$, respectively. Here we note that angles closer to the poloidal case ($\Delta\phi_h = 0$) result in a smaller value for the speed β_h . Our results for the fast- and slow-component flow angles allow for poloidal flow of both components within less than 1.5 times the errors. Nevertheless, our results suggest the possibility of a complex velocity shearing region with opposite sense of rotation for the fast and slow components found by MLWH.

4.2.2. Jet/Counterjet Intensity Ratio Implications

The ratio of the intensities of the jet and counterjet provides information about the jet flow, under the assumption of an inherently symmetric system, which is independent of the component motions. The average image of M87 shown in Figure 22 and the super-resolution images of M87 shown in Figure 23 have been used to obtain intensity ratios between counterjet and jet edges that are symmetrically opposite the core. The resulting intensity ratios are shown in the top panels of Figure 25, where the data points are at image pixel positions along the blue and red lines shown in the images. The ratios, I_{cj}^S/I_j^N and I_{cj}^N/I_j^S , are between intensities at positions on the counterjet (cj) side and at positions on the main jet (j) side that are symmetrically opposite the core. The positions were chosen to be along the northern (N) and southern (S) ridges on the jet side. The structures on the counterjet side did not determine the positions, although the images show that the symmetry assumption is good but not exact. In Figure 25 the ratio $I_{cj}^{\text{Max}}/I_j^{\text{Max}}$, which is the intensity ratio choosing the maximum counterjet and jet edge intensities at each core distance independent of symmetry considerations, is included for comparison purposes. Recall that the intensity ratios are dominated by the beam until the jet and counterjet features are resolved from the core. Since the beam is elongated more along the inner south ridge on the counterjet side and north ridge on the jet side, these intensity ratios will remain high farther from the core, as is evident in all the intensity ratio panels. For example, the 49-epoch I_{cj}^N/I_j^S ratio stops its steep core-dominated decline at ~ 0.4 mas, whereas the I_{cj}^S/I_j^N ratio stops its steep core-dominated decline at ~ 0.6 mas, and the 2013 I_{cj}^N/I_j^S ratio stops its steep core-dominated decline at ~ 0.3 mas, whereas the I_{cj}^S/I_j^N ratio stops its steep core-dominated decline at ~ 0.4 mas. Also the 2016 I_{cj}^N/I_j^S and I_{cj}^S/I_j^N ratios do not appear beyond core-dominated influence until ~ 0.45 mas. The region of core influence is shaded in the figure panels. Beyond the region of core influence, the fact that the regions sampled are symmetric about the core, as is the beam, should ensure that the ratios are not significantly sensitive to the beam shape.

The persistence of larger ratios between the south counterjet and north jet edges, I_{cj}^S/I_j^N , than between the north counterjet and south jet edges, I_{cj}^N/I_j^S , can be interpreted in terms of Doppler boosting and suggests that the northern side of the counterjet and jet is deboosted relative to the south side of the counterjet and jet. In Figure 25 the middle panels show the computed values of a purely poloidal speed along the north counterjet edge and south jet edge, β_{NS} , and along the south counterjet edge and north jet edge, β_{SN} , required by the intensity ratios. Speeds are computed from

$$\beta \cos \theta_{\text{edge}} = \left(\frac{1 - (I_{cj}/I_j)^{1/(2+\alpha)}}{1 + (I_{cj}/I_j)^{1/(2+\alpha)}} \right), \quad (5)$$

where, as previously stated, $\cos \theta_{\text{edge}} \simeq (1 - \psi^2/2)\cos \theta$. Values are computed using the viewing angle to the jet axis $\theta = 17^\circ$, the intrinsic half opening angle $\psi \equiv \Theta/2$, and the spectral index $\alpha = 0.55$ ($I \propto \nu^{-\alpha}$; α appropriate to the kiloparsec-scale jet in the radio band; Frazer Owen, private communication). In the panels the vertical line indicates the location where the opening angle changes. For all computations, the intrinsic opening angles for the average 49-epoch image are assumed to be $\Theta = 23^\circ$ inside 0.620 mas and $\Theta = 6^\circ$ beyond 0.620 mas. The intrinsic opening angles for the

2013 and 2016 images are assumed to be (for 2013) $\Theta = 25^\circ$ inside 0.5 mas and $\Theta = 3^\circ$ beyond 0.5 mas and (for 2016) $\Theta = 23^\circ$ inside 0.4 mas and $\Theta = 3.6^\circ$ beyond 0.4 mas.

For an assumed purely poloidal flow, the intensity ratios associated with the 49-epoch intensity image require a higher speed along the north counterjet and south jet edges and lower speed along the south counterjet and north jet edges. These relative speeds are not consistent with the faster motions along the north side of the jet and slower motions along the south side of the jet found from component motions by MLWH. A resolution to this inconsistency for poloidal flow will be suggested in the discussion of helical flows below. The trend of intensity ratios with core distance provides evidence for speed changes and, in particular, acceleration in resolved regions near the core. On average the flow implied by the intensity ratios increases from $\beta \approx 0.3$ to 0.5 between ~ 0.4 and ~ 0.7 mas ($\sim 195R_S$ to $\sim 341R_S$), then slowly increases to $\beta \approx 0.55$ at 1.2 mas ($\sim 585R_S$), and finally accelerates to $\beta \approx 0.7$ at ~ 1.4 mas ($\sim 682R_S$). At larger distance the counterjet intensity approaches the level of the noise and imaging artifacts, so the intensity ratios cannot be determined from our data. The counterjet/jet intensity ratio implies that the flow speed increases most rapidly in the regions of about 0.4–0.7 mas and about 1.2–1.4 mas, where the two rapid expansions of counterjet and jet occur (see Figure 24). Recall that the counterjet width behaves similarly to the jet width within the ~ 1.2 mas of the core where it can be seen.

The average purely poloidal flow behaviors inferred from the intensity ratios for the 2013 and 2016 super-resolution images are very different from each other. In part the differences may result from small separation from the core along with noise and imaging artifacts particularly in the 2016 image. Nevertheless, the 2016 image intensity ratios imply an intrinsic flow that on average rapidly accelerates from $\sim 0.25c$ at 0.3 mas to $\gtrsim 0.6c$ at ~ 0.6 mas, which exceeds the speed $\sim 0.5c$ found for the 49-epoch average image at ~ 0.6 mas. The better-quality 2013 image intensity ratios imply a much more complex behavior with an intrinsic flow that on average first increases from $\sim 0.4c$ at 0.3 mas to $\gtrsim 0.45c$ at ~ 0.35 mas and then decreases to $\sim 0.3c$ at 0.5 mas, where the opening angle changes from rapid to a slower expansion. At larger distance the flow accelerates back to $\sim 0.4c$ at 0.6 mas. Notice that typical speeds from the 2013, 2014, and 49-epoch images at 0.5 mas are in the range of $0.4c$ – $0.6c$.

We can compare typical poloidal flow speed values inferred from the counterjet/jet intensity ratios with the proper motions associated with bright features within the jet shown in Figures 13 and 14 and the apparent motions from the wavelet analysis reported by MLWH. The proper motions shown in Figures 13 and 14 indicate $\beta^{\text{app}} \lesssim 0.5$ at core distances < 0.5 mas with motions up to $\beta^{\text{app}} \lesssim 2.2$ at core distances > 1 mas (somewhat less on the north side). Figure 20 in MLWH also shows clearly that the velocities of the fastest 10% of features increase from less than $0.5c$ at ~ 0.5 mas to over $2c$ beyond ~ 2 mas. Thus, tracking individual components and the wavelet analysis indicate acceleration in the same region indicated by the counterjet/jet intensity ratios. In particular, at a viewing angle of $\theta = 17^\circ$ the wavelet analysis indicates acceleration along the jet edges from $\langle \beta_{\text{edge}} \rangle \approx 0.5$ at < 0.5 mas to $\langle \beta_{\text{edge}} \rangle \approx 0.92$ at > 1 mas from the core. Thus, for an assumed purely poloidal flow the intensity ratios provide qualitative but not quantitative agreement with the speeds and acceleration found by the component tracking and by the wavelet analysis.

In Section 4.2.1 we found that faster northern edge motions along the jet can be associated with helical flow. We examine the intensity ratio implications for helical flow in the bottom panels of Figure 25. Here we compute the difference in flow angle, $\Delta\phi_h$, relative to pure poloidal motion along the jet edges, and the flow speed, β_h , required to produce the observed counterjet/jet intensity ratios, where again we have made the simplifying assumption that the flow angle to the line of sight can be expressed as $\theta_{\text{edge}} \pm \Delta\phi_h$. In these panels the flow speed is computed from

$$\frac{(1 - R_{\text{NS}})}{\cos(\theta_{\text{edge}} - \Delta\phi_h) + R_{\text{NS}} \cos(\theta_{\text{edge}} + \Delta\phi_h)} \approx \beta_h$$

$$\approx \frac{(1 - R_{\text{SN}})}{\cos(\theta_{\text{edge}} + \Delta\phi_h) + R_{\text{SN}} \cos(\theta_{\text{edge}} - \Delta\phi_h)}, \quad (6)$$

where

$$R_{\text{NS}} \equiv (I_{\text{c}_j}^{\text{N}}/I_{\text{j}}^{\text{S}})^{1/(2+\alpha)} \text{ and } R_{\text{SN}} \equiv (I_{\text{c}_j}^{\text{S}}/I_{\text{j}}^{\text{N}})^{1/(2+\alpha)}.$$

A little manipulation allows us to solve for $\Delta\phi_h$, which is found from

$$\tan \Delta\phi_h = \frac{(R_{\text{SN}} - R_{\text{NS}})}{(1 - R_{\text{SN}})(1 - R_{\text{NS}})} \cot \theta_{\text{edge}}, \quad (7)$$

and as previously, $\Delta\phi_h > 0$ indicates clockwise helical flow. Our helical flow analysis here depends on both north and south edge counterjet and jet intensity ratios and thus can only be applied if both edge ratios are beyond the region of core influence as shown by the shaded region in Figure 25. These equations look very similar to Equations (2) and (3) but are in terms of intensity ratios rather than component speeds.

The assumption of helical flow solves the edge flow issues associated with the intensity ratios raised by the assumption of purely poloidal flow. Now flow will appear faster on the northern jet edge and slower on the southern jet edge as observed. The helical flow speeds and acceleration associated with the 49-epoch image intensity ratios are comparable to the values indicated by the component tracking and by the wavelet analysis inside 1 mas, i.e., acceleration from $\beta_h \approx 0.475$ to $\beta_h \gtrsim 0.625$ between 0.6 and 0.8 mas, albeit with values of $\Delta\phi_h \approx 20^\circ\text{--}35^\circ$, considerably larger than suggested by our estimate of $\Delta\phi_h \approx 7^\circ.8$ based on average edge motions inside 1 mas. Inside 1 mas the 49-epoch image intensity ratios probe the counterjet and jet region where the first rapid expansion ceases and the jet recollimates.

Speeds and acceleration from component tracking and the wavelet analysis exceed the values suggested by the 49-epoch image counterjet/jet intensity ratios at core distances beyond 1 mas, although by 1.4 mas $\Delta\phi_h$ has decreased to a value of about 2.9 that is comparable to our estimate based on average edge motion between 1 and 4 mas. A possible explanation for slower motion based on intensity ratios beyond 1 mas is the slow components detected in the wavelet analysis. Those components would not be subject to strong beaming, so adding the emission from them and from the fast components would mimic an intermediate speed, which is what is seen. Recall that the intensity ratio is set by the material flow speed, in contrast to component speeds that can be set by patterns moving at different speeds from the material. While it is possible for a pattern to move faster than the material speed, e.g., flow plus sound or Alfvén speed, it is unlikely that pattern effects can

explain why the counterjet is brighter than would be expected for the observed component speeds.

At very small angular scales the super-resolution image intensity ratios probe the first rapid counterjet and jet expansion region. The better-quality 2013 intensity ratios would indicate a helical flow that accelerates from $\beta_h \approx 0.5$ to $\beta_h \approx 0.8$ between 0.4 and 0.6 mas in the initial rapid counterjet and jet expansion region that extends to ~ 0.7 mas (see Figure 24). This provides our only evidence for rapid acceleration associated with rapid counterjet and jet expansion and toward flow values consistent with the faster-component motions found by the WISE analysis between 1 and 4 mas. The poorer-quality 2016 intensity ratios could be taken to indicate the creation of a slower-moving counterclockwise helical flow, i.e., $\Delta\phi_h < 0$, beyond 0.55 mas, consistent with the slower-moving component motions found by the WISE analysis between 1 and 4 mas. In any event, it is clear that at these small angular scales the situation is complex and any quantitative analysis is subject to noise and imaging artifacts in addition to any real temporal changes in the flow structure.

4.3. Jet Structure

We now turn from jet shape and flow speeds to examine what can be learned about the internal structure of the jet from its intensity distribution. The pronounced edge brightness is a clear sign that the jet is not uniform and that the main emission comes from the edge. This raises questions such as how thick is the emitting region and what might be in the center. Doppler boosting implied by the relativistic motions and helical jet flow also have implications for the intensity distribution of the jet that are compared with the imaging results. Interpreting the brightness distribution has to begin with an understanding of what part of the jet is actually being observed along a given line of sight in a jet oriented close to the line of sight.

4.3.1. Lines of Sight

The line of sight through the jet axis passes through the jet near side, center, and far side at significantly different core distances. This complicates understanding the implications of the transverse intensity profiles for sheath and spine emission structure. It also complicates the use of mid-jet as opposed to jet edge proper motions for understanding the jet flow and Doppler beaming effects. For example, at a viewing angle of 17° , a sightline that passes through the jet axis at 1 mas from the core passes through the far side and near side of the jet at ~ 0.7 and 1.5 mas from the core, respectively. A typical line of sight through the jet axis crosses the near side of the jet from 2 times (close to the core) to 1.5 times farther from the core than it crosses the far side of the jet. As a consequence, the average far-side edge intensity is 3 (close to the core) to 2 times the near-side edge intensity where the sightline leaves the jet (see Figure 6 to compare northern or southern ridgeline intensities at different distances from the core). If emissivity is relatively uniform, the intensity where a sightline crosses the jet axis might be the average of the near-side and far-side “edge” intensities along the sightline. This intensity difference along a sightline through the jet axis is problematic for determination of the near-side, center, and far-side location of observed center-line structures. We will address this issue in what follows.

4.3.2. Sheath and Spine

Transverse slice profiles (see Figures 4 and 5) indicate that the intensity at the jet center line can be less than half that of the bright edges. Production of such edge-brightened profiles requires a high sheath and low spine effective emissivity. If we assume a cylindrical jet and that emission comes only from a sheath of thickness $\Delta R = R_j - R_{sp}$, where R_j and R_{sp} are the radius of the jet and spine, respectively, then the sheath path length through the jet axis for viewing angle θ can be written as $\ell_{cen} = 2\Delta R / \sin \theta$. The path length through the sheath along a line of sight through the jet edge at $(R_j - \Delta R/2)$ (i.e., the midpoint of the sheath) can be written as

$$\ell_{edge}^2 = 4 \frac{R_j^2}{\sin^2 \theta} \left[1 - \left(\frac{R_j - \Delta R/2}{R_j} \right)^2 \right] = 4 \frac{\Delta R [R_j - \Delta R/4]}{\sin^2 \theta},$$

$$\text{and } \ell_{edge} \approx 2 \frac{(R_j \Delta R)^{1/2}}{\sin \theta} \text{ for } \Delta R \ll 4R_j.$$

Thus, a cylindrical jet with uniform sheath emissivity and a jet edge intensity twice the center intensity, as suggested by the transverse slice profiles, means

$$I_{cen} / I_{edge} \approx \ell_{cen} / \ell_{edge} \approx \left(\frac{\Delta R}{R_j} \right)^{1/2} = 0.5 \text{ and } \Delta R \approx R_j/4.$$

The actual jet is expanding, so the intrinsic emissivity and sheath thickness will change with the jet's radius and core distance. In addition, sightlines cross the jet edges and jet axis at very different core distances. However, given that we found the average edge intensity at the distance where a line of sight crosses the jet center line to be on the order of the near-side and far-side average, we can still conclude that the jet consists of a low apparent emissivity jet spine and high apparent emissivity jet sheath with observed emission largely coming from a sheath with thickness on the order of $R_j/4$. Note that these arguments apply once the jet ridges are resolved from each other and the jet expansion is moderate—say, at core distances beyond about 0.5 mas.

For intensity profiles to be as edge brightened as they appear despite the path length along sightlines through the jet spine being on the order of three times the path length through the near-side and far-side jet sheath, the “effective” spine emissivity must be at least an order of magnitude less than the “effective” sheath emissivity. Intrinsic spine emission can be Doppler deboosted relative to intrinsic sheath emission by a factor

$$\epsilon \equiv \left(\frac{\delta_{sp}}{\delta_{sh}} \right)^{2+\alpha} = \left[\frac{\gamma_{sh}(1 - \beta_{sh} \cos \theta)}{\gamma_{sp}(1 - \beta_{sp} \cos \theta)} \right]^{2.55}.$$

To achieve an order-of-magnitude deboosting, $\epsilon \leq 0.1$, for $\theta = 17^\circ$ with the intrinsic sheath speed and Lorentz factor of $\beta_{sh} \approx 0.924$ and $\gamma_{sh} \approx 2.62$ appropriate between 1 and 4 mas would require a spine Lorentz factor and speed of $\gamma_{sp} \geq 16.5$ and $\beta_{sp} \geq 0.998$. This required minimum gives an apparent motion at $\theta = 17^\circ$ of $\beta^{app} \geq 6.4$. This lower limit is consistent with the $\beta^{app} = (6.1 \pm 0.6)$ seen at HST-1 in the optical by

Biretta et al. (1999) and the $\beta^{app} = (6.4 \pm 0.8)$ of the fastest component seen in the radio by Giroletti et al. (2012). Thus, it is possible that a high-speed Doppler deboosted spine lies within the slower-moving sheath.

4.3.3. Rotation, Expansion, and Doppler Boosting

The presence of clockwise helical flow in the sheath would lead to differential Doppler boosting across the jet. If we consider the values found above for the region between 0.5 and 1 mas (1 and 4 mas region in parentheses) of $\Delta\phi_h \approx 7:8$ ($\approx 2:9$) and $\beta_h \approx 0.56$ (≈ 0.924) with $\theta_{edge} \approx 17:6$ ($\approx 17:3$), then we would predict an enhanced Doppler boost of the southern jet edge relative to the northern jet edge in the range

$$\left(\frac{\delta_S}{\delta_N} \right)^{2+\alpha} = \left[\frac{1.0 - \beta_h \cos(\theta_{edge} + \Delta\phi_h)}{1.0 - \beta_h \cos(\theta_{edge} - \Delta\phi_h)} \right]^{2.55} \approx 1.3 - 1.8,$$

where the numerical value range corresponds to the results for 0.5–1 mas and 1–4 mas in that order.

This predicted differential Doppler boosting is lower closer to the core. A comparison of ridgeline intensities from Figure 6 shows a southern ridgeline intensity equal to or greater than the northern ridgeline intensity at core distances >0.8 mas. However, the northern ridgeline intensity is higher at core distances <0.8 mas in the 23-epoch image. While the ratio is significantly less close to the core, it would still predict a brighter southern edge. It seems more likely that the maximum edge intensity is a function of change in jet direction associated with long-term epoch evolution (see Figures 16–18), and jet edge intensity differences are not likely the result of differential Doppler boosting resulting from rotation.

There will also be differential Doppler boosting between the near side (ns) and far side (fs) of the jet along lines of sight through the jet axis because, thanks to the jet opening angle, the sides are at different angles to the line of sight. If we consider $\beta_h \approx 0.56$ with opening angle $\psi \approx 4:5$ between 0.5 and 1 mas, and $\beta_h \approx 0.924$ between 1 and 4 mas with $\psi \approx 3^\circ$, then we would predict an enhanced Doppler boost of the near side relative to the far side in the range

$$\left(\frac{\delta_{ns}}{\delta_{fs}} \right)^{2+\alpha} = \left[\frac{1.0 - \beta_h \cos \theta_{fs}}{1.0 - \beta_h \cos \theta_{ns}} \right]^{2.55} \approx 1.15-1.85,$$

where the smaller value is closer to the core, and $\theta_{fs} \approx \theta + \psi$ and $\theta_{ns} \approx \theta - \psi$. This amount of differential Doppler boost between near side and far side can partially compensate for higher far-side intrinsic intensities along lines of sight through the jet axis.

Clockwise helical flow around the jet will lead to apparent transverse motion across the jet center line with northward apparent transverse motions across the near side of the jet and southward apparent transverse motions across the far side of the jet. MLWH find a tendency toward northward apparent transverse motions, and this indicates a bias toward seeing motions on the near side of the jet (see Figures 2 and 3 in MLWH).

4.4. Long-term Pattern Motion

In Section 3.4, we showed that the transverse position of the jet shifts on a quasi-periodic ~ 8 – 10 yr timescale. This period provides a characterization of the variation timescale but does not have an adequate time span to claim true periodic motion such as would be expected from precession. In this section, we discuss the implications of these shifts for the properties of the interface between the jet and external medium if their propagation is described by the Kelvin–Helmholtz helical mode.

The structural variations observed are consistent with a jet base that changes direction on the timescale noted above, leading to a variation in flow direction that appears to propagate down the jet at apparent speeds $\beta_p^{\text{app}} \approx 0.81$ – 0.89 , where the range is set by the two different methods to determine the speed used in Section 3.4.2. At a viewing angle of $\theta = 17^\circ$, the intrinsic pattern motion range is $\beta_p \approx 0.76$ – 0.78 . The intrinsic pattern motion is significantly greater than the slower intrinsic component motions from MLWH of $\beta_h \approx 0.553$ but is significantly less than the faster intrinsic component motions from MLWH of $\beta_h \approx 0.924$ at distances beyond 1 mas. MLWH suggested that the fast- and slow-component motions associated with the bright jet edges indicated velocity shear associated with the jet–external medium interface. Thus, we suggest that the pattern can be thought of as moving through an external (e) medium that itself can be moving with flow speed $0 < u_e < 0.553c$, but that the pattern moves more slowly than the internal jet (j) flow speed, which is $u_j > 0.924c$.

In what follows let us assume that the jet with flow speed $\beta_j > 0.924$ ($\gamma_j > 2.62$), determined by the MLWH faster-moving jet components beyond 1 mas, is separated by a sharp velocity discontinuity from an external medium with flow speed $\beta_e < 0.553$ ($\gamma_e < 1.20$), determined by the MLWH slower-moving components beyond 1 mas. We assume a direction change at the jet base on a ~ 9 yr timescale and that this direction change propagates with an intrinsic pattern speed of $\beta_p \approx 0.770$.

A nonballistically moving bulk displacement of the jet can be described by the properties of the Kelvin–Helmholtz helical mode (see Hardee 2007) provided that the displacement frequency is less than the resonant frequency (see Equation (8)). See Appendix C for a brief review of the important equations. Numerical study shows that the helical mode above resonance does not lead to bulk displacement of the jet as a whole (Hardee et al. 2001). Below resonance the helical mode propagation properties are relatively insensitive to the presence of a velocity shear layer (see Birkinshaw 1991). The important propagation properties are revealed by analytical approximations for helical wave propagation along a cylindrical jet with purely poloidal flow and magnetic field inside and outside a sharp velocity shear edge (see Hardee 2007). A simple linear displacement at the jet base can be described by two counterrotating equal-amplitude helical displacements. Provided that flow and magnetic helicity are relatively small beyond 1 mas, approximations to pattern motions assuming no helicity should prove adequate for estimating the jet–external medium interface properties required to produce the observed pattern motion.

The ~ 9 yr timescale for the change in direction at the jet base implies an angular frequency of $\omega \approx 7 \times 10^{-9} \pi \text{ rad s}^{-1}$. An estimate for the conditions required for the lower limit to the resonant frequency to exceed this angular frequency can be obtained by assuming that, in the “sonic” limit, the sound

speeds in the jet and external medium are the same or that, in the “Alfvénic” limit, the Alfvén speeds in the jet and external medium are the same. Here the “sonic” limit means that the sound speed greatly exceeds the Alfvén speed (weakly magnetized flow scenario), and the “Alfvénic” limit means that the Alfvén speed greatly exceeds the sound speed (strongly magnetized flow scenario). In these scenarios the resonant frequency (see Equation (9))

$$\omega^* \gtrsim \frac{3\pi v_w}{4 R_j} > \omega \approx 7 \times 10^{-9} \pi \text{ rad s}^{-1},$$

at, say, 3 mas, where $R_j \approx 0.9 \text{ mas} \approx 2.25 \times 10^{17} \text{ cm}$ provided that $v_w \geq 0.07c$. We have used the FWHM value for the jet width at 3 mas from Figure 24 to estimate R_j , and v_w is the sound speed in the sonic limit or the Alfvén speed in the Alfvénic limit. This required lower limit to the sound speed or Alfvén speed in the jet and external medium at about 7% of light speed lies well below the maximum possible sound speed or Alfvén speed of $c/\sqrt{3}$ or $\lesssim c$, respectively. Thus, it is clearly possible for a quasi-periodic ~ 9 yr timescale jet displacement to be described by the low- to resonant-frequency helical mode propagation properties.

Pattern motion, v_p , is a function of the jet speed u_j , the external medium speed u_e , and the enthalpy ratio, W_j/W_e , between the jet and external medium. Here the enthalpy $W \equiv \rho + [\Gamma/(\Gamma - 1)]P/c^2$, where ρ , P , and Γ are the rest mass density, pressure, and adiabatic index, respectively.

If pattern motion is described by helical mode propagation below the resonant frequency, the required enthalpy ratio is given by Equation (12). If magnetic fields are small, then in the sonic limit $W_j \approx [(v_p - u_e)/(u_j - v_p)](\gamma_e/\gamma_j)^2 W_e$, where $1.5 \leq [(v_p - u_e)/(u_j - v_p)] \leq 5$ and $0.21 \geq (\gamma_e/\gamma_j)^2 \geq 0.14$ for $\beta_j = 0.924$ ($\gamma_j = 2.62$) and $\beta_e < 0.553$ ($\gamma_e < 1.20$). If $\rho \gg P/c^2$, the jet is similar in density to the surrounding medium unless the faster-moving jet components are not truly representative of the underlying jet flow. A much faster jet flow of $\gamma_j = \gamma_{\text{sp}} \gtrsim 16.5$ ($\beta_{\text{sp}} \gtrsim 0.998$) such as required to Doppler deboost the spine and produce the apparent $\sim 6c$ superluminal motions in the optical at HST-1 implies a jet over an order of magnitude less dense than the surrounding external medium. If magnetic fields are large, then in the Alfvénic limit $W_j \approx [v_p/(u_j - v_p)](\gamma_A/\gamma_j)^2 W_e$, where $[v_p/(u_j - v_p)] \approx 5$ and $\gamma_A \approx [\gamma_e^2(1 - u_e/v_p) + (B_e^2 + B_j^2)/4\pi W_e c^2]^{1/2}$. The Alfvénic limit suggests somewhat higher jet density relative to the unmagnetized case, as in general $(\gamma_A/\gamma_j)^2 > (\gamma_e/\gamma_j)^2$.

If pattern motion is more accurately described by helical mode propagation near the resonant frequency, the required enthalpy ratio is given by Equations (13). The principal difference with the low-frequency form lies in the square in the velocity term so that $W_j \approx [(v_p - u_e)/(u_j - v_p)]^2 (\gamma_e/\gamma_j)^2 W_e$, where $2.25 \leq [(v_p - u_e)/(u_j - v_p)]^2 \leq 25$ and $0.21 \geq (\gamma_e/\gamma_j)^2 \geq 0.14$ for $\beta_j = 0.924$ ($\gamma_j = 2.62$) and $\beta_e < 0.553$ ($\gamma_e < 1.20$). Thus, if the pattern motion is described by a helical mode propagation near resonance and $\rho \gg P/c^2$, a jet density comparable to the external medium density would provide the properties required by the observed pattern motion. Once again, a much faster jet of $\gamma_j = \gamma_{\text{sp}} \gtrsim 16.5$ ($\beta_{\text{sp}} \gtrsim 0.998$) implies a jet over an order of magnitude less dense than the surrounding external medium.

Overall this analysis would lead us to believe that a jet rest mass density somewhat less (to about an order of magnitude less) than the external medium density would provide the properties required by the observed pattern motion. The external medium referred to here is not the interstellar medium but rather the immediate cocooning medium surrounding the jet and likely an outflowing magnetized wind from the accretion disk.

There is no evidence for bulk displacement of the jet at arcsecond scales until knot A. This implies that the bulk displacement that we observe at milliarcsecond scales is damped at larger scales. Theory and numerical simulation show that damping of a displacement will occur in the presence of strong magnetic fields (see Equation (14) and Mizuno et al. 2007). Even if this condition is not met, a bulk displacement of the jet at the jet base that can be described by a wave frequency ω that is initially less than the local resonant frequency ω^* can propagate down the expanding jet to where ω is above the local resonant frequency because $\omega^* \propto R^{-1}$ declines along an expanding jet. Thus, an initial bulk displacement at the jet base can become damped at larger distances.

5. Summary

Because of proximity and large black hole mass, M87 is the best available source in which to study the region close, in terms of gravitational scales, to where a jet is launched. This paper presents the main observational results from a program of intensive monitoring of the subparsec- to parsec-scale structure of M87 in 2007 and 2008 and from roughly annual observations from 1999 to 2016 using the VLBA at 43 GHz. A total of 50 observations are included.

The major results of the study are as follows:

1. The images clearly show a wide opening angle jet base and edge-brightened structure.
2. The jet has an overall parabolic shape as reported previously, but with regions of rapid expansion and recollimation.
3. Mildly superluminal motions with apparent speeds of $\beta^{\text{app}} \approx 2$ are seen beyond about 2 mas (0.16 pc in projection) from the core.
4. A region of acceleration is seen in the inner 0.5–2 mas, confirming results presented in MLWH that were based on a new analysis method applied to some of the observations reported in this paper. This region is at an intrinsic (deprojected) core distance of about 0.14–0.55 pc or $240R_S$ – $960R_S$ along the jet for our assumed angle to the line of sight (17°), distance (16.7 Mpc), and black hole mass ($6.1 \times 10^9 M_\odot$).
5. The jet structure is consistent with an unseen spine with the radio emission coming from a sheath with a thickness of about one-quarter of the jet radius.
6. The counterjet is clearly seen and has a structure similar to the main jet, but with brightness that decays more rapidly with distance, presumably because of Doppler boosting.
7. The jet/counterjet brightness ratios indicate an acceleration zone leading to high speeds. However, the ratios do not get as high as expected for the component superluminal motions observed, perhaps because of less beamed emission from material providing the slower-component motions seen by MLWH.
8. The north/south brightness ratios, the north/south edge speed ratios, and the jet/counterjet brightness ratios for

the north and south edges all point to a clockwise helical flow (as viewed by an observer on the jet side looking toward the core).

9. The roughly annual observations over 17 yr reveal transverse motions of the inner parsec of the jet that are consistent with a slow change in jet position angle superimposed on an oscillation with a period of about 8–10 yr. These motions have not been reported before to our knowledge.
10. The oscillation pattern seen in the long-term observations propagates nonballistically along the jet at an apparent speed somewhat less than half that of the fast-component motions seen by MLWH.
11. The nonballistic propagation speed of the long-term patterns is consistent with Kelvin–Helmholtz instability wave propagation speed along a jet with density comparable to or less dense than the cocooning environment.
12. The polarization data show a consistent pattern for two epochs and suggest a toroidal magnetic field geometry.

We will not attempt detailed comparisons of our data with existing jet launch models and simulations. But our observations are consistent with general classes of models where the radio emission region is in the outer portions—the sheath—of a symmetric jet launched by magnetic fields threading an accretion disk (see Blandford & Payne 1982; Blandford & Zanjek 1977; McKinney 2006; McKinney & Blandford 2009). The sheath material is accelerated over the inner $500R_S$ – $1000R_S$ to mildly relativistic speeds ($\gamma_j > 2$). The dark center of the jet allows for a jet spine that might be launched from the black hole and could be faster than the sheath that we see.

Below we discuss the various results in more detail.

5.1. Jet Structure: Edge Brightening and Counterjet

All of the images show a strongly edge-brightened structure with a wide opening angle base as originally reported by Junor et al. (1999). They also show the existence of a counterjet, also edge brightened, that fades much more rapidly than the main jet. Much of the analysis of jet structure presented here is based on an average image made from the 23 epochs of the intensive monitoring observations in 2007 and 2008. That image smooths out the variable structure, giving a high-sensitivity picture of the persistent aspects of the structure. Transverse intensity slices of the average image show that jet and counterjet have similar width structure out to 1.2 mas, beyond which the counterjet becomes too faint to follow. The symmetric structure between the jet and counterjet places the radio core to within 0.06 mas (half the spacing between slices and one-quarter the beamwidth) of the central engine, consistent with the core location found by Hada et al. (2011) from the core shift with frequency.

5.1.1. Expansion and Collimation Regions

Overall the jet shows three intrinsic expansion/collimation regimes: (1) a rapid $\sim 19^\circ$ expansion followed by a contraction, (2) a second rapid $\sim 19^\circ$ expansion beginning at about $530R_S$ and followed by a recollimation, and (3) a third slower expansion of $\sim 6.5^\circ$ beginning at about $1800R_S$ and followed by a slow recollimation. Changes in the slope of the jet intensity decline are associated with changes in jet expansion. The average expansion is consistent with the parabolic expansion found by Asada & Nakamura (2012) to apply out to HST-1, as

well as the initial parabolic expansion found by Hada et al. (2013) inside $300R_s$. However, our results show more complex variable expansion than a single parabolic outside $300R_s$. In retrospect, some evidence for this complex behavior can be found in Hada et al. (2013). Using high-resolution observations at 86 GHz, Hada et al. (2016) find an additional region of expansion and contraction closer to the core than those seen at 43 GHz. The multiple expansion/collimation regimes indicate a nonequilibrium jet-launching region in which equilibrium parabolic expansion is achieved only after several thousand R_s .

5.1.2. Spine/Sheath Structure

The very edge-brightened jet and counterjet suggest that most of the emission comes from a sheath surrounding a low “effective” emissivity spine. On the jet side, the edge-brightened structure that we see from the unresolved radio core out to at least 20 mas is comparable to edge-brightened structure along the parsec-scale jet from about 40 to 200 mas (see Figure 2 in Reid et al. 1989) and is even more pronounced on the kiloparsec-scale jet (see Owen et al. 1989; Hardee & Eilek 2011). Transverse intensity profiles and line-of-sight effects imply a sheath with thickness of about one-quarter of the jet radius. Reduction of an intrinsic spine emissivity comparable to the intrinsic sheath emissivity by Doppler deboosting relative to the sheath would require a spine Lorentz factor $\gamma_{sp} \geq 16.5$ relative to an observed typical sheath Lorentz factor of $\gamma_{sh} \approx 2.6$. This required spine Lorentz factor would result in an apparent motion at a 17° viewing angle of $\beta^{app} \geq 6.4$ that is consistent with observed optical proper motions of $\beta^{app} = 6.1 \pm 0.6$ at HST-1.

5.1.3. Filaments

The average intensity image and its transverse profile structure indicate faint jet-crossing filaments. Faint cross-jet filamentary structure inside 20 mas begins to show up more prominently on the parsec scale jet from about 40 to 200 mas (see Figure 2 in Reid et al. 1989) and is even more pronounced on the kiloparsec-scale jet (see Owen et al. 1989; Hardee & Eilek 2011).

5.1.4. Edge Brightness Variations

There are systematic differences in the edge intensities between the sides of the jet, although there are short-term variations in those differences. In the innermost 0.7 mas the northern edge of both jet and counterjet is brighter than the southern edge, but farther out the jet’s southern edge is usually equal to or brighter than the northern edge. The most likely reason for intrinsic spatial edge intensity differences is the approximately 8–10 yr quasi-periodic intrinsic change in the flow direction at the jet base discussed below. However, other, more rapid events can also produce significant changes. Within the 1.2 yr time frame covered by the 23-epoch average image, significant intensity change within the inner few mas was observed. In particular, the weekly observations in early 2008 tracked a core brightening, associated with a VHE flare event in early 2008 February, which led to jet edge brightening inside 1 mas over the following 2 months. More recently, Hada et al. (2014) found a similar jet base brightening associated with an elevated VHE state in 2012. The deviation of the brightness centroid to below the mean jet position angle inside 20 mas found by Reid et al. (1989) appears related to our finding that the southern edge is brighter than the northern edge. The Reid et al. (1989)

results suggest a quasi-periodic oscillation of the brightness centroid from about 5 to 80 mas that is likely related to a quasi-periodic variation in the northern and southern edge brightness. Deviation of the brightness centroid between HST-1 and knot D at considerably larger angular scales (see Owen et al. 1989; Hardee & Eilek 2011) may or may not be related to that seen on the parsec-scale jet.

5.2. Jet Motions

The individual images from 2007 and 2008 are used to study the dynamics of the inner jet and reveal a jet with complicated motions that clearly accelerates to mildly superluminal speeds over the inner 2 mas. Our component motion analysis gives results similar to an analysis by MLWH of the motions in our 2007 data using a wavelet-based analysis scheme. The discrepancy between reports of fast motions based on our data (e.g., Walker et al. 2008, MLWH) and recent KaVA results (Hada et al. 2017) and slower motions seen at lower frequencies (e.g., Reid et al. 1989; Kovalev et al. 2007) may be the result of the presence of both faster and slower motions as indicated explicitly by the wavelet-based analysis of MLWH.

The component motion analysis of the 2007 data using a wavelet-based scheme in MLWH revealed both jet acceleration and significant differences in apparent speeds along the jet edges. Along the jet between 0.5 and 1 mas there was a higher apparent speed along the north edge relative to the south edge. Farther downstream between 1 and 4 mas the fast component had higher apparent speed on the north edge relative to the south edge. Meanwhile, the slow component had lower apparent speed on the north edge relative to the south edge. The presence of a high-speed and a low-speed component between 1 and 4 mas led MLWH to infer the presence of a velocity shearing sheath.

5.2.1. Counterjet/Jet Intensity Sidedness Ratios

The counterjet structure was studied with two recent, high-sensitivity epochs that were processed for higher resolution and also with an average of 49 epochs (all but the last), which allows the counterjet to be followed to about 1.7 mas. In general, the intensity sidedness ratio increases as a function of core distance, indicating that the jet material is accelerating at the core distances where the counterjet can be seen. Beyond that distance, the material speed, combined with the brightness decrease along the jet, drops the counterjet intensity to below detectable levels. But the sidedness ratio seen in the 49-epoch average image indicates not as much acceleration as seen in the component motions. Perhaps the intensity ratio is not as high as expected because of the effects of the slow component seen by MLWH between 1 and 4 mas, which would not be as strongly beamed. Counterjet/jet intensity sidedness ratios using the 49-epoch average image along the counterjet and jet edges symmetric across the core show systematic north/south differences. At very small scales the two higher-resolution image intensity ratios probe the first rapid counterjet and jet expansion region. Again systematic north/south differences are seen.

5.2.2. Helical Flow

Apparent sheath motions along the northern jet edge are faster than apparent sheath motions along the southern jet edge.

These differences in component motions along the north and south jet edges can be explained best as the result of a clockwise helical flow. For clockwise helical flow, flow along the northern jet edge is farther from the line of sight and closer to the critical angle at which apparent speeds are maximized, whereas flow along the southern jet edge is closer to the line of sight and farther from the critical angle. The helical flow accelerates from $\beta_h \approx 0.56$ between 0.5 and 1 mas to $\beta_h \approx 0.924$ between 1 and 4 mas, with the flow becoming more poloidal at the larger distances. The systematic north/south differences in the counterjet/jet intensity sidedness ratios seen in both the 49-epoch average image and the two high-resolution images are consistent with, and help confirm, the clockwise helical flow scenario suggested by the jet component motions inside 1 mas. In the high-resolution images, the better-quality 2013 image indicates clockwise helical flow with acceleration from $\beta_h \approx 0.5$ to $\beta_h \approx 0.8$ between 0.4 and 0.6 mas in the rapid counterjet and jet expansion region, consistent with the fast-component motions found by MLWH between 1 and 4 mas. The 2016 image intensity ratios indicate a potential for counterclockwise helical flow beyond ~ 0.6 mas, consistent with the slow-component motions found by MLWH between 1 and 4 mas. The slow-component edge speed differences between 1 and 4 mas could result from a counterclockwise helical flow with $\beta_h \approx 0.55$. This result suggests a complex-velocity-shear sheath region.

The clockwise helical flow scenario is consistent with the observed tendency toward northward apparent transverse motions across the jet, where northward transverse motions are associated with flow on the near side of the jet. Assuming the same helical sense for the filaments would indicate clockwise helical filamentary structure. Differential Doppler boosting between the near side and far side of the jet, due to the opening angle, predicts an enhancement of the near side relative to the far side that can partially compensate for the higher far-side intensities nearer to the core along lines of sight through the jet axis. Differential Doppler boosting from rotation would give a brighter southern edge relative to the northern edge as seen beyond about 1 mas. However, the northern edge is brighter than the southern edge close to the core, and this fact, along with spatial and temporal variation in relative northern and southern edge intensities at subparsec, parsec, and kiloparsec jet scales, suggests that edge intensity differences are not entirely due to rotation-induced differential Doppler boosting.

5.3. Long-term Transverse Motions

The long-term, roughly annual observations show that the position angle of the jet has been changing, with both a systematic increase and an approximately sinusoidal oscillation with a period of roughly 8–10 yr. A recent 3D GRMHD simulation by Tchekhovskoy et al. (2011) indicated that quasi-periodic variation in jet direction is a natural consequence of the jet acceleration and collimation process. The observed change in jet angle propagates outward at about 3.2 mas yr^{-1} ($\beta_p^{\text{app}} \approx 0.85$), which is less than the high-speed components ($\beta_p^{\text{app}} \gtrsim 2$) seen by MLWH and by our component analysis between 1 and 4 mas. This nonballistic propagation speed is the expected result for a Kelvin–Helmholtz instability in a jet with density comparable to or less dense than the cocooning

environment (see Hardee 2007). We note, however, that there is no evidence for bulk sideways displacement of the jet at arcsecond scales until knot A. Damping of a bulk displacement at larger scales will occur naturally in the presence of strong magnetic fields (see Mizuno et al. 2007) or if the quasi-periodicity frequency exceeds a local resonant frequency that scales inversely with the jet radius and declines along an expanding jet.

5.4. Magnetic Fields

While most of the polarization data have yet to be reduced, two epochs show similar systematic polarization structure. Near to the core the polarization is up to 1.5% on the jet side, where the magnetic field vectors are perpendicular to the jet axis, suggesting a toroidal configuration. Just beyond the core, the magnetic field vectors on the edge-brightened jet appear parallel to the jet axis. Polarization on the counterjet side of the core is less than 1%, and the magnetic field vectors appear parallel to the counterjet axis. Flow-aligned magnetic field vectors might be indicative of velocity shear in the sheath. On the other hand, the emission apparently on the counterjet side could actually be from the optically thick portion of the inner main jet but spread toward the counterjet by resolution effects, as a 90° polarization angle change between optically thick and thin parts of the jet is seen in many VLBI sources.

5.5. Future Work

The data sets reported on here constitute a rich source of information about the M87 jet on gravitational scales that cannot be reached in most systems. There is much left to be done. We have only barely begun to utilize the polarization information that should shed light on the magnetic field structure and its dynamics along the inner jet. Also, the observing sessions since 2009 included enough time at 24 GHz to make images at that frequency of similar quality to those at 43 GHz. This additional frequency will allow delineation of the spectral index in the inner regions and also, because the jet is somewhat brighter at the lower frequency and the phase stability is better, should allow extension of some of the studies reported here to larger scales. The observations also included astrometric observations targeting the relative positions of M87 and another large, Virgo Cluster elliptical, M84. The astrometry will shed light on any possible core wander and on the relative transverse motions of the two galaxies. The astrometric study is close to completion, with most of the data reduction done (F. Davies, et al. 2018, in preparation).

P.E.H. acknowledges support from NSF awards AST-0506666 and AST-0908010 and NASA/ATP awards NNX08AG83G and NNX12AH06G to the University of Alabama. This work made use of the Swinburne University of Technology software correlator, developed as part of the Australian Major National Research Facilities Programme and operated under license. Earth Orientation and Ionospheric data hosted on the Crustal Dynamics Data Information System (CDDIS) at the NASA Goddard Space Flight Center were used in this project. This study makes use of 43 GHz VLBA data

from the VLBA-BU Blazar Monitoring Program (VLBA-BU-BLAZAR; <http://www.bu.edu/blazars/VLBAproject.html>), funded by NASA through the *Fermi* Guest Investigator Program. C.L. and F.B.D. were summer students at the NRAO when they became involved in this project.

Appendix A Symbol Table

Table 2 is a list of all the symbols used in this paper.

Table 2
Symbol Definitions

Symbol	Definition
a_1	Linear change in R_c with distance
a_2	Linear change in R_c with time
a_3	Sine wave amplitude at $z = 0$
a_4	Power-law index of sine wave amplitude dependence on z
a	Sound speed
$a_{j,e}$	Jet, external medium sound speed
B	Magnetic field strength
$B_{j,e}$	Magnetic field strength in jet, external medium
c	Speed of light
f	Sine wave frequency (cycles mas^{-1})
G	Gravitational constant
$I_{j,cj}$	Intensity on the jet, counterjet side
$I_{j,cj}^{N,S}$	Intensity on the north, south side in the jet, counterjet direction
$I_{j,cj}^{\text{Max}}$	Maximum intensity on jet, counterjet side
I_{cen}	Intensity along projected jet center
I_{edge}	Intensity along the edge of the jet
ℓ_{edge}	Path length through sheath, cylindrical jet
ℓ_{cen}	Path length through sheath along projected jet center line
M	Mass of black hole
M_{\odot}	Solar mass
P	Pressure
R_S	Schwarzschild radius ($2GM/c^2$)
R_c	Offset from the nominal jet center line
R_0	R_c at date 2000.0
R_{NS}	$(I_{cj}^N/I_j^S)^{1/(2+\alpha)}$
R_{SN}	$(I_{cj}^S/I_j^N)^{1/(2+\alpha)}$
R_j	Radius of jet
R_{sp}	Spine radius
t_{yr}	Date in fractional years
t	Date-2000.0 (for fits)
t_d	Time minus pattern propagation time from core ($t - z/v_p$)
$u_{e,j}$	External medium, internal jet flow speed
v^{app}	Observed (apparent) speed
v_h	Helical mode wave speed at low frequency
v_h^*	Helical mode wave speed at resonance
v_p	Pattern propagation speed (mas yr^{-1})
v_A	Alfvén speed
$v_{A,j,e}$	Jet, external medium Alfvén speed
v_w	Helical wave speed below resonance
$v_{w,j,e}$	$\equiv (a_j, v_{A,j})$ in sonic or Alfvénic limits for jet, external medium
V_A	$\equiv B^2/(4\pi W)$
V_{As}	“Surface” Alfvén speed
W	Enthalpy
$W_{j,e}$	Enthalpy in jet, external fluid

Table 2
(Continued)

Symbol	Definition
z	Core distance in mas; an increment: Δz
α	Spectral index $I \propto \nu^{-\alpha}$
β	Intrinsic speed as a fraction of the speed of light
$\beta_{\text{edge}}^{\text{app}}$	Apparent speed in projection on edge of jet
β^{app}	Apparent speed in projection
$\beta_{N,S}^{\text{app}}$	Apparent speed on north, south edge of the jet
$\beta_{j,cj}^{\text{app}}$	Apparent speed on jet, counterjet side
β_p	Intrinsic pattern speed
β_p^{app}	Apparent pattern speed
β_{edge}	β on edge of jet
$\beta_{\text{sp,sh}}$	Intrinsic β in the spine, sheath
β_h	Intrinsic β along a helical path
β_e	External sheath medium flow speed
γ	Lorentz factor
$\gamma_{\text{sp,sh}}$	Spine, sheath Lorentz factor
$\gamma_{e,j}$	External medium, jet Lorentz factor
$\gamma_{w,j,e}$	Sonic or Alfvénic Lorentz factor in jet, external medium
$\gamma_{aj,ae}$	Sonic Lorentz factor, jet or external medium
γ_A	Alfvénic Lorentz factor
$\gamma_{A,j,Ae}$	Alfvénic Lorentz factor, jet or external medium
Γ	Adiabatic index
ΔW	Change in jet width
ΔR	Sheath thickness
$\delta_{\text{sp,sh}}$	Spine, sheath Doppler factor
$\delta_{\text{ns,fs}}$	Doppler factor on near, far side of the jet
$\delta_{S,N}$	Doppler boost factor of northern and southern edges of jet
ϵ	Deboosting of spine emission
η	$\equiv \gamma_j^2 W_j / \gamma_e^2 W_e$
θ	Viewing angle between jet axis and line of sight
θ_{edge}	Viewing angle between jet edges and line of sight
$\theta_{\text{fs,ns}}$	Viewing angle of jet edges along line of sight through jet axis
θ_{crit}	Critical angle to line of sight for maximum β^{app}
Θ	Jet intrinsic full opening angle in a jet segment
Θ^{app}	FWHM apparent opening angle
ν	Frequency
ρ	Density
ϕ_0	Sine wave phase (deg) at $t_d = 0$
$\Delta\phi_h$	Flow angle relative to pure poloidal flow along jet edges
ψ	Intrinsic half opening angle
ω^*	Helical mode resonant frequency
ω	Angular wave frequency

Appendix B List of Observations

Table 3 lists all of the observations that contributed to this paper. There were additional observations associated with some of the projects, but, if they were not used in the paper, they do not appear here. Table 4 lists the average images that were used in Figure 17 and in the long term analysis. These were each made using a noise weighted average of images from observations made within a single year.

Table 3
VLBA Observation Sessions That Contributed Data to This Paper

Observation Code	Date	MJD	Bit Rate ^a (Mbps)	rms ^b (μ Jy beam ⁻¹)	Integrated ^c Flux Density (Jy)	Peak ^d Flux Density (Jy beam ⁻¹)
GJ009 ^e	1999 Mar 04	51241	256	204	0.52	0.28
BJ031B ^f	2000 Apr 09	51643	256	387	1.23	0.60
BW054C ^g	2001 Oct 12	52194	256	709	1.53	0.53
BU021 ^h	2002 Jun 02	52427	256	540	1.49	0.58
BW070 ⁱ	2004 Apr 05	53100	256	773	1.26	0.61
BW082A	2006 Apr 08	53833	128	247	1.59	0.80
BW082B	2006 Apr 11	53836	128	235	1.60	0.80
BW082D	2006 Apr 18	53843	128	273	1.69	0.82
BW082E	2006 Apr 21	53846	128	268	1.46	0.81
BW082F	2006 May 14	53869	128	307	1.67	0.79
BW082G	2006 Jul 14	53930	128	276	1.35	0.57
BW088A	2007 Jan 27	54127	256	184	1.75	0.64
BW088B	2007 Feb 17	54148	256	209	1.60	0.60
BW088D	2007 Mar 13	54172	256	205	1.80	0.70
BW088E	2007 Apr 03	54193	256	201	1.70	0.68
BW088F	2007 Apr 23	54213	256	198	1.86	0.67
BW088G	2007 May 10	54230	256	175	1.82	0.70
BW088H	2007 Jun 03	54254	256	199	1.63	0.60
BW088I	2007 Jun 22	54273	256	185	1.43	0.51
BW088J	2007 Jul 16	54297	256	225	1.58	0.58
BW088K	2007 Aug 04	54316	256	216	1.65	0.60
BW088L	2007 Aug 26	54338	256	223	1.80	0.68
BW088P	2007 Nov 02	54406	256	192	1.53	0.58
BW088U	2008 Jan 21	54486	256	202	1.86	0.81
BW090A	2008 Jan 26	54491	256	197	1.88	0.83
BW090B	2008 Jan 31	54496	256	189	1.97	0.82
BW090C	2008 Feb 04	54500	256	291	1.97	0.82
BW090E	2008 Feb 15	54511	256	193	2.10	0.94
BW090F	2008 Feb 20	54516	256	249	2.19	1.01
BW090G	2008 Feb 25	54521	256	169	2.23	1.00
BW090H	2008 Mar 02	54527	256	191	2.24	1.04
BW090J	2008 Mar 12	54537	256	158	2.36	1.10
BW090K	2008 Mar 19	54544	256	170	2.38	1.10
BW090L	2008 Mar 24	54549	256	159	2.37	1.09
BW090N	2008 Apr 05	54561	256	167	2.44	1.13
BW092A	2009 Jan 19	54850	256	268	1.46	0.66
BW093A	2010 Jan 18	55214	256	271	1.41	0.66
BW093B	2010 Apr 04	55290	256	210	1.55	0.68
BW093C	2010 Apr 19	55305	256	231	1.58	0.65
BW093D	2010 May 01	55317	256	227	1.48	0.66
BW093E	2010 May 16	55332	256	240	1.42	0.63
BW093F	2010 May 31	55347	256	247	1.31	0.62
BW095B	2011 Feb 13	55605	512	182	1.71	0.86
BW097A	2012 Jan 06	55932	512	185	1.43	0.64
BW098A ^j	2013 Jan 12	56304	2048	67	1.51	0.62
BW106 ^k	2013 Jun 04	56447	2048	80	1.40	0.56
BW107 ^l	2013 Dec 27	56653	2048	149	1.44	0.61
BW115A	2015 Jan 26	57048	2048	92	1.66	0.73
BW115D	2016 Mar 14	57461	2048	72	1.78	0.75
BW115H ^m	2016 Apr 10	57488	2048	84	1.65	0.70

Notes. Additional observations were made and are in the archive, but they were not used in this paper for various reasons, including poor data quality and processing difficulties.

^a The total recording rate in bits per second. For these projects, there are two bits per sample, two samples per Hz of bandwidth, and two polarizations, so the recording rate is eight times the spanned bandwidth.

^b The noise level was measured using a histogram fit to the final image prior to adjusting the convolving beam used for the point CLEAN components to match the common resolution. When the beam size adjustment is made (AIPS task CCRES), the residual image, including any low-resolution components from the multiresolution CLEAN, is scaled by the ratio of beam areas. This is correct for the regions with emission but is somewhat problematic for the noise. The rms of the unsealed image should provide a better comparison of the quality of the images. Note that the scaling of the residual image is by less than 20% for all but four images, but there are outliers.

^c The integrated flux density is the sum of all CLEAN components of all resolutions from the very deep CLEANs used in the imaging.

^d The peak flux density is measured on the images for which the point CLEAN components are convolved with a common beam size of 0.43×0.21 mas, elongated along position angle -16° .

^e Global observations involving VLBA and European VLBI Network antennas. Single polarization. The flux density calibration is highly suspect but has not been revisited. See Junor et al. (1999).

^f Included the phased VLA. See Ly et al. (2007).

^g Ly et al. (2004).

^h Archival data. M87 was a phase reference calibrator. See Ly et al. (2007).

ⁱ See Ly et al. (2007).

^j First epoch to use the Roach Digital Back End (RDBE), which provides wide bandwidths for all following observations.

^k Used Digital Down Converter personality of the RDBE. Other RDBE observations used the Polyphase Filter Bank personality.

^l Image quality poor. The image was used in the stacked image of Figure 22 but not in the long-term variation analysis or in Figure 18.

^m This image was used in Figure 20 but not in the image montage. The quality is not quite as good as BW115D. The structure is similar.

Table 4
Averages of Multiple Images Used in the Long-term Image Sequence

Observation ^a Code	Average Date	rms ^b ($\mu\text{Jy beam}^{-1}$)	Integrated ^c Flux Density (Jy)	Peak Flux Density (Jy beam^{-1})
BW082	2006.3	137	1.54	0.77
BW088	2007.4	74	1.64	0.63
BW090	2008.1	75	2.13	0.98
BW093	2010.3	127	1.25	0.65

Notes.

^a The stack is a noise-weighted average of all observations in Table 3 using this base observation code. An exception is BW088U, which is included in the 2008 stack, not the 2007 stack. The images used are those with the common resolution of 0.43×0.21 mas, elongated along position angle -16° .

^b The rms is measured with a histogram fit to the full stacked image. This will be subject to the scaling issue noted in note b of Table 3, but the CCRES scale factors will average toward 1.0, so the effect should be small.

^c Flux density is measured by integrating in a box from 1 to -8 mas R.A. offset and -1 to 4 mas decl. offset from the core. At larger distances, low surface brightness and poor short spacing UV coverage make image plane integration unreliable.

Appendix C

Helical Mode Resonant Frequency and Propagation

In this appendix we briefly review the important analytical limiting equations giving the resonant frequency and describing the motion of the helical mode at and below the resonant frequency used to constrain the jet–external medium interface properties that would lead to the observed long-term pattern motion.

An approximate lower limit to the helical mode resonant frequency, ω^* , of

$$\omega^* R_j / v_{we} \approx \frac{3\pi/4}{\left[1 - \left(v_{we}^2/u_j^2 + 2\frac{\gamma_{wj}}{\gamma_{we}} v_{we} v_{wj} / \gamma_j u_j^2 + \frac{\gamma_{wj}^2 v_{wj}^2}{\gamma_{we}^2} / \gamma_j^2 u_j^2\right)\right]^{1/2}} \quad (8)$$

is found in the sonic (fluid) or Alfvénic (magnetic) limits (see Equation (16) in Hardee 2007) in the limit of no flow, $u_e = 0$, in the external (e) medium. In Equation (8) γ_j and u_j refer to the jet (j) Lorentz factor and speed, with $v_{wj} \equiv (a_j \text{ or } v_{Aj})$ and $v_{we} \equiv (a_e \text{ or } v_{Ae})$ in the sonic or Alfvénic limits, respectively. The sound speed a and the Alfvén wave speed v_A are defined by

$$a \equiv \left[\frac{\Gamma P}{W}\right]^{1/2} \quad \text{and} \quad v_A \equiv \left[\frac{V_A^2}{1 + V_A^2/c^2}\right]^{1/2},$$

where the adiabatic index $4/3 \leq \Gamma \leq 5/3$; enthalpy $W \equiv \rho + [\Gamma/(\Gamma - 1)]P/c^2$, where ρ and P are the density and pressure, respectively; and $V_A^2 \equiv B^2/(4\pi W)$, where B is the magnetic field strength, with $\gamma_w \equiv (1 - v_w^2/c^2)^{-1/2}$ the sonic or Alfvénic Lorentz factor accompanying $v_{wj} \equiv (a_j \text{ or } v_{Aj})$ and $v_{we} \equiv (a_e \text{ or } v_{Ae})$. Note that the sonic Lorentz factor $\gamma_{aj,e} = (1 - a_{j,e}^2/c^2)^{-1/2} \leq 1.225$, whereas the Alfvénic Lorentz factor $\gamma_{Aj,e} \equiv (1 + V_{Aj,e}^2/c^2)^{1/2} = (1 - v_{Aj,e}^2/c^2)^{-1/2}$ can be large. The resonant frequency is a function of the velocity shear,

$u_j - u_e$, as well as the sound and Alfvén wave speeds in the jet and external medium, where $\omega^* \rightarrow \infty$ as

$$\frac{u_j - u_e}{1 - u_j u_e / c^2} \rightarrow \frac{v_{wj} + v_{we}}{1 + v_{wj} v_{we} / c^2},$$

where the left-hand side approaches the right-hand side from above.

An estimate for the conditions required for the lower limit to the resonant frequency to exceed this angular frequency can be obtained by assuming that the sound and Alfvén speeds in the jet and external medium are the same, i.e., $a_j = a_e$ or $v_{Aj} = v_{Ae}$ in the sonic or Alfvénic limits. In this case we would find that

$$\omega^* \approx \frac{3\pi}{4} \frac{u_j/R_j}{(u_j/v_w - 1)} \approx \frac{3\pi}{4} \frac{c/R_j}{(c/v_w - 1)} \geq \frac{3\pi}{4} \frac{v_w}{R_j}, \quad (9)$$

where $v_w = (a \text{ or } v_A)$ in the sonic or Alfvénic limits. Below the resonant frequency the helical mode wave speed, v_h , is described by the real part of Equation (8) in Hardee (2007),

$$v_h = \frac{\eta u_j + u_e}{(1 + V_{Ae}^2/\gamma_e^2 c^2) + \eta(1 + V_{Aj}^2/\gamma_j^2 c^2)}, \quad (10)$$

where $\eta \equiv \gamma_j^2 W_j / \gamma_e^2 W_e$. The helical mode wave speed at resonance, v_h^* , can be obtained in the sonic or Alfvénic limits and is given by (Equation (15) in Hardee (2007))

$$v_h^* \equiv \frac{\gamma_j(\gamma_{we} v_{we}) u_j + \gamma_e(\gamma_{wj} v_{wj}) u_e}{\gamma_j(\gamma_{we} v_{we}) + \gamma_e(\gamma_{wj} v_{wj})}. \quad (11)$$

In both these expressions we now allow for an external medium flow $u_e > 0$.

If pattern motion is governed by helical mode propagation below the resonant frequency, a little manipulation allows us to rewrite Equation (10) for W_j/W_e as

$$W_j/W_e = \left[\frac{\gamma_e^2 (v_p - u_e) + v_p (B_e^2 + B_j^2) / 4\pi W_e c^2}{\gamma_j^2 (u_j - v_p)} \right], \quad (12)$$

where we now define $v_p \equiv v_h$.

If pattern motion is more accurately described by helical mode propagation near the resonant frequency, a little manipulation allows us to write Equation (11) as

$$W_j/W_e = \left[\left(\frac{\gamma_e}{\gamma_j} \right) \left(\frac{\gamma_{aj}}{\gamma_{ae}} \right) \frac{(v_p - u_e)}{(u_j - v_p)} \right]^2 \quad \text{or} \\ W_j/W_e = \left[\left(\frac{\gamma_e}{\gamma_j} \right) \left(\frac{B_e}{B_j} \right) \frac{(v_p - u_e)}{(u_j - v_p)} \right]^2, \quad (13)$$

in the sonic or Alfvénic limits, respectively, and where we now define $v_p \equiv v_h^*$. Here we see that the sonic and Alfvénic limiting expressions are comparable to $\gamma_{aj}/\gamma_{ae} \approx 1$ in the sonic case and to $B_e/B_j \approx 1$ in the Alfvénic case when there is magnetic pressure balance between the jet and external medium.

Theory and numerical simulation show that damping of a displacement will occur in the presence of strong magnetic fields (see Mizuno et al. 2007) when

$$(u_j - u_e)^2 - V_{As}^2/\gamma_j^2 \gamma_e^2 < 0, \quad (14)$$

where V_{As} is a “surface” Alfvén speed defined by

$$V_{As}^2 \equiv (\gamma_{Aj}^2 W_j + \gamma_{Ae}^2 W_e) \frac{B_j^2 + B_e^2}{4\pi W_j W_e}.$$

Damping of a bulk displacement will also occur if the wave frequency is less than the resonant frequency. This can occur on an expanding jet, as a wave frequency ω that is initially less than the local resonant frequency ω^* can propagate down the expanding jet to where ω is above the local resonant frequency because $\omega^* \propto R^{-1}$ declines along an expanding jet.

ORCID iDs

R. Craig Walker  <https://orcid.org/0000-0002-6710-6411>
 Frederick B. Davies  <https://orcid.org/0000-0003-0821-3644>
 Chun Ly  <https://orcid.org/0000-0002-4245-2318>

References

- Acciari, V. A., Aliu, E., Arlen, T., et al. 2009, *Sci*, **325**, 444
 Asada, K., & Nakamura, M. 2012, *ApJL*, **745**, L28
 Asada, K., Nakamura, M., Doi, A., Nagai, H., & Inoue, M. 2014, *ApJL*, **781**, L2
 Biretta, J. A., Sparks, W. B., & Macchetto, F. 1999, *ApJ*, **520**, 621
 Birkinshaw, M. 1991, *MNRAS*, **252**, 505
 Blandford, R. D., & Payne, D. G. 1982, *MNRAS*, **199**, 883
 Blandford, R. D., & Zanjek, R. L. 1977, *MNRAS*, **179**, 433
 Briggs, D. 1995, PhD thesis, New Mexico Inst. Mining and Tech., <http://www.aoc.nrao.edu/dissertations/dbriggs/>
 Britzen, S., Fendt, C., Eckert, A., & Karas, V. 2017, *A&A*, **601**, A52
 Cheung, C. C., Harris, D. E., & Stawartz, L. 2007, *ApJ*, **662**, 213
 Deller, A., Britzen, W. F., Phillips, C. J., et al. 2011, *PASP*, **123**, 275
 Gebhardt, K. 2011, *ApJ*, **729**, 119
 Giroletti, M., Hada, K., Giovannini, G., et al. 2012, *A&A*, **538**, L10
 Greisen, E. W. 1995, in *Information Handling in Astronomy—Historical Vistas*, ed. A. Heck (Dordrecht: Springer), 109
 Greisen, E. W., Spekkens, K., & van Moorsel, G. A. 2009, *AJ*, **137**, 4718
 Hada, K., Doi, A., Kino, M., et al. 2011, *Natur*, **477**, 185
 Hada, K., Giroletti, M., Kino, M., et al. 2014, *ApJ*, **788**, 165
 Hada, K., Kino, M., Doi, A., et al. 2013, *ApJ*, **775**, 70
 Hada, K., Kino, M., Doi, A., et al. 2016, *ApJ*, **817**, 131
 Hada, K., Kino, M., Nagai, H., et al. 2012, *ApJ*, **760**, 52
 Hada, K., Park, J., Kino, M., et al. 2017, *PASJ*, **69**, 71
 Hardee, P. E. 2007, *ApJ*, **664**, 26
 Hardee, P. E., & Eilek, J. A. 2011, *ApJ*, **735**, 61
 Hardee, P. E., Hughes, P. A., Rosen, A., & Gomez, E. 2001, *ApJ*, **555**, 744
 Jorstad, S., & Marscher, A. 2016, *Galax*, **4**, 47
 Junor, W., & Biretta, J. A. 1995, *AJ*, **109**, 500
 Junor, W., Biretta, J. A., & Livio, M. 1999, *Natur*, **401**, 891
 Kovalev, Y. Y., Lister, M. L., Homan, D. C., & Kellermann, K. I. 2007, *ApJL*, **668**, L27
 Kuo, C. Y., Asada, K., Rao, R., et al. 2014, *ApJL*, **783**, L33
 Laing, R. A. 1981, *ApJ*, **248**, 87
 Lister, M. L., & Homan, D. C. 2005, *AJ*, **130**, 1389
 Lobanov, A., Hardee, P., & Eilek, J. 2003, *NewAR*, **47**, 629
 Ly, C., Walker, R. C., & Junor, W. 2007, *ApJ*, **660**, 200
 Ly, C., Walker, R. C., & Wrobel, J. M. 2004, *AJ*, **127**, 119
 Madrid, J. P., Sparks, W. B., Harris, D. E., et al. 2007, *Ap&SS*, **311**, 329
 Marscher, A. P., Jorstad, S. G., D’Archangelo, F., et al. 2008, *Natur*, **452**, 966
 Marshall, H. L., Miller, B. P., Davis, D. S., et al. 2002, *ApJ*, **564**, 683
 McKinney, J. C. 2006, *MNRAS*, **368**, 1561
 McKinney, J. C., & Blandford, R. D. 2009, *MNRAS*, **394**, L126
 Mei, S., Blakeslee, H. P., Côté, P., et al. 2007, *ApJ*, **655**, 144
 Mertens, F., & Lobanov, A. 2015, *A&A*, **574**, A67
 Mertens, F., Lobanov, A. P., Walker, R. C., & Hardee, P. E. 2016, *A&A*, **595**, A54 (MLWH)
 Mizuno, Y., Hardee, P. E., & Nishikawa, K.-I. 2007, *ApJ*, **662**, 835
 Nakamura, M., & Meier, D. L. 2014, *ApJ*, **785**, 152
 Napier, P. J., Bagri, D. S., Clark, B. G., et al. 1993, *IEEEP*, **82**, 658
 Owen, F. N., Hardee, P. E., & Cornwell, T. 1989, *ApJ*, **340**, 698
 Perlman, E. S., Biretta, J. A., Sparks, W. B., Macchetto, F. D., & Leahy, J. P. 2001, *ApJ*, **551**, 206
 Perlman, E. S., Biretta, J. A., Zhou, F., Sparks, W. B., & Macchetto, F. D. 1999, *ApJ*, **117**, 2185
 Perlman, E. S., & Wilson, A. S. 2005, *ApJ*, **627**, 140
 Reid, M. J., Biretta, J. A., Junor, W., Muxlow, T. W. B., & Spencer, R. E. 1989, *ApJ*, **336**, 112
 Rudnick, L., & Edgar, B. K. 1984, *ApJ*, **279**, 74
 Sparks, W. B., Biretta, J. A., & Macchetto, F. 1996, *ApJ*, **473**, 254
 Tchekhovskoy, A., Narayan, R., & McKinney, J. C. 2011, *MNRAS*, **418**, L79
 Van Moorsel, G. 2014, VLBA Observational Status Summary 2015A (Socorro, NM: NRAO), <https://science.lbo.us/facilities/vlba/docs/manuals/oss2015A>
 Walker, R. C., Hardee, P. E., Davies, F., et al. 2016, *Galax*, **4**, 46
 Walker, R. C., Ly, C., Junor, W., & Hardee, P. E. 2008, *J. Phys. Conf. Ser.*, **131**, 012053
 Walsh, J. L., Barth, A. J., Ho, L. C., & Sarzi, M. 2013, *ApJ*, **770**, 86
 Wang, C.-C., & Zhou, H.-Y. 2009, *MNRAS*, **395**, 301
 Wilson, A. S., & Yang, Y. 2002, *ApJ*, **568**, 133
 Zavala, R. T., & Taylor, G. B. 2002, *ApJ*, **566**, 9